

# Investigation of Hydrogen Sorption in Magnesium-based Sputtered Thin Films

By

Cao Yuan

Final thesis submitted to the University of Birmingham

For the Degree of

**Master of Philosophy**

School of Metallurgy and Materials

College of Engineering and Physical Sciences

University of Birmingham

August 2018

UNIVERSITY OF  
BIRMINGHAM

**University of Birmingham Research Archive**

**e-theses repository**

This unpublished thesis/dissertation is copyright of the author and/or third parties. The intellectual property rights of the author or third parties in respect of this work are as defined by The Copyright Designs and Patents Act 1988 or as modified by any successor legislation.

Any use made of information contained in this thesis/dissertation must be in accordance with that legislation and must be properly acknowledged. Further distribution or reproduction in any format is prohibited without the permission of the copyright holder.

**Keywords:** Magnetron sputtering, Mg based thin film, hydrogen sorption properties, hydrogenation and dehydrogenation, hydrogen storage and hydrogen sensor, interface shear stress, buckling, Mg/Y multilayer, Van't Hoff plot

## Synopsis

Hydrogen sorption into Mg-based thin films prepared by magnetron sputtering was investigated. The hydrogen storage properties and thin films' physical properties were investigated in the experiments.

Mg thin films were prepared in a Closed Field Unbalanced Magnetron Sputter Ion Plating (CFUBMSIP) system. This system has advantage for homogenous and uniform coatings which is better than conventional coating system. The sputtering parameters are shown to have a significant influence on the microstructure and intrinsic film growth stress in Mg thin films. The intrinsic stress can be examined by X-Ray Diffraction (XRD) during hydrogen absorption, in plane tensile stress of Mg thin films grows due to crystallite coalescence.

The surface roughness and buckling appearance were characterized by Confocal microscopy and Profilometry. Surface roughness has the relationship with the Mg thickness. During hydrogen absorption, high stress accumulates leading to more buckling. While, more buckling indicates high thin film surface roughness.

The effect of Mg layer thickness (lower than 1000 nm) was investigated. Mg thickness can influence the hydrogen sorption behavior. Thinner Mg layers can have a lower hydrogen absorption temperature comparing with thicker films. Film thickness has the effect on Mg grain boundary diffusion which is dominated by trans-granular diffusion. Different film thickness has different Mg grain boundary diffusion rate.

As Pd alloys with Mg at high temperatures, a Ti interlayer can be used to prevent inter-diffusion between Pd and Mg. SEM microscopy was tried to find the grain boundary between

Mg and Pd. Si substrate was tried considering weight and volume of glass substrate. Thermodynamics was influenced during hydrogen sorption process with Si substrate.

Mg based thin films were sputtered onto glass substrates. The overall hydrogen storage uptake was reduced due to the volume of glass. Thus, a silicon substrate was used, which has a lower volume and weight comparing to the glass substrate. Hydrogen storage capacity will be modified. In addition, different substrates can influence the adhesion energy between the Mg layer and the substrate. The films growth mode and microstructure are factors which can ultimately influence the thermodynamics of the Mg thin films. Buckling is shown during hydrogen sorption process, which can accumulate stresses. The interface shear stress of Mg thin films can be measured. High stress accumulates with more buckling at the surface. The hydrogenation conditions are relevant with the interface shear stress. Mg thickness, hydrogenation times and hydrogenation temperature are the main hydrogenation conditions. For example, the interface shear stress is around 1.75 GPa of sample Pd (60 nm)-Mg (150 nm) glass substrate after hydrogenation 72h at room temperature. While at the same conditions, sample Pd (60 nm)-Mg (800 nm) glass substrate has the interface shear stress lower than 1 GPa. The interface shear stress is influenced by hydrogenation conditions which may be useful for mechanical hydrogen sensors.

The electrical resistance of Mg based thin film can be measured using two probes and four probes technique. The four probe technique gave more accurate results. 2A 25sccm condition has the lowest electrical resistance among the measuring samples which is around  $2\Omega$ .

Finally, a Mg/Y based multilayer system was investigated. Mg/Y based multilayer appears to provide a new method towards  $MgH_2$  destabilization by accommodating of lattice mismatch between strained FCC Mg/Y interfaces. There is no alloying phase formation between Y and Mg under high temperature He atmosphere.

## **Acknowledgements**

I would like to say thank you to Professor David Book and Dr Shahrouz Nabossadri for their help and kindness during my MPhil study period. Besides I would also say thank you to the support by the whole hydrogen storage group in the University of Birmingham.

I will also say thanks to my parents during my MPhil study. They help me a lot when I come across the illness. Their suggestions and support are really useful for me. Although I can only see them one or two times per year, I still miss them a lot.

If there are no ups and downs, I will say you are too lucky. I meet so many difficulties to fix the equipment and learn to use new equipment. Of course, I need to say thank you to Shahrouz Nayebossadri and Simon Cannon for their help in these aspects. They have very good skills in equipment fixing and technique training. I learn a lot from them.

During the MPhil study, I learn much not only how to analysis the data but also how to make a useful plan. Before doing experimental work, I will make a short plan and discuss with the supervisors. The professor will provide some guidelines and suggestions. This step makes me improve a lot of knowledge in my study.

As a research student in the University of Birmingham, I want to say that this is a special period in my life. Sometimes I need to work hard and sometimes I feel relax at that moment. A lot of things you cannot control. You can only manage yourselves. The experience is unique and special which is never copied. In the end, I want to say that no matter how time flies, I will cherish more than two years of MPhil periods. I spend almost two years finishing my research work and hope to obtain the MPhil degree. No matter what to say, it is a memorable period to my life.

## Contents

<b>1. Global Energy of Hydrogen</b> .....	1
1.1 Brief introduction.....	1
1.2 Trends in hydrogen energy applications .....	1
1.3 Global warming and climate change.....	3
1.4 Legislation .....	6
1.5 Hydrogen properties and hydrogen energy applications.....	7
1.6 Summary .....	13
<b>2. Literature Review</b> .....	15
2.1 Hydrogen storage technologies.....	15
2.1.1 Liquid hydrogen storage .....	17
2.1.2 Compressed hydrogen storage.....	18
2.1.3 Solid-state hydrogen storage.....	18
2.2 Hydrogen sorption properties of magnesium .....	26
2.3 Mg thin film.....	32
2.3.1 Overview of Mg thin film for hydrogen storage .....	33
2.3.2 Control of microstructure during sputtering .....	35
2.3.3 Stress effect (compressive stress and tensile stress).....	39
2.3.4 Thermal stress.....	41
2.3.5 Surface roughness and buckling of thin film .....	42
2.3.6 Hydrogen sorption behavior (hysteresis) .....	42
2.3.7 Interlayer and various substrate.....	46
2.3.8 Optical transmittance of thin film.....	59
2.3.9 Sheet resistivity of Mg-based thin film.....	62
2.3.10 Multilayer .....	65
2.3.11 Conclusions of thin films .....	71
2.4 Thin film deposition systems.....	72
2.4.1 Nucleation of free energy consideration .....	73
2.4.2 Determining $\theta$ .....	74
2.4.3 Temperature effect.....	75
2.5 Hydrogen storage applications and hydrogen sensors .....	76
<b>3. Aims and Objectives</b> .....	80
<b>4. Experimental Techniques</b> .....	82
4.1 Sputtering machine (CFUBMSIP).....	82
4.2 Confocal microscopy and SEM.....	84

4.3 XRD (X-ray diffraction).....	87
4.4 Hydrogenation chamber .....	89
4.5 Profilometer .....	89
4.6 Four probe and two probe resistivity measurement .....	90
4.7 Optical UV-laser .....	90
4.8 TPD measurement (RGA) .....	91
4.9 Raman spectroscopy .....	93
<b>5. Results .....</b>	<b>95</b>
5.1 Effect of sputtering conditions.....	95
5.1.1 Summary .....	100
5.2 XRD results (under He or H <sub>2</sub> ) .....	100
5.2.1 Room temperature XRD .....	100
5.2.2 In-situ XRD of thin-films under He atmosphere.....	104
5.2.3 In-situ XRD of thin-films under H <sub>2</sub> atmosphere .....	104
5.2.4 Conclusions .....	109
5.3 Hydrogen sorption properties of Mg thin film .....	109
5.3.1 Conclusions .....	117
5.4 Thickness effect of Mg thin film .....	118
5.5 Interface shear stress linked with hydrogenation process .....	119
5.5.1 Conclusions .....	124
5.6 Surface roughness and buckling appearance of Mg thin film .....	125
5.6.1 Conclusions .....	130
5.7 Mg based multilayers .....	131
5.8 Sheet resistivity of Mg based thin films .....	135
5.8.1 Two probe technique .....	135
5.8.2 Four probe technique .....	136
5.9 Optical behaviors .....	136
5.9.1 Conclusions .....	137
<b>6. Conclusions .....</b>	<b>138</b>
6.1 General discussion .....	138
6.2 Final conclusions .....	140
6.3 Future work .....	141
<b>List of Publications .....</b>	<b>144</b>
<b>References .....</b>	<b>145</b>

# **1. Global Energy of Hydrogen**

## **1.1 Brief introduction**

Energy utilizing is important and used all over the world. As a requirement for everyday life conventional energy sources such as fossil fuels have caused carbon dioxide emission and particulate pollution, the environmental impact has been considerable. Carbon dioxide is produced during the burning of fossil fuels leading to global warming. One of the main issues of 21<sup>st</sup> century is to choose sustainable energy in order to reduce air pollution. Fossil fuels could be partially replaced by hydrogen energy. [1] Compared with fossil fuel systems, hydrogen energy systems have the potential to be more sustainable and environmental friendly. However, for the introduction of a hydrogen-based economy, there are still problems to be overcome and the requirements for the transportation sector also need to be carefully considered. In the future, there could be a global market for hydrogen-based applications such as hydrogen sensors and mobile hydrogen storage applications. [1]

## **1.2 Trends in hydrogen energy applications**

Hydrogen economy, hydrogen production, hydrogen storage, hydrogen sensors and hydrogen fuel cells are all important aspects. Countries such as USA, Japan, Germany and South Korea have already been developing hydrogen fuels for commercial use. For example, the Toyota Mirai fuel cell car from Japan has started to be sold to various European countries. Hydrogen fuel cell technologies have begun new step to commercialization. For example, hydrogen supply stations have recently been built in Shanghai (China) and in Amelsburen Germany. [1] While a number of countries including USA, Germany, Japan, UK and Poland have begun demonstrating hydrogen fuel cell cars. The cost of fuel cell systems has significantly decreased over the last two decades, due to developments in advanced materials selection,

catalyst loading reduction, system optimization, and manufacturing scale-up improvements.

[1]

Out of all the different regional developments, Japan has been developing the utilization of hydrogen energy applications, particularly rapidly. This has included PEM and solid oxide fuel cell systems for residential power in Japan, and PEM fuel cell cars which are being introduced all over the world by Toyota and Honda. There are policies being planned to develop fuel cells and hydrogen storage systems by 2015. [1] For example, power generation PEFC units are shown in Fig 1.1, and a plan for how they would integrate with a community is shown in Fig 1.2. PEFC systems use hydrogen as a fuel to provide electricity. While the hydrogen is first supplied by electrolyzing water using electricity generated by solar panels and then storing the hydrogen in a compressed form. Therefore, this is a schema to provide low carbon power for transport and to ensure that smart houses do not need to burning fossil fuels. [1]

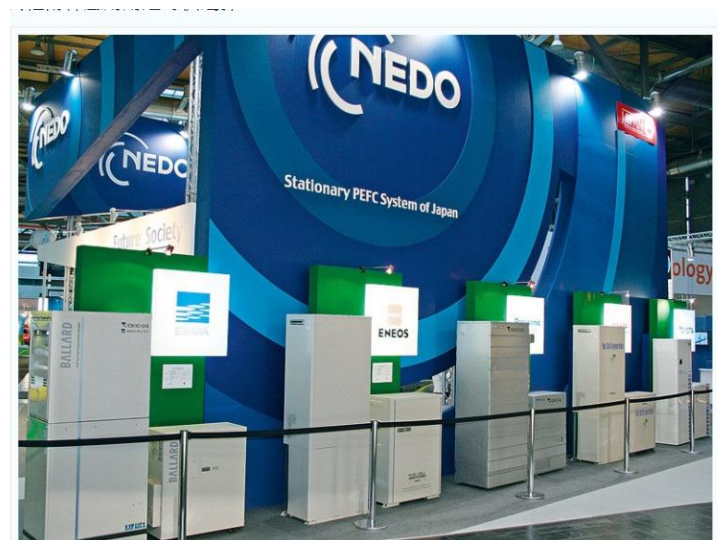


Fig 1.1 Practical image of stationary PEFC system in Japan [1]

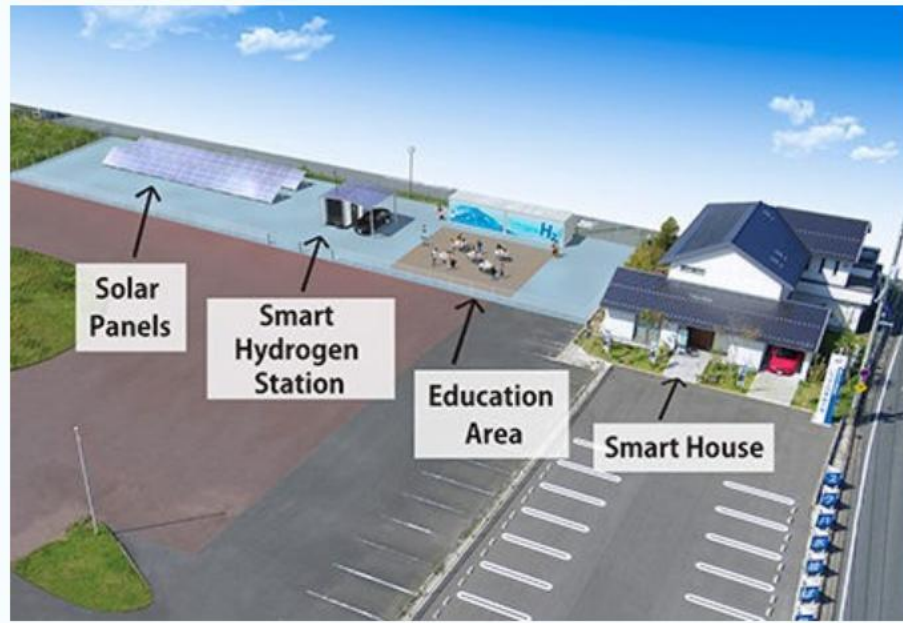


Fig 1.2 Hydrogen energy community centre comprising: solar panels, smart hydrogen station, education area and smart house. [1]

### 1.3 Global warming and climate change

The industrial revolution had a profound effect on human development, the environment and on natural resources. Starting in the mid-1700s in Great Britain, this revolution involved the development of machines that can replace manual labor, which was fueled by fossil fuels instead of wind and water. Instead of wind and water, the impact of this change began to be realized in the UK in the 18<sup>th</sup> century: the combustion of coal caused a dramatic increase in air pollution. [2, 3] Complete or non-complete combustion of hydrocarbons produces H<sub>2</sub>O, CO, CO<sub>2</sub> and various particulate particles. The production of CO<sub>2</sub> leads to global warming causing a change in climate; in particular, an increase in temperature linked to man-made CO<sub>2</sub> emissions. The CO<sub>2</sub> concentration was about 260 ppm (parts per million) in 1790, 376 ppm in 2003 and is projected (by some models) to reach 700 ppm by 2050. [1] In the 20<sup>th</sup> century, the temperature of the earth increased by about 0.7 °C and thus climate change has become a

very significant environmental, economic, social and political issue which every country needs to face. However, it remains to be seen whether CO<sub>2</sub> reduction targets can be met, by increased energy efficiency and the introduction of clean energy. Hydrogen energy is an important approach to replace fossil fuels as a fuel and an energy vector, as it: is the most abundant element in the universe, and has the highest energy per unit mass. [1] The utilization of hydrogen has the potential to be safe, flexible, reliable and sustainable form of energy vector. [2, 4] Today, renewable energy accounts for 3% of global energy production without large-scale hydroelectricity, as shown in Fig 1.3. Oil consumption is the largest among these energy consumption sources, at around 400 million tonnes shown in Fig 1.3. Nuclear energy and hydroelectricity have remained constant in recent years until 2012. The reports from organizations including IEA (international Energy Agency) and BP (British Petroleum) predict increases in energy demand above 56 % (from 2010 to 2040). [5, 6, 7] A number of countries, particularly in the Middle East, depend economically on oil export, and so they are likely to have increasing energy security risks. The renewable energy has a big impact on the energy construction of these countries. Oil price shocks may have resulted in US stagflation in the 1970s. [7]

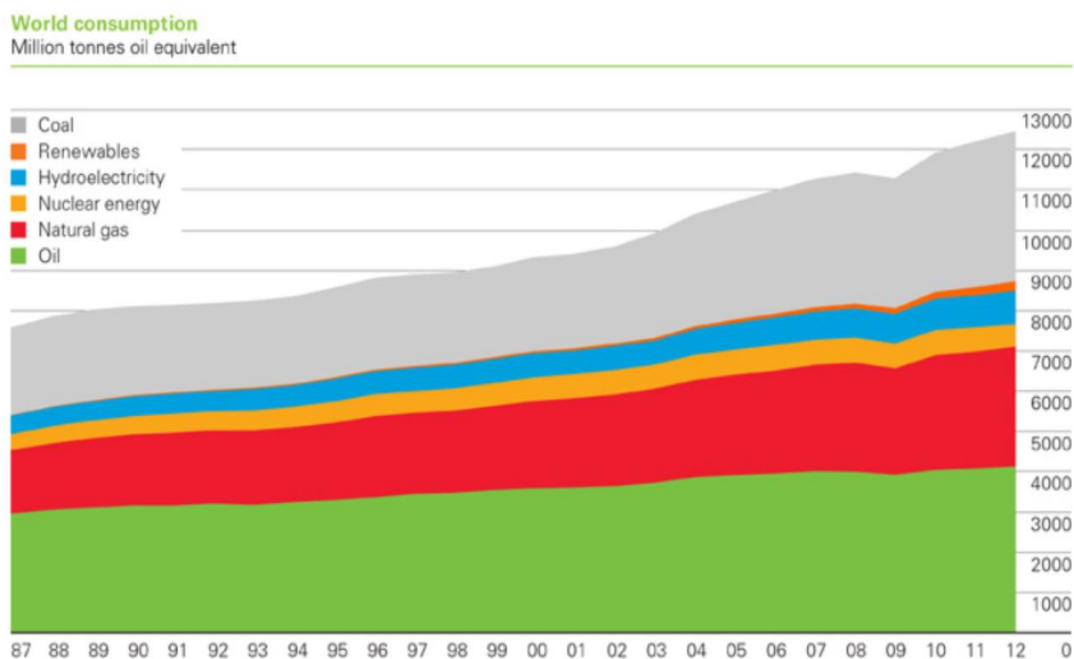


Fig 1.3 World energy consumption up to 2012 The Y axis describes the quantity of energy in equivalent units of millions of tonnes of oil and the X axis is the year. (1 tonne is equivalent to around 42 GJ). Around 80% of all energy was supplied by fossil fuels with the remainder being made up of nuclear and hydroelectric/ renewable. [7]

As shown in Fig 1.4, the monthly CO<sub>2</sub> concentration has increased rapidly since 1960. The amount of CO<sub>2</sub> concentration reached about 400 parts per million in 2015. [8] CO<sub>2</sub> is a green house gas, which has the ability to absorb and reflect infrared radiation, and so increased CO<sub>2</sub> will cause temperature build up. [8]

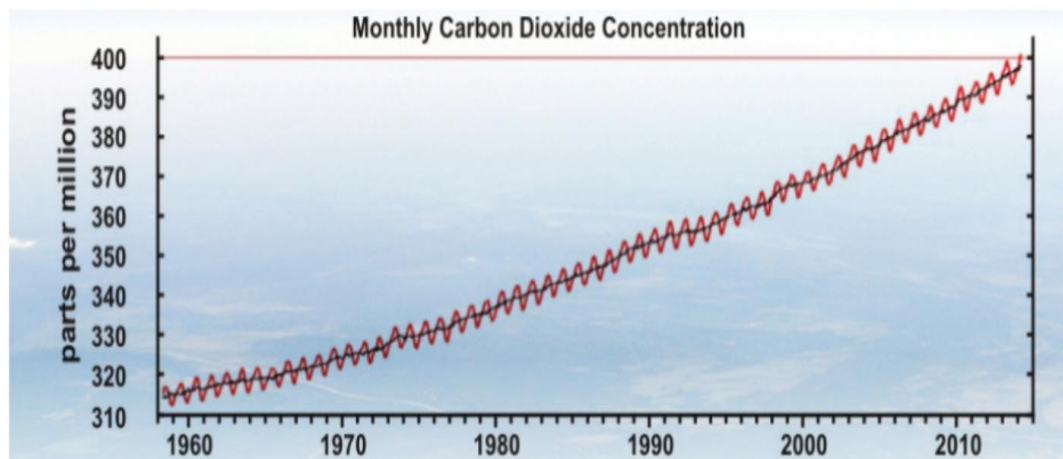


Fig 1.4 Concentration of atmospheric carbon dioxide from around 1960 [8]

To try to deal with this problem of atmospheric CO<sub>2</sub> build-up, there have been various proposals. As an example, in 1998, the European Commission made an agreement that CO<sub>2</sub> emissions should be cut to 140 g CO<sub>2</sub>/km by 2008/9. The CO<sub>2</sub> emissions were reduced more than 25% from 1998 to 2008. The UK averaged about 130 g CO<sub>2</sub>/km in 2015. In the future, it is estimated that it will reduce to 120 g CO<sub>2</sub>/km before 2020 though strong controlling by the government. For the future target, it will be set at 95 g CO<sub>2</sub>/km since 2021. Besides, the CO<sub>2</sub> targets for the vans are made in 2011. The target of 147 g CO<sub>2</sub>/km has been set as the goal for the 2020 as for the light duty vans. [9]

Fig 1.5 shows a slight decline in US energy production; coal production has decreased in recent years, while renewable energy and natural gas energy have increased since 2010. Both natural gas and renewable energy can reduce the CO<sub>2</sub> emissions compared to burning coal. U.S primary energy production totaled 70 quadrillion British thermal units (Btu) in 2000 and 84 quadrillion British thermal units (Btu) in 2016. This trend has continued in recent years. [10]

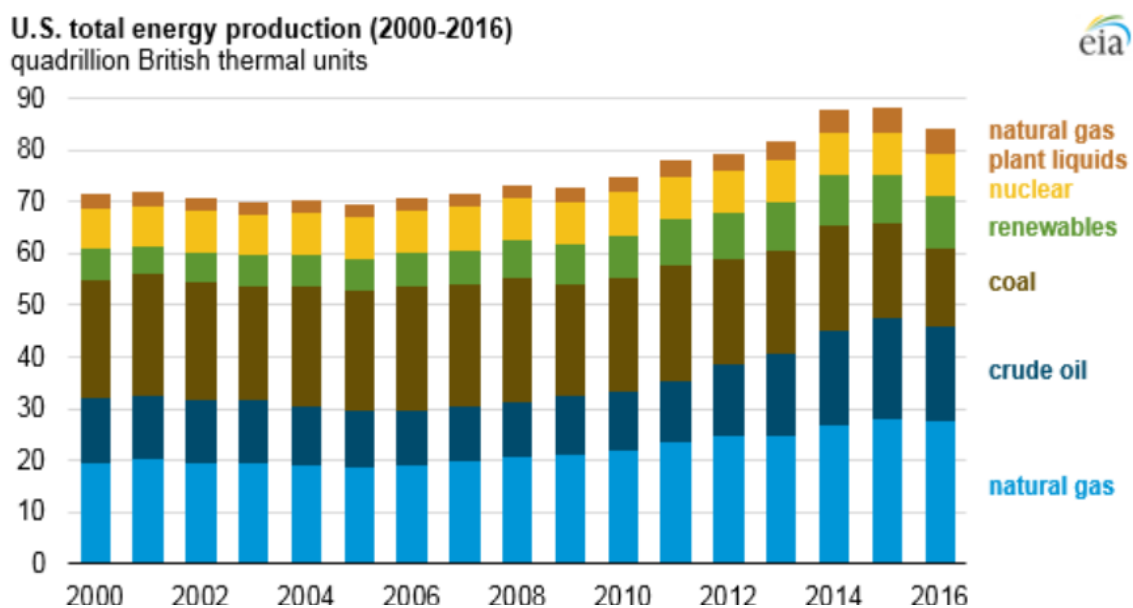


Fig 1.5 Total U.S. energy production fell in 2016 after six consecutive years of increases from 2009 to 2015. Total energy production includes natural gas, nuclear energy, coals, oil and natural gas. [10]

#### 1.4 Legislation

Politicians and governments have been aware of the problems with the energy system, in recent years. There has been increasing pressure for governments to provide more funding into research to reduce carbon dioxide emissions. Many governments agreed and approved recommendations made by the IPCC in 1997, leading to the Kyoto protocol entering into force in 2005. The main feature of this protocol is targets to reduce greenhouse gas emissions

for the world's leading economies. [11, 12] In the UK, the Climate Change Act (2008) has also provided a goal for long-term UK greenhouse gas reductions, i.e. reduce greenhouse gas emissions by 34% before 2020 and 80% before 2050. [13] In addition, the UK government has proposed the transportation should meet the Climate Change Act (2008) obligations. The Vehicle Certification Agency (VCA) has summarized the different EC low-carbon transport legislation to which the UK is committed, including EC/443/2009 and EC/510/2011. Other countries also have targets for reductions, e.g. Germany aims to reduce CO<sub>2</sub> emissions by 95% by 2050. [13]

### 1.5 Hydrogen properties and hydrogen energy applications

Hydrogen gas is the lightest gas, with a density of about 0.0899 g L<sup>-1</sup> (under standard temperature and pressure). [1] With a mass about 1/14 that of air, hydrogen is a constituent part of water (H<sub>2</sub>O), which means that there is the prospect of hydrogen being widely available if economic water decomposition (e.g. electrolysis, thermo-catalysis, biological, etc) can be achieved. After hydrogen production the next important step to consider is hydrogen storage. This is of particular importance to hydrogen fuel cell cars. As shown in Fig 1.6, automotive PEM fuel cell technology cost has significantly reduced, and is predicted to continue to decrease. In 2014 and 2015, the first commercial releases of hydrogen fuel cell cars took place by Hyundai (in South Korea) and Toyota (in Japan). It has been predicted that by 2025, such fuel cell cars will be widespread, and their cost will have reduced by about 95%. [1]

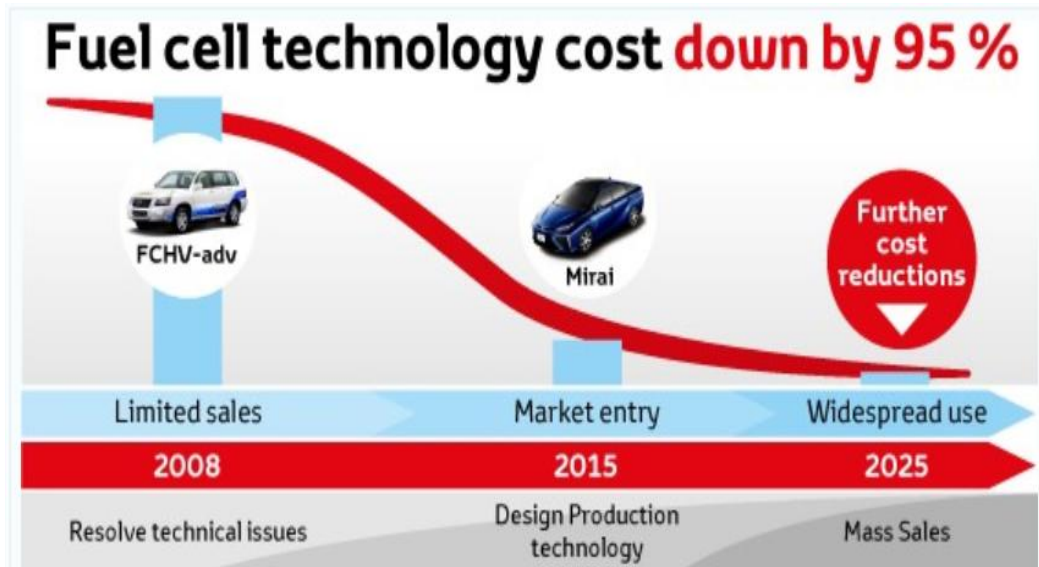


Fig 1.6 development of automotive PEM fuel cell technology; cost has reduced by 95% from 2008 to 2025 [1]

Hydrogen storage can be a challenge issue for hydrogen fuel cell vehicles because hydrogen storage ability influences the endurance of fuel cells. A suitable material for hydrogen storage is a requirement for effective mobile hydrogen energy applications. So far, some hydrogen storage alloys have 2 to 3 wt% hydrogen storage capacities, but this is not high enough to meet the US DOE target which is around 5 wt%. However, Mg based hydrides are promising candidates for on board hydrogen storage due to their high intrinsic capacity of 7.6 wt%. The hydrogen sorption kinetics can be improved by adding a catalyst to the Mg-hydride powder; and ball milling to decrease the grain size. The drawback of ball-milled catalyzed Mg hydride is easy to be oxidized. The future work is to achieve the goal by improving the development on hydrogenation of metal hydrides. [1, 4]

Fig 1.7 shows how coal was replaced by liquid oil due to the development of the automotive internal combustion engine. The next evolution may well be hydrogen-powered automotive fuel cell because of the demand for low-carbon emission vehicles. Fuel cells are suitable due to their high efficiency. [14]

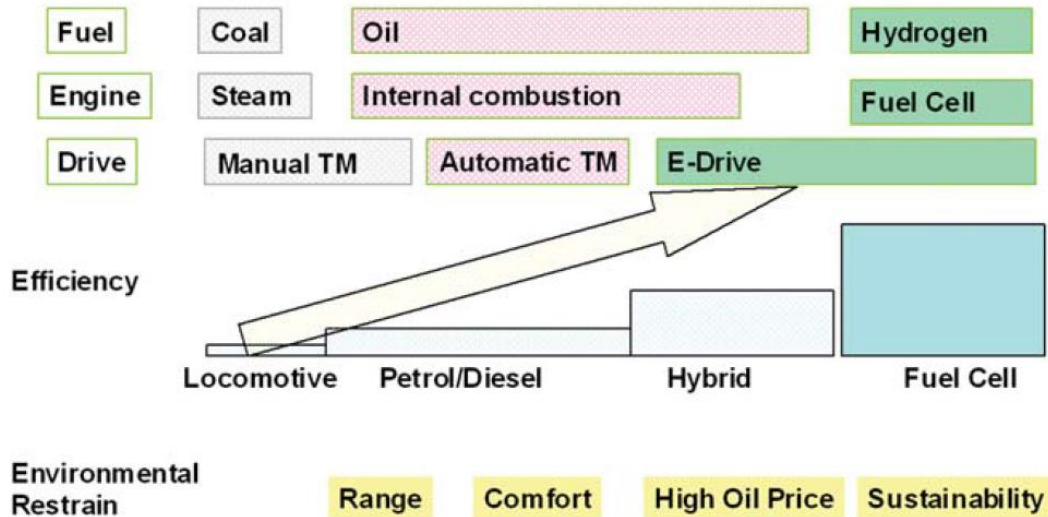


Fig 1.7 Hydrogen materials innovation and society including Locomotive, Petrol / Diesel, hybrid and fuel cell technologies [14]

Various types of energy storage systems are shown in Fig 1.8. Both the volumetric and gravimetric energy densities are highest for fossil fuels (apart from nuclear). Hydrogen has a very high gravimetric energy density and very low volumetric density. The gravimetric energy density of hydrogen is about 10 - 100 kWh kg<sup>-1</sup>. For other applications such as Li ion battery and Pb-acid battery, they have similar volumetric density and gravimetric energy density. The introduction of energy application such as battery should make technological and economic sense. These energy applications are widely used in the market all over the world.

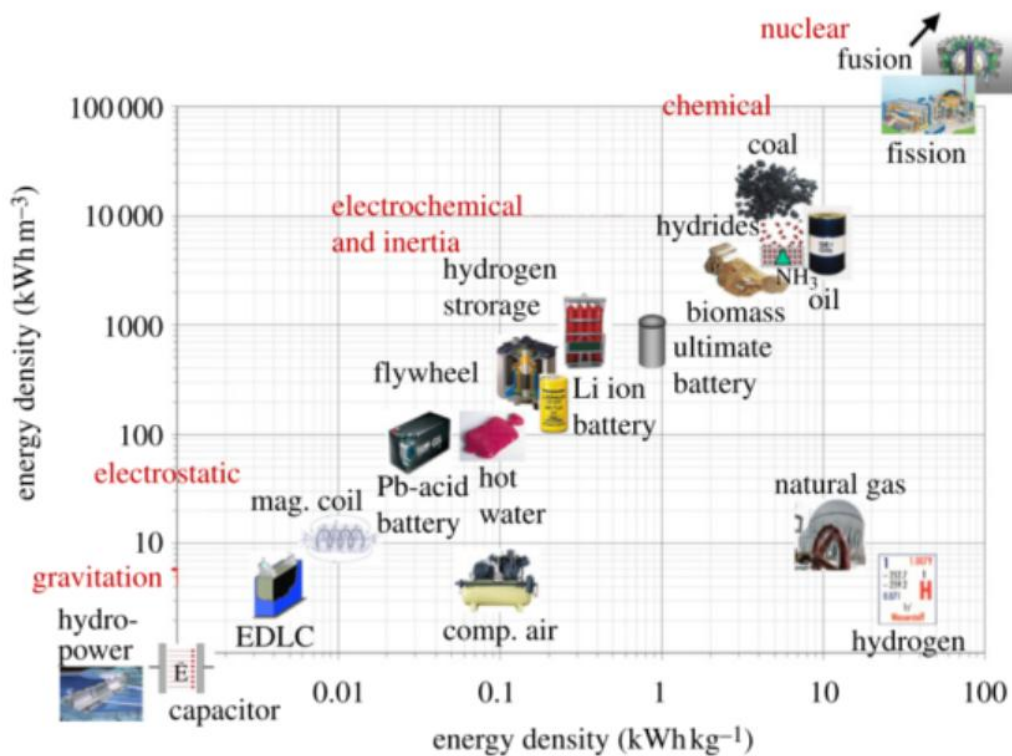


Fig 1.8 shows the volumetric (y-axis) and gravimetric (x-axis) energy storage densities of different technologies. Hydrogen has a very high gravimetric energy density and very low volumetric density while hydrides have high gravimetric energy density and high volumetric density. [12]

The potential hydrogen cycle is shown in Fig 1.9. The sun provides solar energy for water electrolysis. Electrolysis forms  $H_2$  and  $O_2$  by reaction:  $2H_2O = 2H_2 + O_2$ . Hydrogen can then be reversibly stored, e.g. as a metal (as shown by the equation  $M + 1/2H_2 = MH$ ). The subsequently released hydrogen can react with oxygen to form water at last for electrolysis energy cycle supply. The efficiency is above 50% in each step.

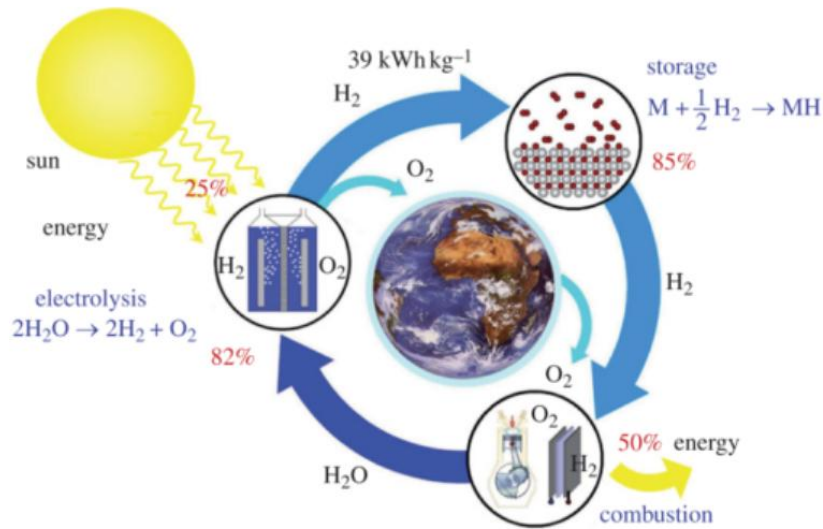


Fig 1.9 it is the picture of hydrogen circle. Solar energy is used to electrolyze water. Hydrogen is then stored and then combusted when required. This cycle is closed and the only energy input comes from the sun. [12]

A plan for a multi-level hydrogen energy centre is shown in Fig 1.10. This includes an autonomous hydrogen centre (AHC), coastal hydrogen centre (CHC), off-shore hydrogen centre (OHC) and Inland hydrogen centre (IHC). Hydrogen can be produced in many ways such as dissociation from CH<sub>4</sub> in common knowledge. [1] The hydrogen is then used for a range of applications (eg. buildings and transportation) which link to our everyday lives.

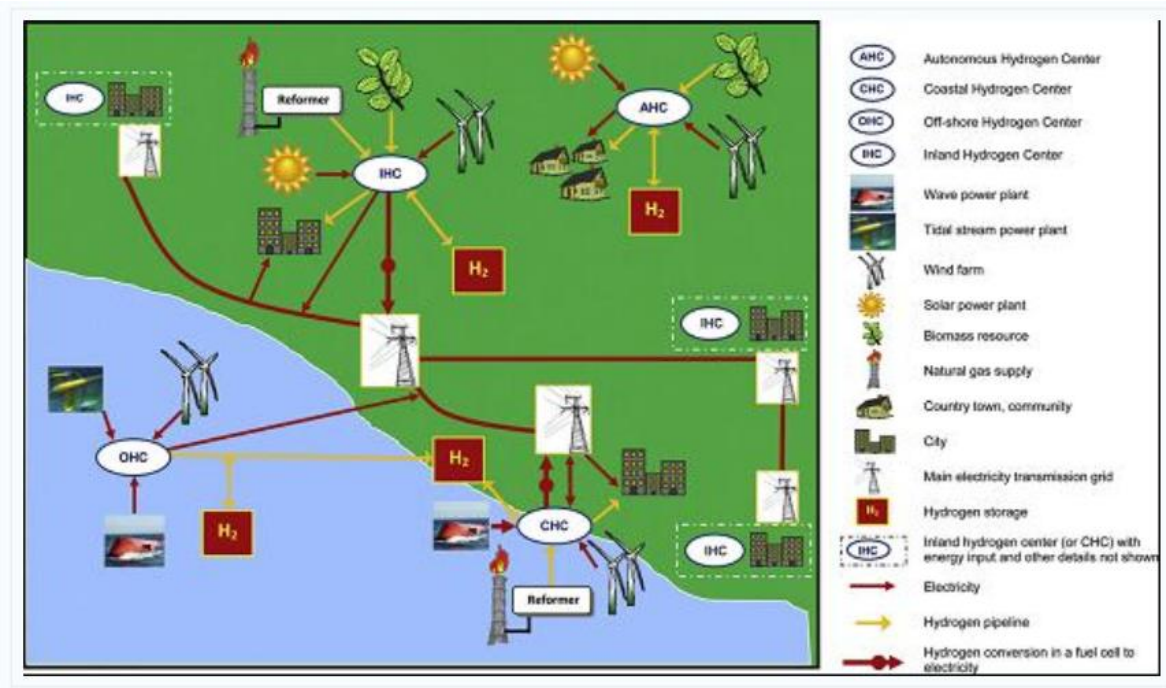


Fig 1.10 Schematic of multi-level hydrogen energy application center [1]

As shown in Fig 1.11, hydrogen can be produced from coal, natural gas, biomass and municipal waste. Hydrogen can also be made by splitting water via electrolysis, using electrolysis from wind energy. The hydrogen can then be stored as a compressed gas, as a liquid or within certain solid materials (hydrides). Hydrogen can then be supplied to fuel cell in order to produce electricity for applications such as transportation and stationary heat generation.

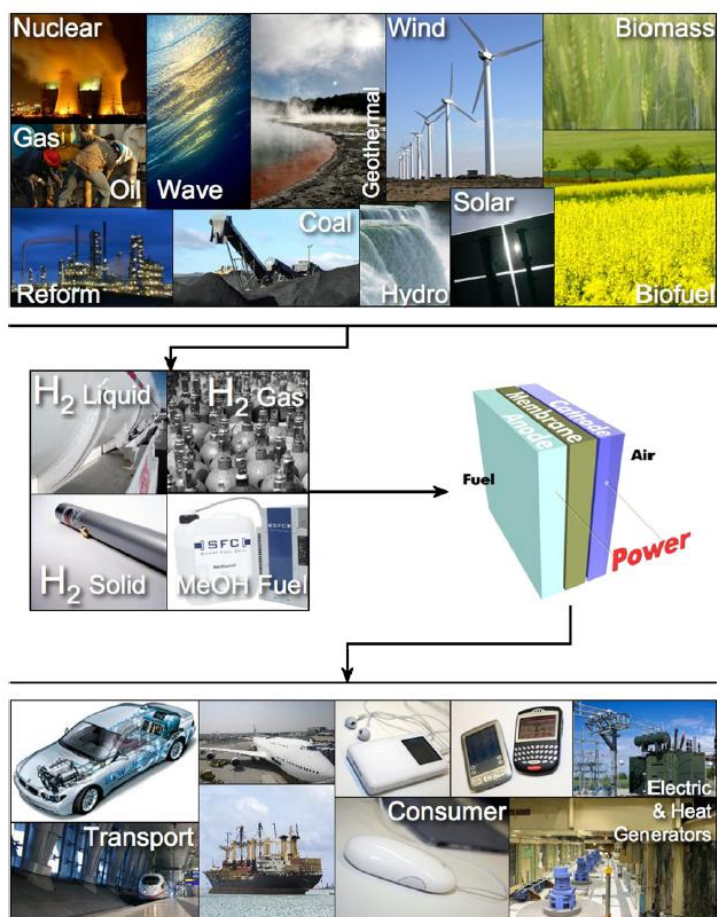


Fig 1.11 Hydrogen as an energy carrier linking multiple production methods and sources to various fuel cell applications [15]

## 1.6 Summary

Hydrogen energy applications could be a promising way of reducing CO<sub>2</sub> emissions. There are various materials which can store hydrogen, some of which can meet some of the hydrogen storage targets and so which are worth investigating. Compressed hydrogen and liquid hydrogen are already used for various applications. Many countries including developed and developing countries, are focused on hydrogen applications and fuel cell use. For example the IPHE (International Partnership on Hydrogen Energy) was established in 2003 with the aim of accelerating the use of clean energy and mobility systems using fuel cells and hydrogen (FCH) technologies. The aim of the IPHE has been to accelerate the

commercialization of FCH technologies. [1] There are some changes for hydrogen and fuel cell applications which will influence the world.

- Increased legislation is attempting to reduce CO<sub>2</sub> emissions and improve local air quality. The hydrogen based economy provides solutions to potential problems with renewable energy.
- Energy demand is good for economic growth analyzing. Energy demand can help the government to set the energy use targets.
- Although oil and fossil fuels productions still have remaining, they will reach a ceiling in the future. Increases in oil prices have been held responsible for reduced productivity and lower economic growth.
- Renewable energy such as solar energy and wind energy is predicted to become the useful energy in the energy industry due to their sustainable properties.
- Hydrogen energy power stations will be used to provide power for both buildings and vehicles.
- Hydrogen fuel cell technology can be the promising applications for hydrogen use because it requires hydrogen gas supply. Hydrogen fuel cells can supply electricity to different applications with only water as a byproduct, therefore depending on the source of the hydrogen, the fuel cell systems may be considered sustainable and environmental friendly. The future demand for portable electric power supplier can exceed the capability of battery technology. [1]
- The hydrogen economy can be a possible solution to solve the potential problems such as CO<sub>2</sub> pollution and other energy waste. However, it still has more challenges to be overcome such as optimizing the energy construction in the future.

## 2. Literature Review

The literature review is split into five sections. Firstly, the broad introduction of three known methods for hydrogen storage including liquid hydrogen, compressed hydrogen and solid state hydrogen will be discussed. Secondly, both the advantages and disadvantages of hydrogen storage methods are referred in this section. Thirdly, in solid state hydrogen storage, both powder and Mg based thin film are discussed. Mg based thin films can also store hydrogen; this will be compared with MgH<sub>2</sub> powder. The various properties of Mg thin films will be discussed. Then, the details of the thin film technique PVD (physical vapor deposition) sputtering system will be introduced. All the thin-film samples investigated in this work are deposited on substrates (eg. typically glass substrate). At last, the potential for hydrogen storage and hydrogen sensor applications will be investigated and discussed. The hydrogen storage and sensors use are based on Mg thin film hydrogen sorption properties and physical properties.

### 2.1 Hydrogen storage technologies

In our earth, most hydrogen of Earth is in compounds in water, fossil oil, organics (eg. natural gas) and so on. There are three common ways to store hydrogen including liquid hydrogen, compressed hydrogen and solid-state hydrogen storage. Both physical and chemical hydrogen interactions are involved in these storage methods, and the resulting hydrogen density is different as the hydrogen is either a molecule, or dissociated and bonded to the structure of a material (i.e. hydride). [1] When storing hydrogen gas, one must consider: gravimetric capacity, volumetric capacity as well as any safety issues. Fig 2.1.1, demonstrates a range of hydrogen storage techniques being considered for on board applications including their volumetric H<sub>2</sub> density and gravimetric H<sub>2</sub> density values. As shown in Fig 2.1.1, compressed hydrogen has a high gravimetric H<sub>2</sub> density but with low volumetric H<sub>2</sub> density thus it needs large volume tanks to store the required amount of compressed hydrogen. However, metal

hydrides (shown in red on Fig 2.1.1) have high volumetric density and low gravimetric density (eg.  $\text{LaNi}_5\text{H}_6$ ). Complex hydrides (purple) have high volumetric  $\text{H}_2$  density and middle gravimetric density (eg.  $\text{LiH}$ ). They have very high dissociation temperature. Hydrocarbon-based hydrides have high volumetric density and high gravimetric density (eg.  $\text{CH}_4$ ). Solid-state hydrogen storage (i.e. metal hydrides complex hydrides) has the highest density among all the options shown in Fig 2.1.1. The 2020, US DOE (Department of Energy) targets are for the gravimetric  $\text{H}_2$  density to be above 5.5 wt% and the volumetric  $\text{H}_2$  density is above  $40 \text{ kg H}_2 \text{ m}^{-3}$ . The material  $\text{MgH}_2$  can meet the 2020 DOE targets which have a good prospect for hydrogen storage applications. [16]

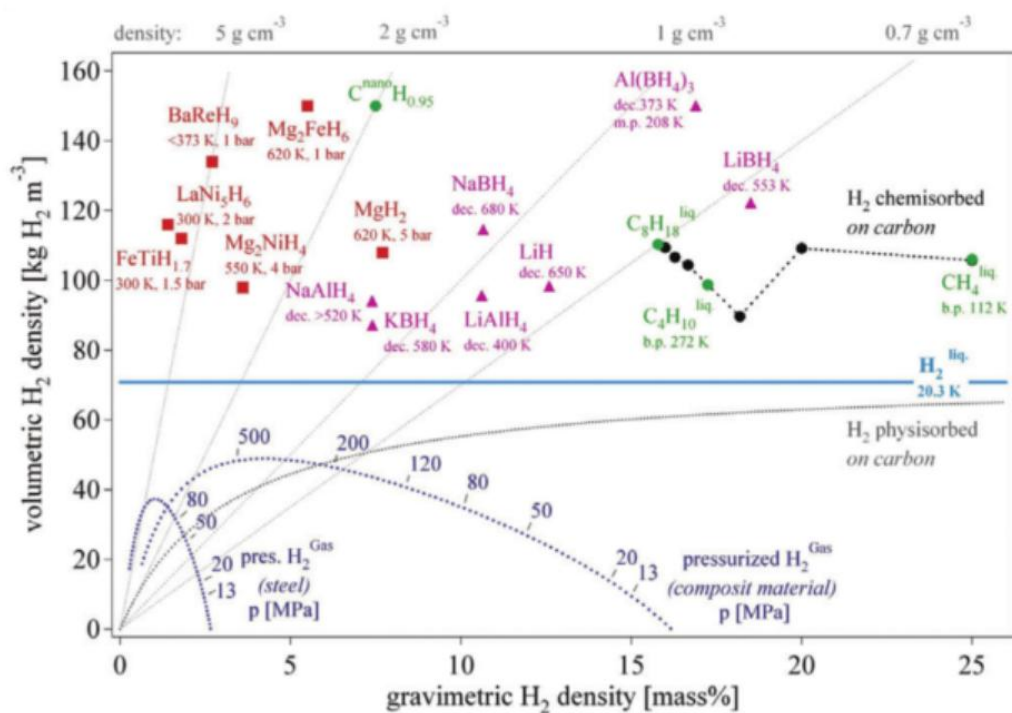


Fig 2.1.1 Volumetric and gravimetric energy densities of a range of selected hydrogen storage materials; Red – metal hydrides Purple – complex hydrides Green – carbon based hydrides Dotted lines represent theoretical densities for a compressed gas in either a mild steel or composite container. The container is not taken into account. [16]

The hydrogen gas has very low volumetric and gravimetric H<sub>2</sub> density. It is the lightest gas in the universe. So it is suitable to ideal gas law which is shown below:

$$PV = nRT \quad (1)$$

Where P is pressure in Pascal, V is volume in m<sup>3</sup>, n is the number of moles, R is the universal gas constant in J mol<sup>-1</sup> K<sup>-1</sup> and T is the temperature in °C. The equation shows the relationship among gas volume, pressure and reaction temperature. Under constant reaction pressure, the gas reaction volume increases with increasing temperature.

### 2.1.1 Liquid hydrogen storage

Liquid hydrogen storage has been used in various applications since the 1960s. The energy required for liquefaction is around the 10 kWh/kgH<sub>2</sub>. To store liquid hydrogen, a low temperature is required (less than -253 °C). Such a low temperature requires a well insulated Dewar container, constructed from metals with suitable mechanical properties at cryogenic temperatures. If the temperature inside the tank reaches the critical point, then the tank needs to have a system which can safely release gas to avoid a dangerous pressure build-up. [17] In Russia, the liquid hydrogen tank's volume is around 25 m<sup>3</sup> to 1437 m<sup>3</sup>. The weight of 25 m<sup>3</sup> hydrogen tank is about 19 tons which can store 1.75 ton hydrogen. Every day the loss of evaporation is 1.2 percent. 1437 m<sup>3</sup> liquid hydrogen weighs 360 tons which stores 100.59 tons liquid hydrogen. The loss of evaporation is about 0.13 percent every day. The liquid hydrogen system store density is also influenced by the amount of insulation required, and the free-space needed above the liquid to accommodate a partial pressure build-up during boil-off. [1] In order to try to reduce the effect of thermal losses (i.e. boil-off into hydrogen gas), liquid hydrogen storage system needs to be able to insulate with respect to thermal radiation, thermal convection and thermal conduction. [18]

### 2.1.2 Compressed hydrogen storage

As the density of hydrogen under STP (standard conditions for temperature and pressure; 0 °C and 0.1 MPa) is quite low, hydrogen can be compressed in a tank to increase the density. Compressed hydrogen tube is 11 m long with a radius of 0.3 m, and a working pressure of about 20 MPa. The pressure can reach 35 MPa and 70 MPa in compressed hydrogen applications. In China, the first compressed hydrogen supply station (35 MPa) has already been built in Shanghai. The density of compressed hydrogen is higher than the liquid hydrogen. [1] Right now, compressed gas becomes one of the options for on board hydrogen storage such as vehicles. The fuel tanks of compressed hydrogen can operate up to 70MPa, which are higher than for propane tanks (2 MPa) and compressed natural gas (25 MPa). [19] The safety of compressed hydrogen tanks is very important, and so tank integrity and the prevention of leak needs to be carefully evaluated. The formation of an explosive mixture at the high temperature can cause severe damage. [19]

### 2.1.3 Solid-state hydrogen storage

Many metals together can absorb hydrogen to form a class of compounds known as metal hydrides or complex hydrides. These hydrides can discharge hydrogen when needed by raising the temperature and reducing the pressure. Some well-known alloys such as LaNi<sub>5</sub>, and TiFe have good hydrogen cycling properties and high volumetric hydrogen storage capacities, however, they have low volumetric hydrogen storage capacities (<2 wt %) which is not satisfactory for vehicular applications. Magnesium (and Mg alloys) is interesting because of their relative low price and relatively high abundance and a maximum and a maximum reversible gravimetric hydrogen storage capacity of 7.6 wt%. However, the main drawbacks for MgH<sub>2</sub> are its sluggish hydrogen sorption kinetics, high thermodynamic stability and high desorption temperature (above 350 °C). MgH<sub>2</sub> powders need to heat up

above 350 °C in order to obtain satisfactory hydrogen sorption properties. The chemical reaction is shown below:



The hydrogen sorption kinetics of these MgH<sub>2</sub> powders can be improved by: ball-milling; and adding an appropriate surface catalyst such as (e.g. such as NbF<sub>5</sub> or Nb<sub>2</sub>O<sub>5</sub>). Ball-milling a mixture of MgH<sub>2</sub> and 1 mol% NbF<sub>5</sub> can increase the reaction kinetics; based on XRD analysis, NbF<sub>5</sub> melts during the high energy ball milling resulting in the formation of a Nb hydride film covering the powder particles. [21] In addition, the ball-milling process can also reduce the grain size within the powder particles. This increase in the volume of grain boundaries can significantly improve the hydrogen sorption properties, i.e. lower sorption temperature and/or more rapid sorption kinetics. The hydrogen desorption temperature can be reduced to about 150 °C. In absorption and desorption process, some oxide additions such as Nb<sub>2</sub>O<sub>5</sub>, TiO<sub>2</sub>, V<sub>2</sub>O<sub>5</sub>, Cr<sub>2</sub>O<sub>3</sub> and Fe<sub>3</sub>O<sub>4</sub> have the catalyst effect. Among these catalysts, the composites materials containing Fe<sub>3</sub>O<sub>4</sub> has the fastest kinetics in the reaction. Besides, Al + MgH<sub>2</sub> system can be useful to improve thermodynamics such as reducing hydrogen desorption temperature. The Mg-Al alloy can be expected as one of the alloy system which can improve the kinetics and thermodynamics. [4, 20, 21, 22, 23, 24, 25, 26] However, current solid-state hydrogen storage materials have gravimetric hydrogen storage capacities which are too low and sorption temperatures that are too high. Solid state hydrogen storage materials can include powders or thin films. Thin film can be defined as a layer of material ranging from fractions of a nanometer to several micrometers in thickness. In order to achieve a high hydrogen storage capacity and a suitable hydrogen sorption temperature for thin films, it has been shown that nano-composite hydrogen absorbing materials can be designed. In previous work, nano-composite two layered Pd/Mg and three layered Pd/Mg/Pd were prepared using an RF-associated magnetron sputtering method.

Chemisorbed hydrogen atoms sit in interstitial locations within a metal lattice. Hydrogen to metal concentration (H/M) of around 0.1 usually achieves in this  $\alpha$ -phase. Figure 2.1.2 illustrates the Van't Hoff equation. The enthalpy and entropy are represented in this equation. Hydride phase starts to nucleate at the start of the plateau (i.e. at about 0.1 H/M at 25 °C in Fig 2.1.2). At 0.85 H/M it is 100% hydride phase. The reaction is  $Mg+H_2 = MgH_2$ . In this reaction, it is reversible based on different conditions. When the Gibbs free energy ( $\Delta G$ ) is negative, the reaction below occurs.  $\Delta H$  is the enthalpy change and  $T$  is temperature.  $\Delta S$  is the change in entropy. The relationship among  $\Delta G$ ,  $\Delta H$  and  $\Delta S$  is proposed by author Gibbs which is shown below:

$$\Delta G = \Delta H - T\Delta S \quad (2)$$

Another form of this equation is shown below:

$$\Delta G = -RT\ln K \quad (3)$$

$R$  is the universal gas constant and  $K$  is the chemical equilibrium constant. By connecting these two equations, we get the relation and final equation:

$$\ln K = \frac{\Delta H}{RT} - \frac{\Delta S}{R} \quad (4)$$

This is the Van't Hoff equation. In the case of Metal – Hydrogen interactions, the equilibrium constant,  $K$  is proportional to  $-1/T$ . As the pressure is related to temperature,  $K$  is related with  $P/P_0$ . The equation can be written as equation:  $y = mx + c$ . The plot of  $\ln K$  against  $1/T$  will provide the graphical solution of the equation where the gradient is  $\Delta H/R$  and the intercept is  $\Delta S/R$ , known as a van't Hoff plot. As the hydrogen concentration increases, the amount of  $\alpha$  phase increases. At a critical pressure (e.g. about 1 bar at 25 °C in Fig 2.1.2) the amount of  $\alpha$  phase reaches a maximum, and  $\beta$  phase begins to form. Then  $\alpha + \beta$  phase will transform to  $\beta$  phase at last at high  $C_H$  (H/M at 25 °C). This plateau pressure is temperature dependent. the pressure increases with increasing temperature.

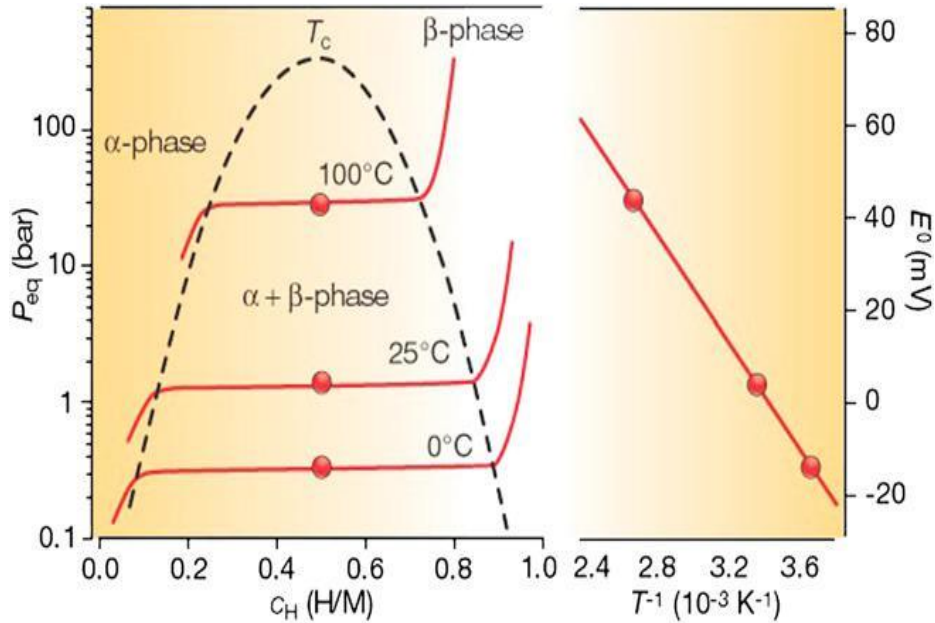


Fig 2.1.2 Pressure – composition – temperature curve and corresponding with Van't Hoff plot  
 The construction of a Van't Hoff plot is shown on the right hand side, with the gradient denoting  $\Delta H/R$  and gradient  $\Delta S/R$ . This is very useful in the characterization of hydrogen storage materials. Above the critical temperature,  $T_c$ , the two phase region ( $\alpha + \beta$ ) disappears and hydrogen exists only as a solution in metals. The Van't Hoff plot is shown in the equation.  $\ln \frac{P_{eq}}{P_{H_2}} = \frac{\Delta H}{RT} - \frac{\Delta S}{R}$   $P_{H_2}$  is standard pressure  $1.013 \times 10^5$  Pa. [4]

As shown in Fig 2.1.3, the bonding in  $MgH_2$  is partially covalent with an elongated H ion instead of purely ionic character. The charge density map for  $MgH_2$  planar surfaces are shown below. The density map indicates that there it is a degree of covalent bonding. The scale shows the electron density surrounding of Mg atoms (shown as red) and hydrogen atoms (shown as yellow).

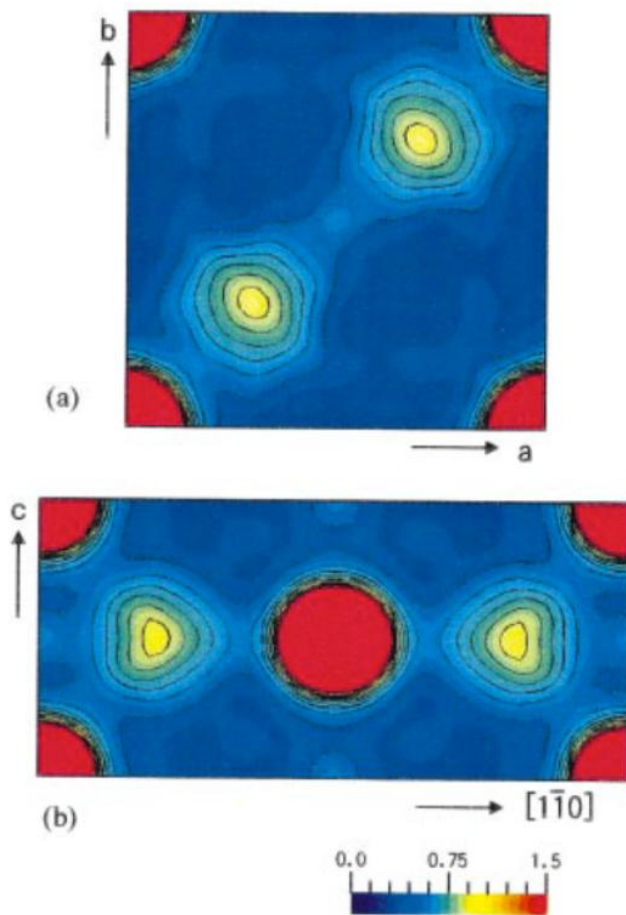


Fig 2.1.3 Electron charge density maps of MgH<sub>2</sub> planar surfaces – a) 001 projection and b) 110 projection The scale shows the electron density surrounding Mg atoms (shown as red) and hydrogen atoms (shown as yellow). At the bond midpoint, the electron density is around 0.26 e/A<sup>3</sup> which is larger than a typical Li-H ionic bond length (0.12 e/A<sup>3</sup>), but smaller than a typical Si covalent bond (0.7 e/A<sup>3</sup>). The electron densities surrounding the Mg and H atoms are distorted, indicating a degree of covalent bonding instead of purely ionic character. [27]

As shown in Fig 2.1.4 (c) and Fig 2,1,4 (d), metal absorbs hydrogen to form metal hydride and release hydride to become metal at high temperatures and pressures ( $P \gg P_{eq}$ ). Hydrogen pressure is important considering the practical applications. This is possible onset of H-H interactions required for the formation of the hydride phase.  $2M + H_2 = 2MH$  Reaction kinetics mechanisms are different in different conditions.

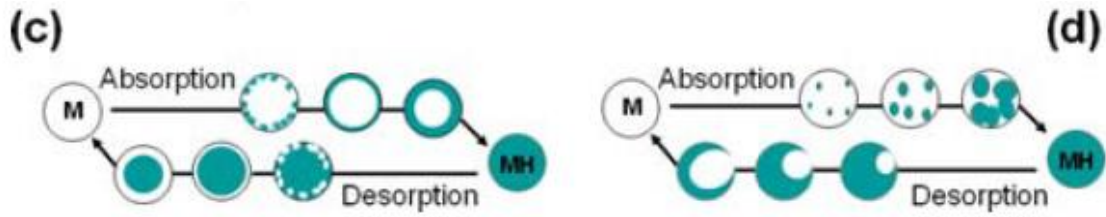


Fig 2.1.4 (c) at high temperatures and pressures ( $P \gg P_{eq}$ ), and (d) at low temperatures and similar to the equilibrium pressures Note the nucleation and growth behavior differs significantly between a core shell model and a random nucleation pattern. [28]

In Table 1, both gravimetric density and volumetric density of different materials are shown.  $\text{LiBH}_4$  has the highest gravimetric density among these materials, which is around 18.4 wt%. Different solid state media has various gravimetric densities to store hydrogen. Liquid hydrogen need to be stored far lower than room temperature with moderate pressures. Compressed hydrogen is far higher than 1 bar. Solid state hydrogen storage method needs high temperatures or pressures not including Fe-Ti and  $\text{LaNi}_5$ .  $\text{NH}_3$  liquid is practically irreversible.

Table 2.1 Hydrogen content of different media [28]

Medium	Gravimetric density (mass %)	Volumetric density/kg L <sup>-1</sup>	Conditions for reversible hydrogen storage
$\text{H}_2$ gas 700 bar	100	0.03	Near room temperature with moderate pressures
$\text{H}_2$ liquid	100	0.07	
FeTi	1.5	6.50	
$\text{LaNi}_5$	1.5	8.25	
$\text{ZrV}_2$	3.0	—	Needs high temperatures and/or pressures
$\text{NaAlH}_4$	5.5	1.24	
$\text{MgH}_2$	7.6	1.40	
$\text{Mg}_2\text{NiH}_4$	3.8	2.60	
LiH	12.7	0.80	
NaH	4.2	1.40	
$\text{AlH}_3$	10.1	1.48	
$\text{TiH}_2$	4.0	3.80	
$\text{LiAlH}_4$	10.5	0.92	
$\text{LiBH}_4$	18.4	0.12	
$\text{NH}_3$ liquid	17.7	0.60	Practically irreversible
$\text{H}_2\text{O}$	11.1	1.00	

Physisorption is an alternative approach to store hydrogen molecules using materials. Physisorption uses van der Waals attractions between hydrogen molecules and materials surfaces, instead of chemical bonding with dissociated hydrogen. The lower energy bonding means that an appreciable storage capacity can only be achieved at lower temperatures (usually, -200 to -150 °C). Common micro-porous high-surface area materials used for physisorption are metal organic frameworks (MOFs), carbons (eg. nanotubes, fullerenes) and zeolites. For zeolites, hydrogen storage capacity at room temperature was reported to be less than 0.1 wt%. [29]

In Fig 2.1.5, hydrogen sorption in magnesium (as an example) is a heterogeneous solid gas reaction. It involves different energy barriers which can retard the hydrogen sorption process. The gas phase is absorbed at the magnesium surface. Hydrogen molecules dissociate and then diffuse into the subsurface. For bulk materials, diffusion is the process by which hydrogen enters the metal. Nucleation of the hydride phase occurs in the bulk materials.

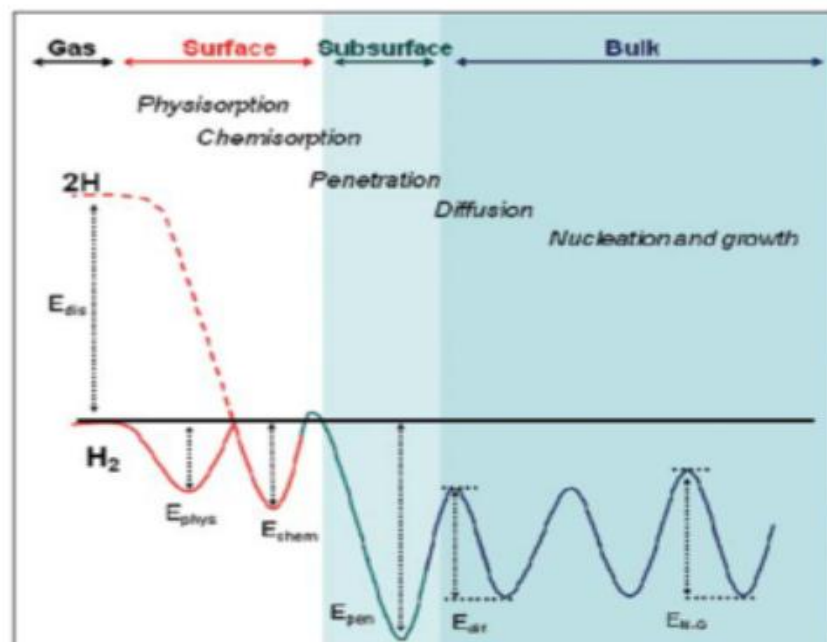


Fig 2.1.5 Lennard-Jones potential diagram corresponding to the successive energy barriers encountered by hydrogen during absorption and desorption in a metal.  $E_{\text{phys}}$ : energy for hydrogen physisorption,  $E_{\text{chem}}$ : energy for hydrogen chemisorption,  $E_{\text{pen}}$ : energy for hydrogen

penetration in the subsurface,  $E_{\text{dif}}$ : energy for hydrogen diffusion in the bulk, and  $E_{\text{N-G}}$ : energy for the nucleation and growth of the hydride phase [28]

As shown in Fig 2.1.6, two intrinsic parameters in hydrogen sorption reaction can improve the hydrogen storage performance of a material: the formation enthalpy  $\Delta H$  and the activation energy. The reaction is  $M+H_2 \leftrightarrow MH_x$ . There are some approaches to try to improve the hydrogen storage properties: (1) Modifying the compositions (2) nano-scaling the hydrides (3) catalyzing the hydrogenation and dehydrogenation by additives doping and/or (4) changing the reaction pathways. [29]

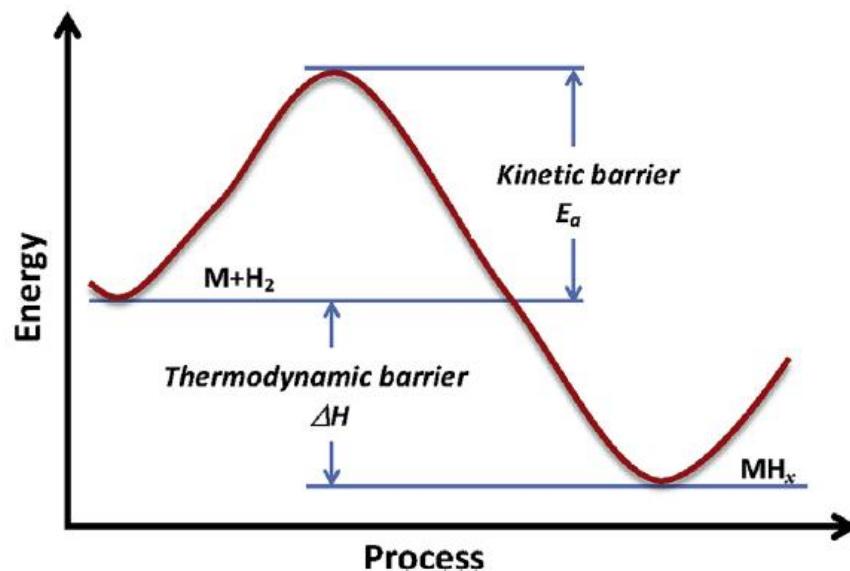


Fig 2.1.6 Schematic illustration of thermodynamic and kinetic barriers for hydrogenation and dehydrogenation reactions of metal hydrides [29]

In Fig 2.1.7, both TG curves with  $NbF_5$  and without catalyst are shown. The catalyst has less influence on the hydrogen storage capacity. Both curves show a wt% capacity of around 6.3 wt%. A catalyst can improve the hydrogen sorption kinetics which means the reaction can happen more rapidly and at a slightly lower temperature. With the addition of  $NbF_5$ ,  $MgH_2$  can dissociate hydrogen at 475 K, compared to 600 K without a catalyst,  $MgH_2$ . [21]

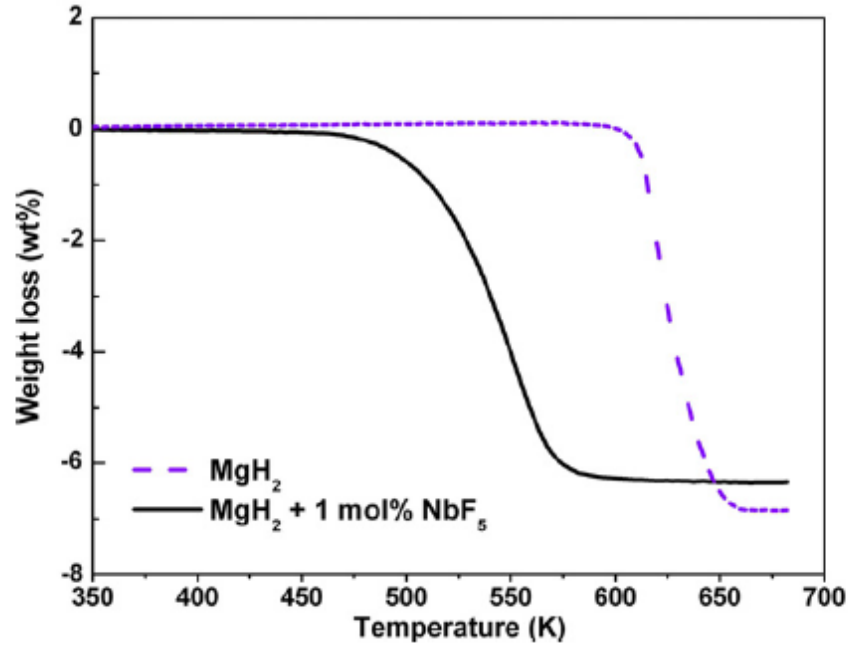


Fig 2.1.7 TG curves of MgH<sub>2</sub> (a) with NbF<sub>5</sub> and (b) without the catalyst [21]

## 2.2 Hydrogen sorption properties of magnesium

The hydrogen sorption process includes hydrogen absorption and hydrogen desorption. For MgH<sub>2</sub> powder, it is dehydrogenated first to release hydrogen. Then it is hydrogenated at a different temperature to absorb hydrogen. For the Mg based thin film, it can hydrogenate first at room temperature and dehydrogenate at a higher temperature around 150 °C. The hydrogen capacity can reduce after increasing the number of hydrogen cycle.

Nanoscaling referring to powders is shown to have a large effect on improving the thermodynamics and kinetics of Mg based alloys due to surface and boundary effects. Hydrogen release from bulk MgH<sub>2</sub> particles is based on growth of Mg crystallites within the MgH<sub>2</sub> matrix. In thin film samples, dehydrogenation occurs by a ‘shrinking core’ mechanism as shown in Fig 2.2.1. The nucleation and growth happen on MgH<sub>2</sub> thin film surface. The enlarged Mg grains during the dehydrogenation of bulk sample can be seen. [29]

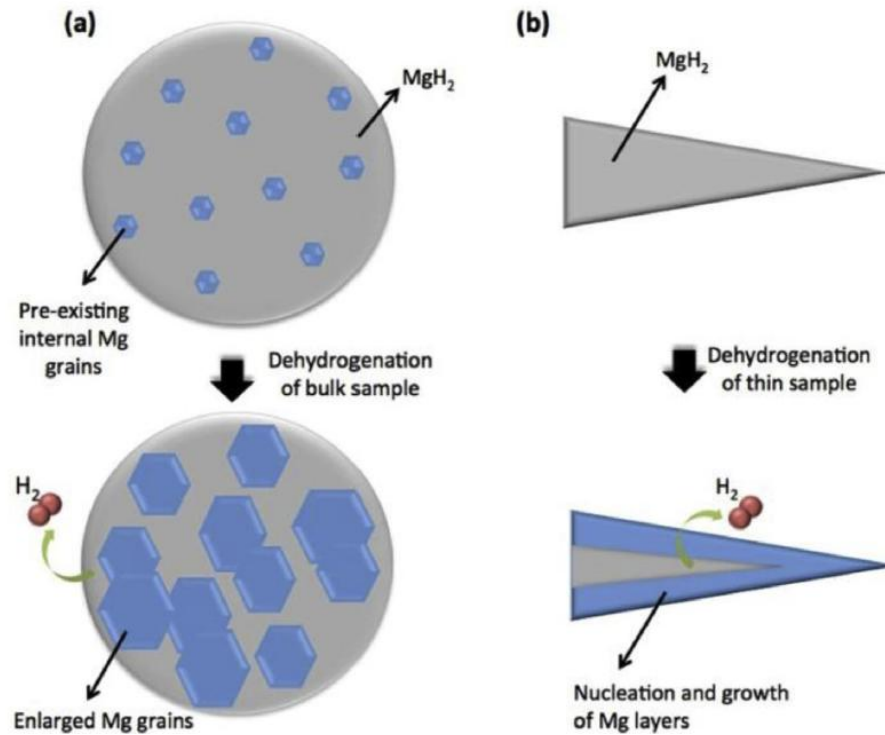


Fig 2.2.1 Schematic hydrogen release mechanisms from a MgH<sub>2</sub> grain (a) nucleation and growth model for bulk MgH<sub>2</sub> grains and (b) shrinking core model for thin film MgH<sub>2</sub> samples [29]

The phase diagram of Mg-H system at 1 bar is shown in Fig 2.2.2. Temperature above 570 K, there will be no MgH<sub>2</sub> formation. From 300 K to 550 K, Mg-hcp will appear with H mole fraction lower than 0.65. MgH<sub>2</sub> forms in the whole H mole fraction. Above 922 K, the gas and liquid phase will be shown in Fig 2.2.2. At high temperatures, only the gas phase is formed.

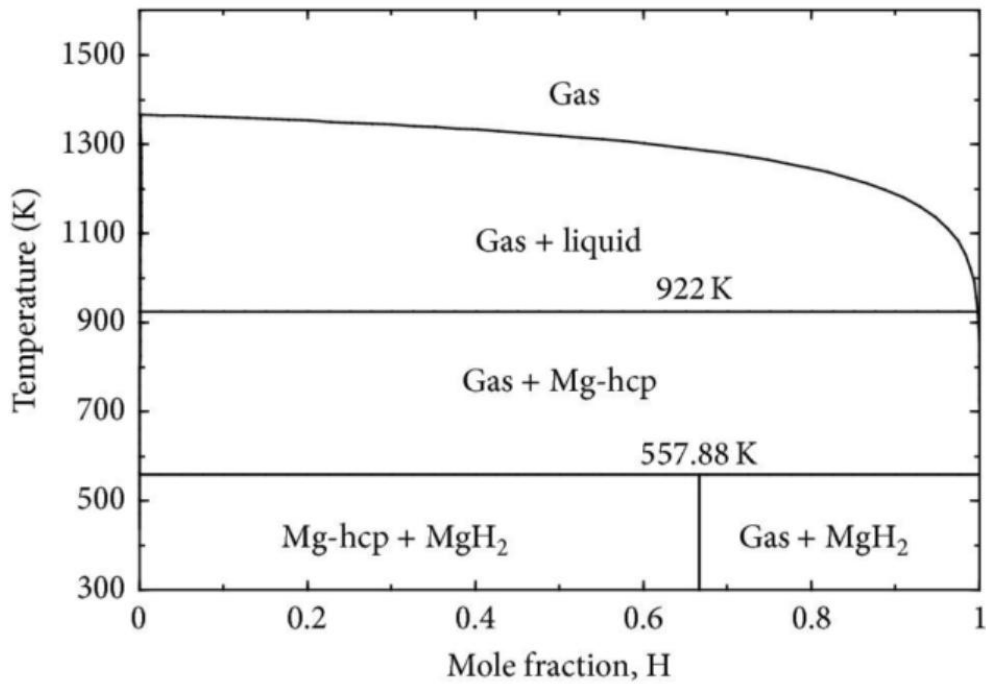


Fig 2.2.2 Binary phase diagram for the Mg-H system at 1 bar H<sub>2</sub>. The dissociation temperature of around 570 K is consistent with the published literature. [30]

According to the Mg/Pd binary phase diagram (Fig 2.2.3), Pd can be alloyed with Mg to form compounds. These compounds change with Mg composition and temperature. Compounds such as Mg<sub>3</sub>Pd, MgPd and Mg<sub>5</sub>Pd<sub>2</sub> can form in different Mg% conditions.

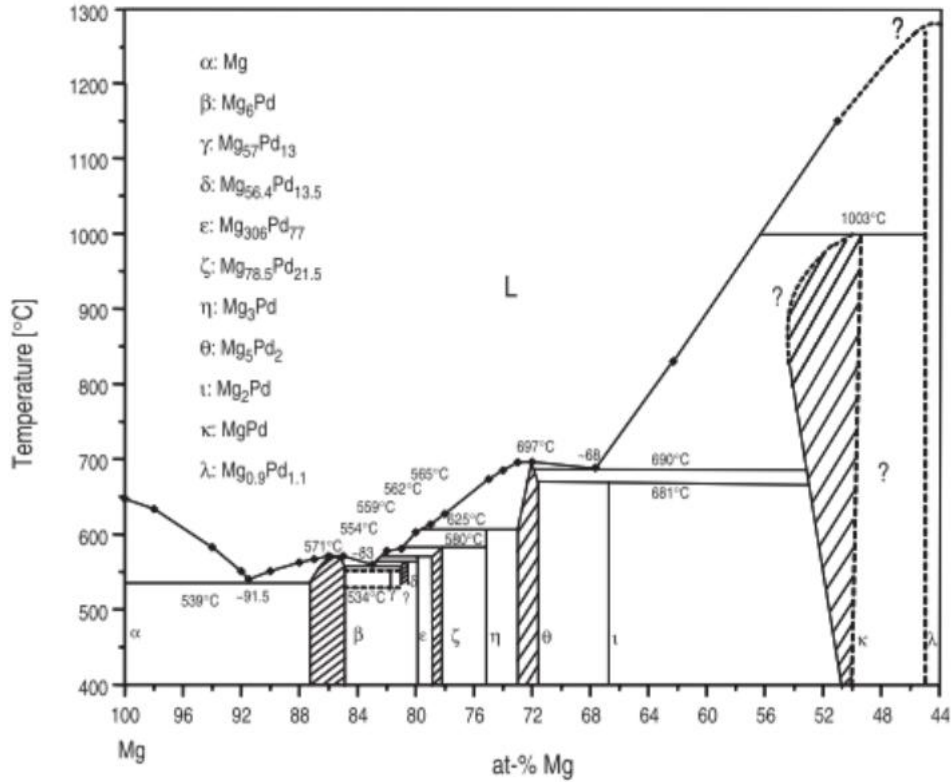


Fig 2.2.3 Binary phase diagram of the Pd-Mg according to data from this study; only data points obtained from thermal analysis measurements are shown in this graph. Phase labels are in Pd-rich two phase fields. [31]

Fig 2.2.4 shows the sorption behavior of a conventional Mg powder sample with a particle size between 50 – 100 microns. After annealing at 350 °C and hydrogenation at 400 °C were any absorption shown in the conditions. The hydrogen capacity is below 2 wt% under 400 °C and 10 bar H<sub>2</sub>. Under the 300 °C, the reaction does not occur. This illustrates how the reaction conditions can influence the hydrogen reaction process.

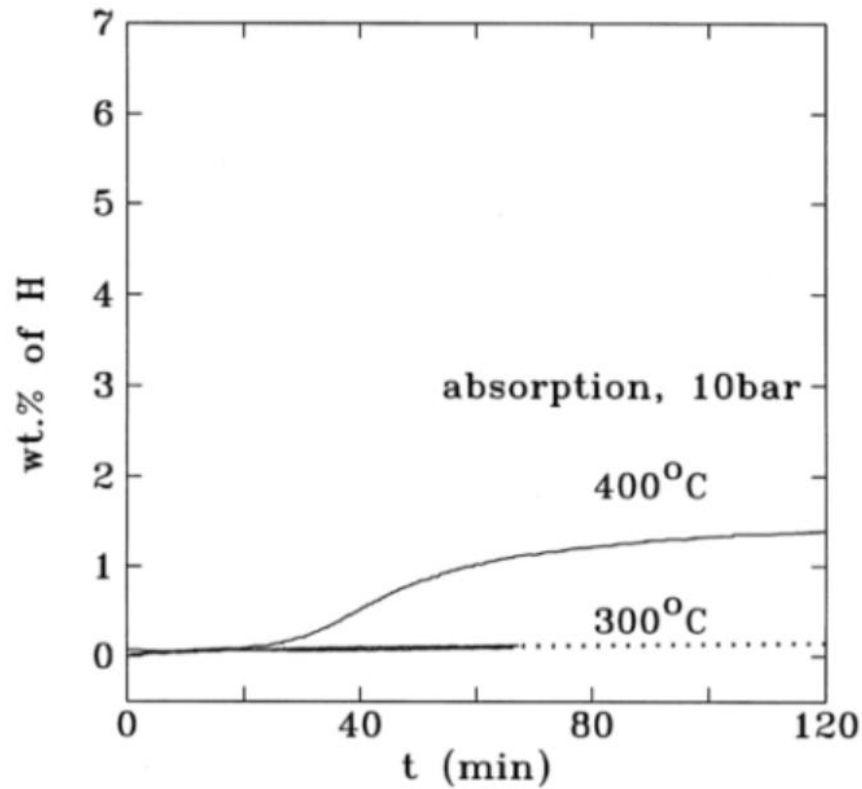


Fig 2.2.4 Hydrogen absorption in conventional magnesium powder at 300 and 400 °C at 10 bar H<sub>2</sub> pressure Absorption capacity is limited to 1.5 wt%. [32]

The desorption temperature of nano-composites MgH<sub>2</sub> was measured in Fig 2.2.5. Without catalyst, the desorption temperature was about 700 K. Upon milling MgH<sub>2</sub> and Al, hydrogen desorption temperature was reduced to 550 K. Desorption properties were improved. In sample (I) and (II), the peaks are broad. The desorption peak of sample (IV) was about 370 K. TDS trace of sample (III) has two peaks which are around 495 K and 515 K. TDS trace of sample (IV) has two peaks which are around 350 K and 550 K. This result indicates two endothermic peaks in hydrogen desorption process.

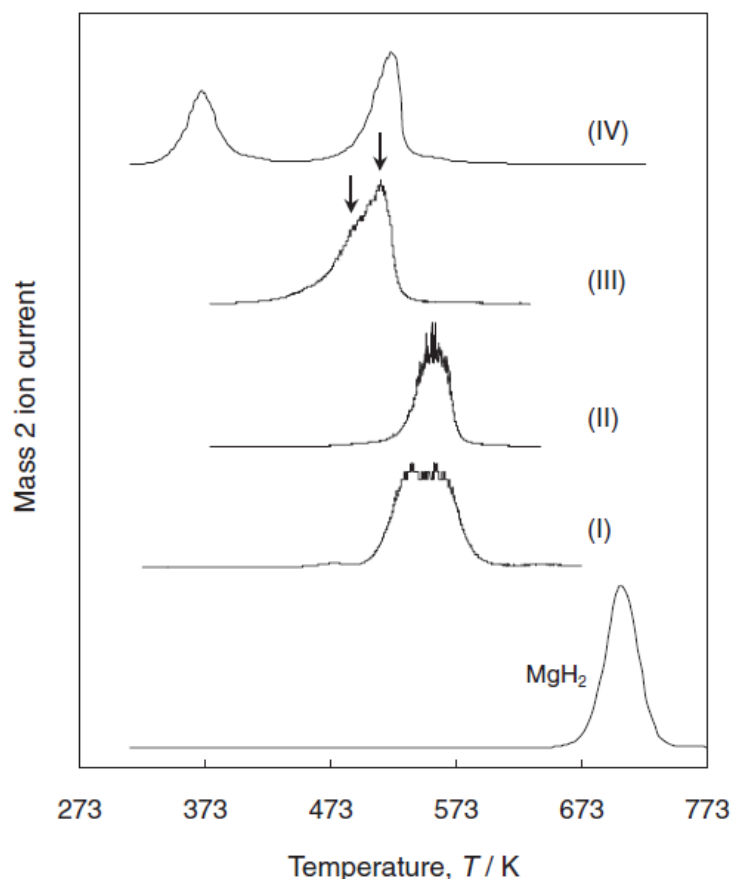


Fig 2.2.5 TDS of the nano-composites  $\text{MgH}_2/\text{Al}$  (I),  $\text{MgH}_2/\text{Al}$  (II),  $\text{MgH}_2/\text{Al}$  (III) and  $\text{MgH}_2/\text{AlH}_3$  (IV) in comparison with that of  $\text{MgH}_2$  (milled without additives) [33]

The TPD-MS H-desorption curves in Fig 2.2.6 (a), show that Mg based thin hydride films have a lower desorption temperature than bulk  $\text{MgH}_2$ . Thicker Mg films have a lower hydrogen desorption temperature. Thinner films ( $d < 150$  nm), can completely hydride, to form  $\text{MgH}_2$  throughout the film (Fig 2.2.6 (b)). While films ( $d > 150$  nm) cannot fully form  $\text{MgH}_2$ . Fig 2.2.6 (b) also shows that hydrogen content increased for Mg film thickness up to 150-200 nm. Mg thin films with  $d > 200$  nm can show a practically constant amount of H into films. Under the Mg thickness of 530 nm, the hydrogen capacity is the highest among all the samples. The hydrogen capacity is about 20 mol  $\text{H}_2/\text{mm}$  measured by TPD-MS spectra under 11 bar at 280 °C.

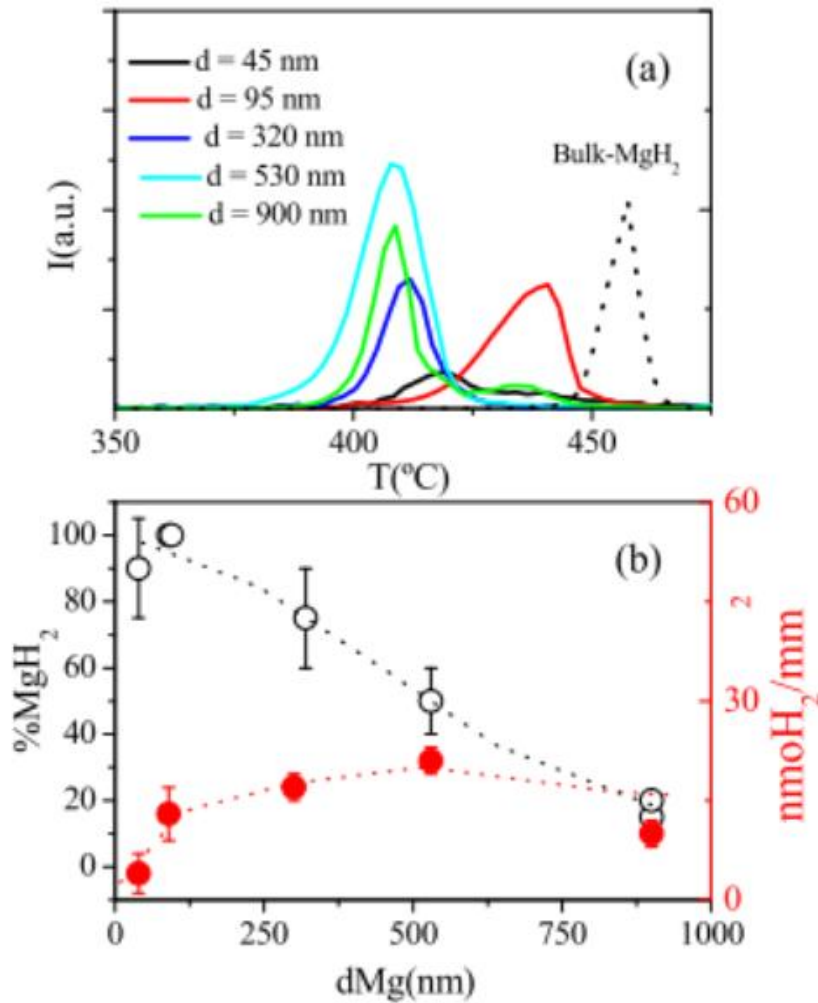


Fig 2.2.6 (a) TPD-MS spectra of Mg films hydrogenated under 11 bar pressure at 280 °C. Thickness varies from 45 nm up to 900 nm. A spectrum of MgH<sub>2</sub> is included for comparison purposes. (b) Influence of Mg thickness on MgH<sub>2</sub> (wt %) and mol H<sub>2</sub> / mm<sup>2</sup> in hydrogenated films. Dot lines are guidelines. [34]

### 2.3 Mg thin film

Thin film is a kind of film in which the thickness is lower than 1 micron ( $< 1000$  nm). The main advantages and disadvantages of thin films metal hydrides are indicated by the authors Baldi and Dam which are shown below [35]:

- The thin film can control the microstructure such as column width and thin film thickness by controlling the deposition parameters (Argon flow & Base pressure)
- Co-deposition of immiscible metals can form new phases in the thin film state which is not readily achievable in bulk materials
- Samples with a large range of compositions can be characterized quickly using combinatorial techniques

Besides, the thin film approach suffers from a few drawbacks as well which is shown below:

- The hydrogen capacity of samples is very low which makes it difficult to measure, except by TPD.
- Thin film has less surface area than powders which reduces the hydrogen sorption kinetics.
- Comparing to powder samples, the thin films characterization can be quite difficult due to low hydrogen capacity and high volume and weight of the substrate. It is not easy to peel off Mg based the thin films from the substrate in the experiment.

However, it is shown that thermodynamics and sorption behavior can be quite different compared to bulk materials. Both the advantages and disadvantages are discussed. The aim of this research is to expand the advantages of the thin films and to try to overcome some of the disadvantages of the Mg based thin films.

### 2.3.1 Overview of Mg thin film for hydrogen storage

Mg thin films include Pd top layer, Mg thin layer and substrate (eg. glass substrate) Pd layer should be coated on top to avoid formation of a Mg layer oxide. Pd top layer acts as the catalyst, which can enhance the hydrogen dissociation and recombination. [36] The main

advantages of thin film systems are reviewed by Baldi and Dam from recently published research and are shown below.

XRD patterns for Pd/Mg/Pd thin films before hydrogenation are shown in Fig 2.3.1. The Mg (002) and Mg (004) diffraction peaks were observed which is similar with two-layered Pd/Mg films. Pd (111), Pd (200) and Pd (220) are also shown in Fig 2.3.1. The profiles indicate a c-axis preferred orientation for the Mg films. It is shown that the intensity of the Mg (002) peak decreases with decreasing Mg thickness and there is no Mg peak observed in film (a) with the Mg thickness of 25 nm. The broad maximum around  $25^\circ$  is the glass substrate. A thicker film has a higher Mg peak intensity.

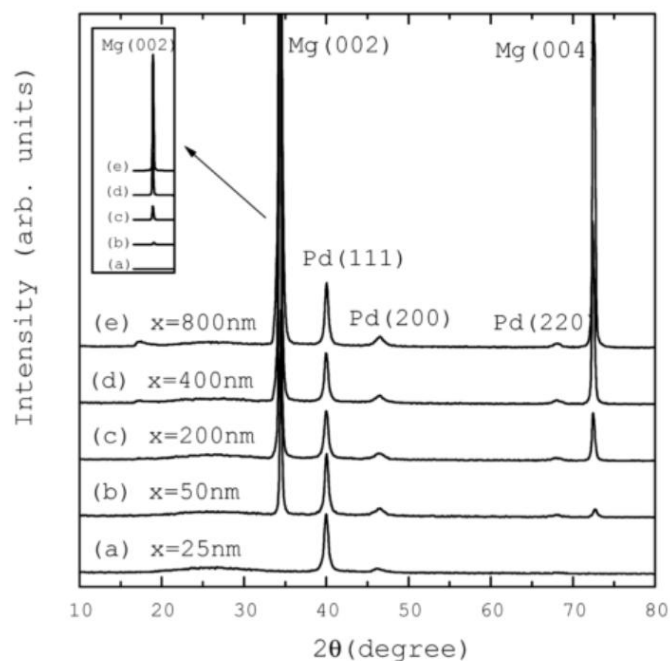


Fig 2.3.1 X-ray diffraction profiles of sample Pd(50 nm)-Mg(x nm)-Pd(50 nm) glass substrate with  $x = 25, 50, 200, 400$  and  $800$  nm before hydrogenation. The broad peak near the range  $20-30^\circ$  is that of the glass substrate. [37]

### 2.3.2 Control of microstructure during sputtering

The sputtering parameters can be controlled in order to modify the Mg-based thin film microstructure. As an example, the working pressure, target bias voltage, base pressure, rotation speed and sputtering current are possible to control. The width of the Mg columnar grains microstructure can be controlled via various sputtering parameters such as bias voltage and base pressure. Controlling Mg film thickness is another method of tailoring the composition and degree of crystallization. It is reported that Pd-Mg (40nm)-Pd film shows the best hydrogen absorption and desorption kinetics comparing with other thickness samples. This film can finish absorption hydrogen in around one minute in  $4 \times 10^3$  Pa H<sub>2</sub> at 298 K. This film can fully dehydrogenate about 25 min. When the thickness of the Mg layer was less than 60 nm, the hydrogenation rates increased. [38]

As shown in Fig 2.3.2, all the images are made using SEM. It is observed that the 325 mesh Mg sample has a particle size of around 40 - 50  $\mu\text{m}$ . In Fig (b), the particle size is from 100 to 700 nm with a mean size about 300 nm. Mg<sub>50</sub>Co<sub>50</sub> alloy ball milled for 100 h has a BCC structure with the particle size 1 to 3  $\mu\text{m}$ . In Fig (d), a typical cross section image indicates a layer thickness of 84 nm and the crystallite size is around 50-100 nm (Fig (e)). Finally, Pd capped Mg thin film has a plate like structure. In Fig (f), the crystallite size is around 200-250 nm in the SEM image. This represents the Pd crystallite size. Pd top layer indicates hexagonal plate like structure.

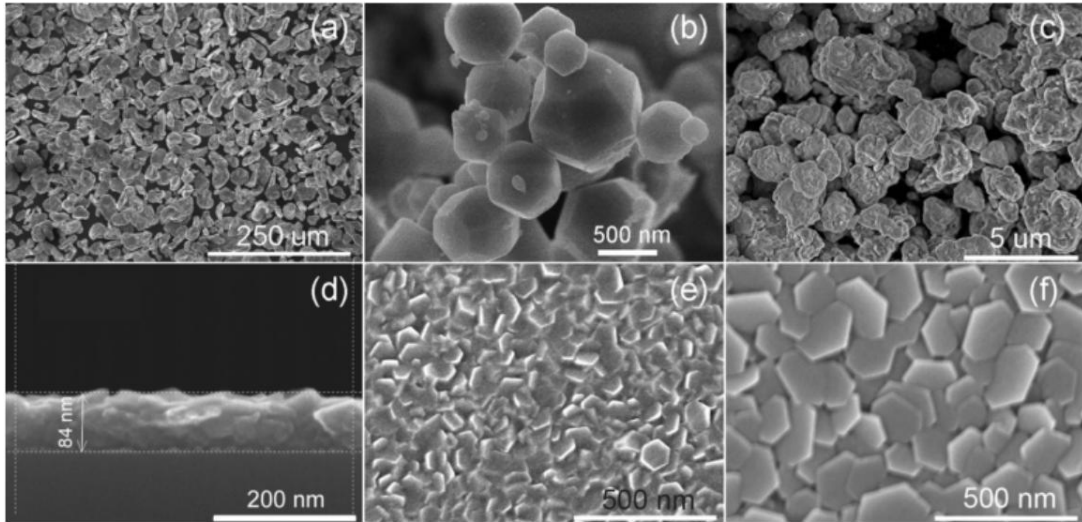


Fig 2.3.2 SEM sample images (a) 325 mesh Mg, (b) Mg nano-particle sample, (c) milled  $Mg_{50}Co_{50}$  BBC alloy, (d) cross section observation of Mg thin film without Pd layer, (e) top picture of Mg thin film without Pd layer and (f) top picture of Pd capped Mg thin film. [39]

Island growth modes occur during deposition that depends on the contact angle. Three typical microstructures are due to different growth modes are represented schematically in Fig 2.3.3. The three microstructures can be influenced by the PVD conditions such as target potential, saturation pressure and the reaction temperature. Changing the target potential influences the free energy of atoms for particle coalescence. The substrate bias voltage can influence the microstructure in the same way. The saturation pressure influence the amount of nucleation sites. Increasing saturation pressure can increase the nucleation sites. Finally, the temperature can affect the rate of nucleation. The films tend to grow in columns. The deposition temperature affects the properties such as microstructure of the Mg thin films. The deposition temperature changes will lead to the change of microstructure.

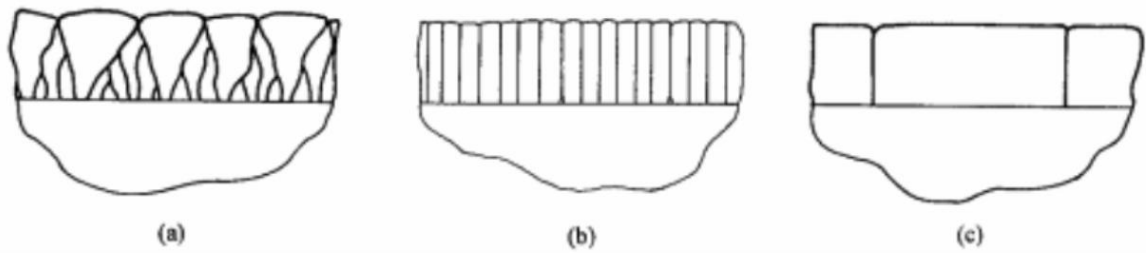


Fig 2.3.3 Potential microstructures of the thin film < 1 micron in thickness deposited by PVD systems Type (a) is often seen with the highest nucleation rates. Type (b) is often seen after grain boundary motion has occurred due to coalescence. Type (c) is observed by a high degree of coalescence and film thickening [40]

Sputtered thin films are shown schematically in Fig 2.3.4 (a). Fig 2.3.4 (b) shows how the thin films deform due to hydrogen sorption. Compressive stress and tensile stresses accumulate during the hydrogenation process. As shown in Fig 2.3.4 (c), this indicates that the transition metal layers form nano-crystallites due to the breaking up of the samples into fine flaky powder. The mechanism of film transformation changes after adding transition metals. [41]

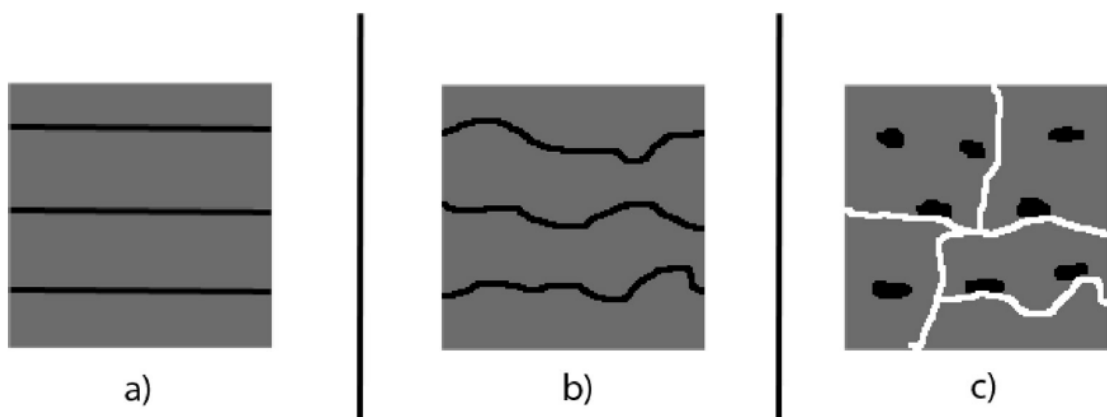


Fig 2.3.4 Schematics show suggested mechanism of thin film transformation: a) as deposited coating, b) deformation after hydrogen cycling, and c) transition metal layers forming nano-crystallites [41]

TEM images of samples Pd(25nm)-Mg(200nm) and Pd(50nm)-Mg(200nm)-Pd(50nm) before hydrogenation are shown in Fig 2.3.5. The boundary of Pd and Mg can be clearly observed. Mg is composed of thin columnar grains. The column width of the Pd(25nm)-Mg(200nm) sample is about 70 nm. Pd(50nm)-Mg(200nm)-Pd(50nm) has around 20 nm column width which far smaller than sample Pd(25nm)-Mg(200nm) thin film. This indicates that a sandwich structure has an influence on the Mg columnar width, i.e. that the Mg layer structure is changed by its foundation layer. The TEM results also show that the structure of Mg in Pd/Mg/Pd films is composed of columnar grains with a width of about 30 nm. Smaller Mg columnar width has better hydrogen storage properties (i.e. reduced hydrogen sorption temperature) than the larger width samples.

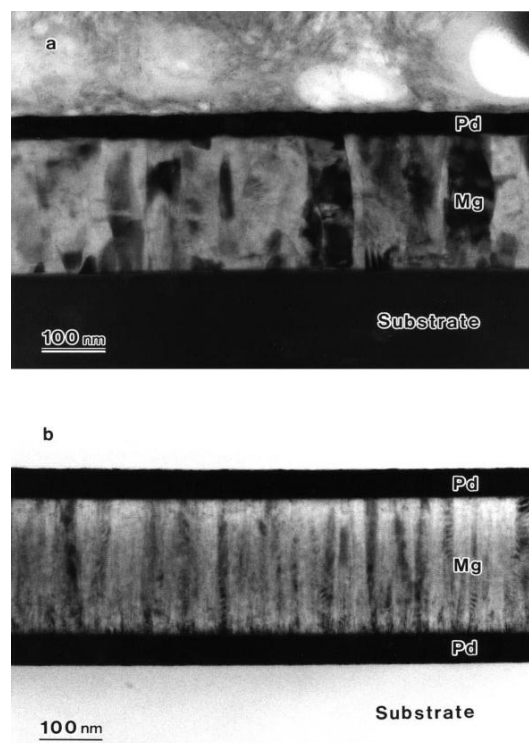


Fig 2.3.5 TEM micrographs for the cross section of sample (a) Pd (25 nm)-Mg (200 nm) and sample (b) Pd (50 nm)-Mg (200 nm)-Pd (50 nm) films before hydrogenation [37]

After the Mg thin films were hydrogenated at 10 bar of hydrogen during 20 h at 100 °C. MgH<sub>2</sub> peaks with (110), (101) and (211) miller plane were observed in Fig 2.3.6 (a). Concerning the microstructure, the crystallite size of MgH<sub>2</sub> was calculated to be 80 ± 40 nm

using the Scherrer formula. In Fig 2.3.6 (b), the SEM images show grains in close contact, with a grain size of around 200 nm, i.e. higher than the estimate based on XRD.

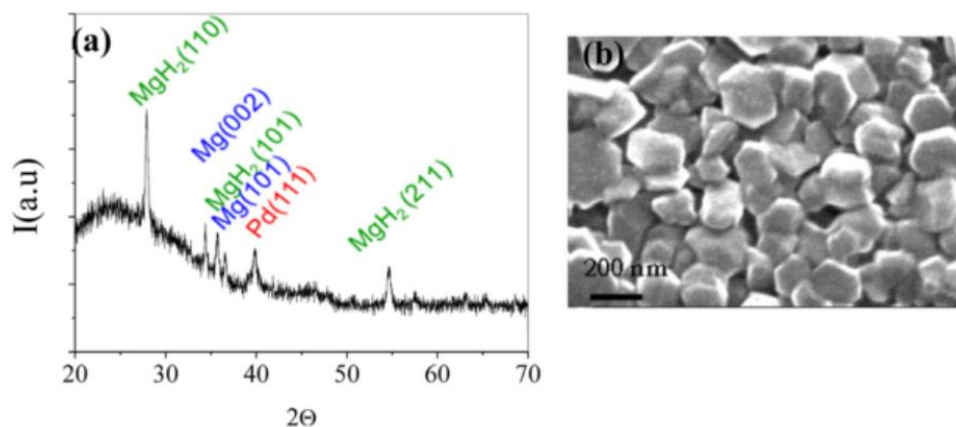


Fig 2.3.6 (a) XRD pattern of Pd capped  $\text{MgH}_2$  thin film and (b) SEM image of Pd-capped of  $\text{MgH}_2$  surface [42]

### 2.3.3 Stress effect (compressive stress and tensile stress)

$\text{Pd/Mg/Pd}$  thin film was deposited onto a glass substrate (Corning #7059;  $20 \times 20 \times 0.5$  mm) with nano-meter scales layers. During heating, hydrogen absorption leads to a volume expansion causing compressive stress in the  $\text{MgH}_2$  lattice. An anisotropic deformation results in compression on the Mg film plane. Without the film peeling off, stress accumulates during the hydrogen absorption process. The compressive stress is on the surface of Mg. During hydrogen desorption (Fig 2.3.7), the Pd top layer can avoid oxidation and enhance hydrogen dissociation and recombination. Hydrogen molecules released from thin film sample to form hydrogen molecules which leads to a small contraction. The volume of Mg thin film expands up to 10% due to  $\text{MgH}_2$  formation. Stain is generated between Mg and the substrate. The contraction of the  $\text{PdH}_x$  layers to Pd causes compressive stress in the  $\text{MgH}_2$  lattice. Mg exhibits a martensite-like transformation. The distance between Mg atoms are expanded 22% and the Mg-Mg distances are expanded only 6% in substrate plane. An anisotropic

deformation provides compressive stress. At the same time, stress accumulates on the Mg layer. Mg (001) plane corresponds to the MgH<sub>2</sub> (hh0) plane. Desorbing hydrogen atoms can diffuse through the thin film and form at the film surface to form hydrogen molecules in the desorption process. [37]

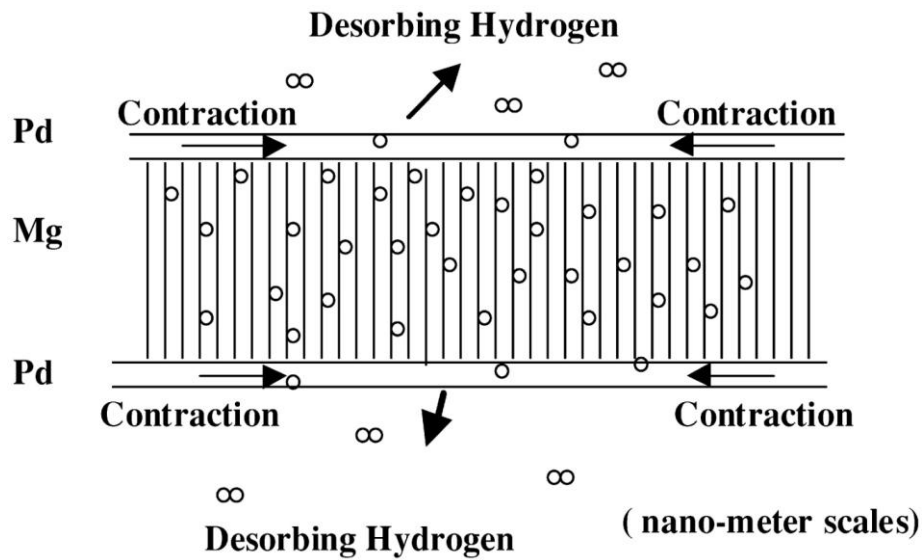


Fig 2.3.7 Schematic diagram of hydrogenated Pd/Mg/Pd film with Mg layer [37]

Compressive stresses can develop during the thin film deposition process. Grain boundary densification has been proposed to induce compressive residual stresses. Besides, during the hydrogen sorption process, the compressive stress accumulates very fast.

Crystallite coalescence occurs which result in tensile stresses forming in the thin films. It is observed in films with some porosity present. Besides, more stable hydride phase destabilized due to the tensile stresses. The surroundings of hydride phase are all the desorbing grains.

As shown in Fig 2.3.8, we consider a piece of thin solid film of the dimensions  $l \times W \times t$ . An applied a force of  $F$  to the area of  $A = Wt$  will stretch the film length  $l$  by  $\Delta l$ . A force equation is

$$\frac{F}{A} = Y \frac{\Delta l}{l} \quad (5)$$

Where  $F/A$  equals to  $\sigma$  (stress) and  $\frac{\Delta l}{l}$  equals to  $\epsilon$  (strain).  $Y$  is Young's modulus. According to the Hooke's law, the equation is

$$\frac{\Delta t}{t} = \frac{\Delta W}{W} = -\nu \frac{\Delta l}{l} \quad (6)$$

Where the letter of  $\nu$  is the Poisson's ratio, it should be noted that the negative sign means that when  $l$  is stretched, both  $W$  and  $t$  will shrink. A possible method to measure Poisson's ratio is to observe the change in lattice parameters by XRD in a direction normal to the tensile stress.

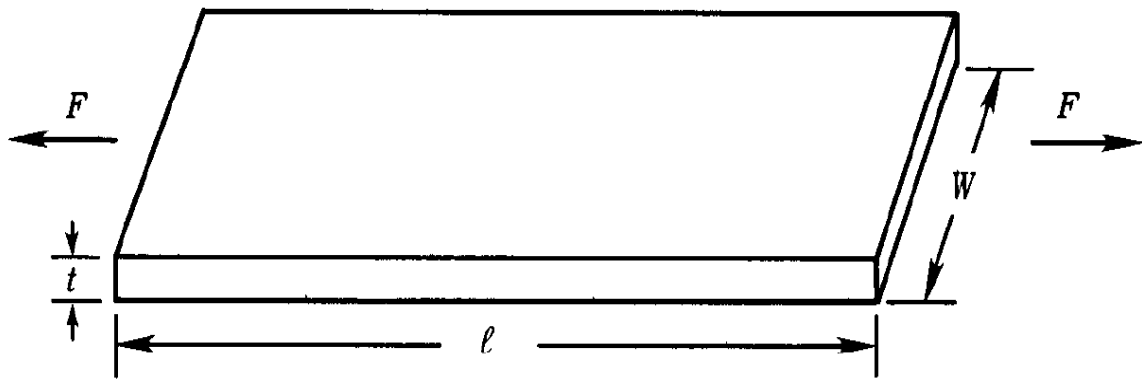


Fig 2.3.8 Direction and applied force by convention. A thin film with dimensions  $l \times W \times t$  under tensile stress [43]

#### 2.3.4 Thermal stress

There are also thermal stresses due to thermal expansion between thin films and the substrate. When carrying out experiments involving heating, it is important to obtain thermal stresses. The effect of heating on stress can be also measured. High temperature leads to thermal stress accumulation. Annealing can be used in order to increase some of these stresses. These thermal stresses are accumulated in the Mg thin films. The stress amplitude depends on the temperature change. The thermal stress can be calculated and estimated using the formula

$$\sigma_f(T) = (\alpha_s - \alpha_f)\Delta TE_f / (1 - \nu_f) \quad (7)$$

In this equation,  $\sigma_f$  is the in plane film stress,  $\alpha_s$  and  $\alpha_f$  are the linear co-efficients of thermal expansion.  $E_f$  is the Young's modulus and  $\nu_f$  is the Poisson ratio of the film.  $\Delta T$  is the change in temperature. This equation indicates that the temperature change has a linear relationship with thermal stress in each substrate.

### 2.3.5 Surface roughness and buckling of thin film

After hydrogen absorption and desorption, the surface becomes rougher than before. More buckling appears on the surface which leads to a change in surface roughness. This buckling can be observed using either a Profilometer technique or Confocal microscopy. The buckling number can be estimated from Profilometry maps which represents the thin film surface condition. Large buckling numbers lead to the rough surface due to the stress accumulation. High buckling number means high surface roughness value. The coalescence and sketches under Profilometry measurement can appear on the thin film surface after hydrogen sorption. The sketches show the stretched grain morphology. These surface sketches can influence the buckling number as well. Buckling numbers increases due to the stress build up during the experimental work.

### 2.3.6 Hydrogen sorption behavior (hysteresis)

Hydrogen sorption refers to the hydrogen absorption and desorption processes. Hysteresis often occurs during hydrogen absorption and desorption cycling of metal hydrides. This can partly be explained by differences in thermodynamic and kinetic properties. Expansion of the metal lattice will occur during the hysteresis process (absorption and desorption). Lattice parameter expands during hydrogen sorption compared of as received materials.

As shown in Fig 2.3.9, metals such as Pd, Ni, Ti, V and Nb can be deposited as a top layer for the fundamental studies. The plateau pressure changes with various miscible metals. This behavior is due to an elastic constraint: when the Mg film transforms to MgH<sub>2</sub> there should be a volume increase, but this is restricted by alloying at the surface. According to the binary phase diagrams, Mg does not alloy with Ti, Nb or V. Capping elements also do not alloy with Mg (Ti, Nb, V). [44] This kind of expansion effect has not been directly observed in powders as the metal lattice can expand unrestricted by being attached to a substrate. However, a synergistic effect is reported with the mixture of Mg<sub>2</sub>NiH<sub>4</sub>/MgH<sub>2</sub> phases, that the hydrogen is released at different temperatures. The tensile or compressive stresses may focus on these phases change of metal to metal hydride phase transitions. The plateau pressure for the formation of MgH<sub>2</sub> increases dramatically due to a clamping effect.

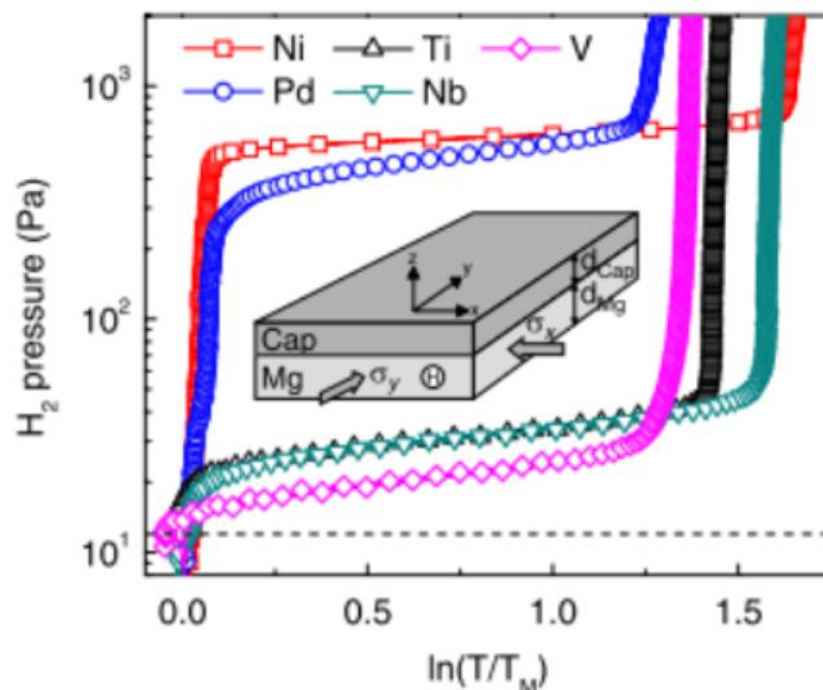


Fig 2.3.9 Effect of miscible or immiscible alloying elements as top layers on the hydrogen plateau pressure of Mg films [45]

Three layered Pd/Mg/Pd thin films have also been investigated (Fig 2.3.10). The PdH<sub>0.6</sub> (111) and PdH<sub>0.6</sub> (200) peaks have the highest intensity in films (a), (b) and (c). These results

suggest that Pd absorbs hydrogen to form PdH<sub>0.6</sub> after hydrogenation at 373 K for 24 h. However, there is no PdH<sub>0.6</sub> X-ray peak in samples (d) and (e); this is due to films (d) and (e) peeling off from the substrate.

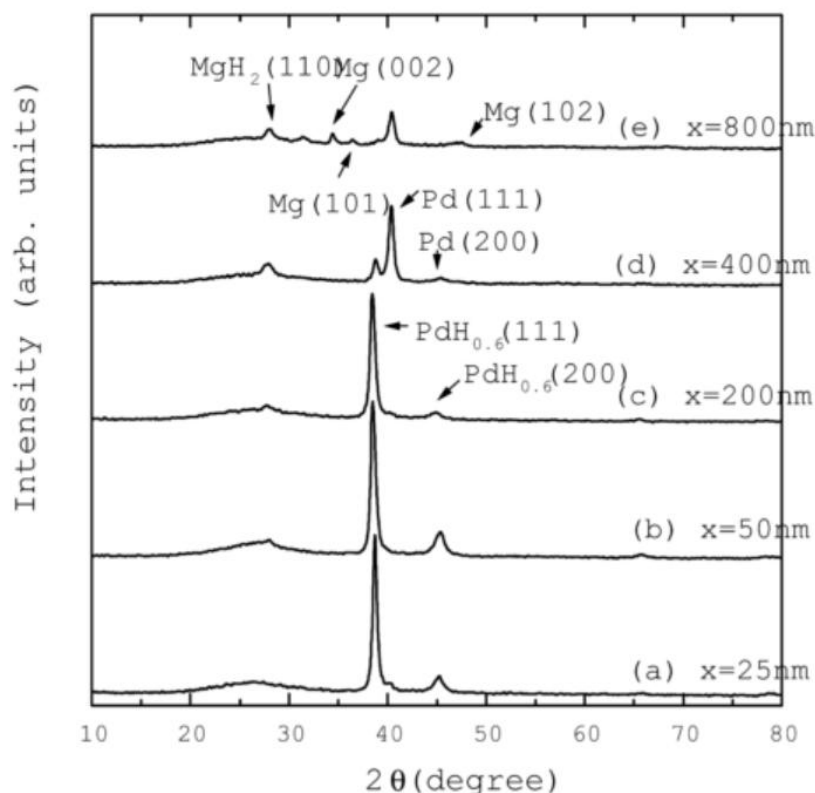


Fig 2.3.10 shows XRD patterns of Pd(50 nm)/Mg(x nm)/Pd(50 nm) films (in which x = 25, 50, 200, 400 and 800 nm) after heating at 373 K for 24 h under 0.1 MPa hydrogen. The broad X-ray peak at  $2\theta$  20-30° is due to the glass substrate. [37]

During the hydrogen desorption process, samples of Pd/Mg/Pd with different Mg layer thicknesses were measured by TDS. As shown in Fig 2.3.11, the hydrogen desorption temperature decreases rapidly as the Mg thickness increases in Pd/Mg/Pd films. Among these samples, Pd/Mg (800nm)/Pd film has the lowest desorption temperature which is around 350 K. The thinner films (Mg thickness 25 nm and Mg thickness 50 nm), have more than two peaks during hydrogen desorption; desorption peaks are around 350 – 400 K. This shows that thicker films (up to 800 nm), exhibit lower hydrogen desorption temperatures (under 0.1 MPa

at 373 K for 24 h). The thickest film (Sample (e); 800 nm) had the highest intensity desorption peak (i.e. highest mass spectrometer ion current), whereas sample (a) exhibited almost no peaks; this is due to the large difference in the mass of Mg in the different samples, and therefore, the mass of hydrogen which can release from the Mg hydrides.

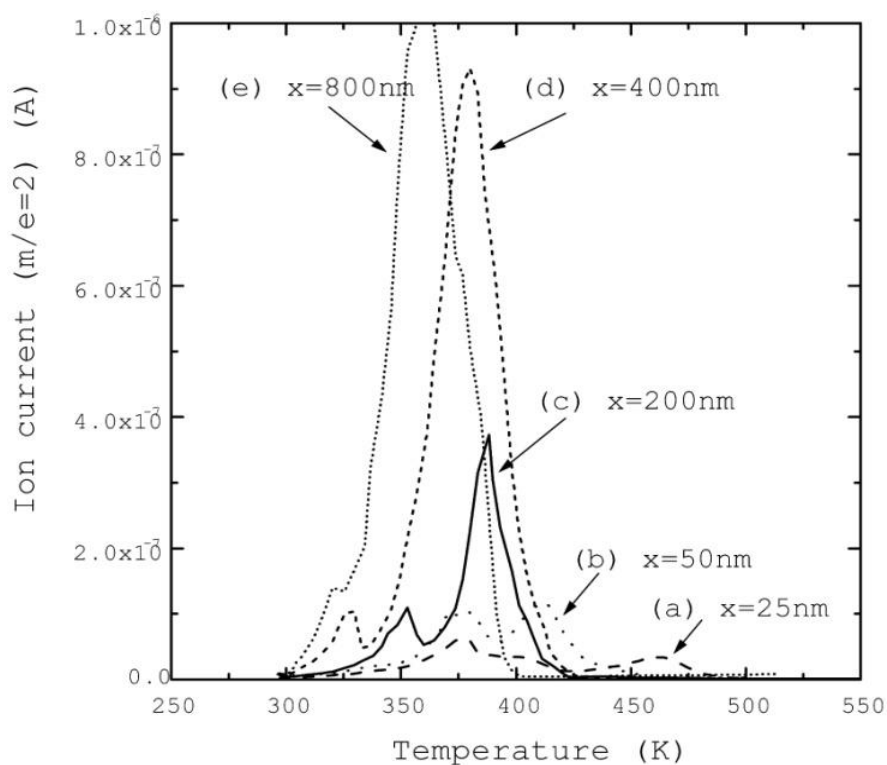


Fig 2.3.11 TDS spectra of several hydrogenated Pd (50 nm) / Mg (x nm) / Pd (50 nm) films where x= 25, 50, 200, 400 and 800 nm. Samples were heated at 4 °C/min under vacuum. [37]

The TDS profiles show that the Pd layers contain around 0.15-0.3 wt% hydrogen. The Mg thin film has hydrogen capacity about 5.0 wt%. Pd/Mg/Pd shows better dehydrogenation properties than the Pd/Mg thin films as the hydrogen desorption temperature is reduced after inserting a Pd layer between Mg and the substrate. Besides, Pd/Mg/Pd has larger grain boundaries than Pd/Mg films which provide more grain pathways. [37]

The sketch shown in Fig 2.3.12 illustrates the effect of thermodynamic bias and extrinsic hysteresis on the H sorption isotherms of a nano-confined system which means that hydride still attached to a substrate. The sketch displays a symmetric hysteresis with respect to the

equilibrium pressure. The colored arrows in (d) have the same meaning as in (b) and (c). If the thermodynamic bias is positive as in (c, d), the absorption plateau is shifted upwards more than that of desorption. Desorption process might even be shifted downwards compared to the bulk materials if hysteresis is very large.

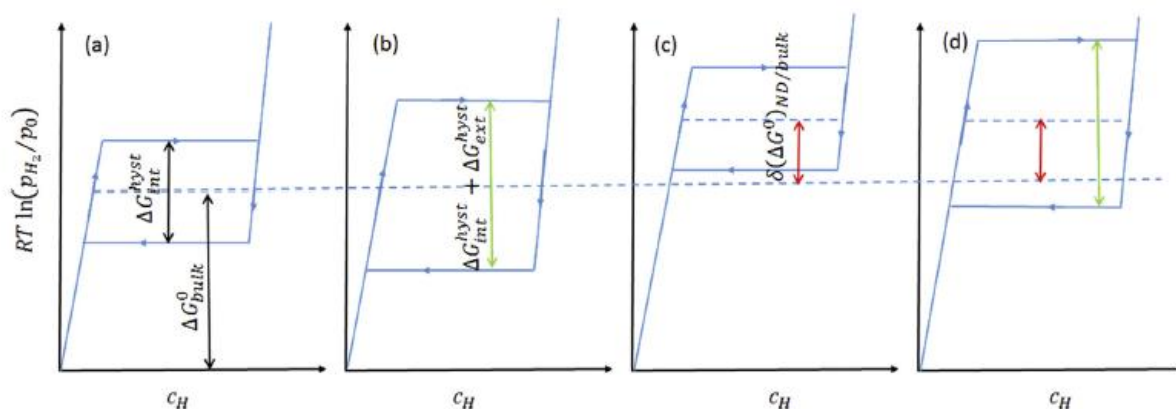


Fig 2.3.12 Hysteresis in interaction with metal hydrides (a) reference bulk materials exhibiting intrinsic hysteresis (b) additional extrinsic hysteresis (c) thermodynamics bias, for instance due to interface or elastic strain in NDs. (d) combination of additional hysteresis and thermodynamics bias [46]

### 2.3.7 Interlayer and various substrate

An interlayer can be inserted between the Mg and Pd layers which can influence the alloying effect. Mg-TM (TM = Ti, Fe, Ni, Co, Cr, V) thin films have all been investigated. Compared with simple Mg-Pd thin films, Mg-TM-Pd can exhibit different optical and electrical properties, e.g. changing between a mirror, (low impedance state) and a transparent (high impedance state) film, during hydrogen absorption. However, some of these transition metals, such as Ti, cannot be alloyed with Mg. A Ti interlayer in a Mg film can significantly improve the hydrogen sorption kinetics and reversibility. [47, 48, 49]

Changing the substrate can also affect the overall hydrogen capacity of thin films. Thinner substrates such as Si can reduce the volume and the weight compared to conventional glass substrate. Thus system volumetric hydrogen storage density is improved. It was observed that it occurs at the Mg-Si interface when the temperature is above 520 K. The formation of bcc-MgPd and  $Mg_2Si$  can be detrimental to the hydrogenation process.

Fig 2.3.13 shows TEM cross sections for different Mg/Pd-based films. The average thicknesses of the Mg and Pd films are 40 nm and 16 nm, respectively. At the interface between the Mg and Pd layer,  $Mg_xPd_y$  can form. It is inter-diffusion between the Mg and Pd layers correlates with the Mg-Pd binary phase diagram, which shows the compounds  $Mg_5Pd_2$  (Region 1 in Fig 2.3.13 (b)) and  $Mg_6Pd$  (Region 2 in Fig 2.3.13(b)). Fig 2.3.13 (c) and (d), show TEM images of a Ti/Mg/Ti/Pd film after exposure to  $H_2$  at 200 °C for 2 h. Ti interlayer can act as an effective barrier inter-diffusion, so avoiding alloying between the Mg and Pd layers. [50]

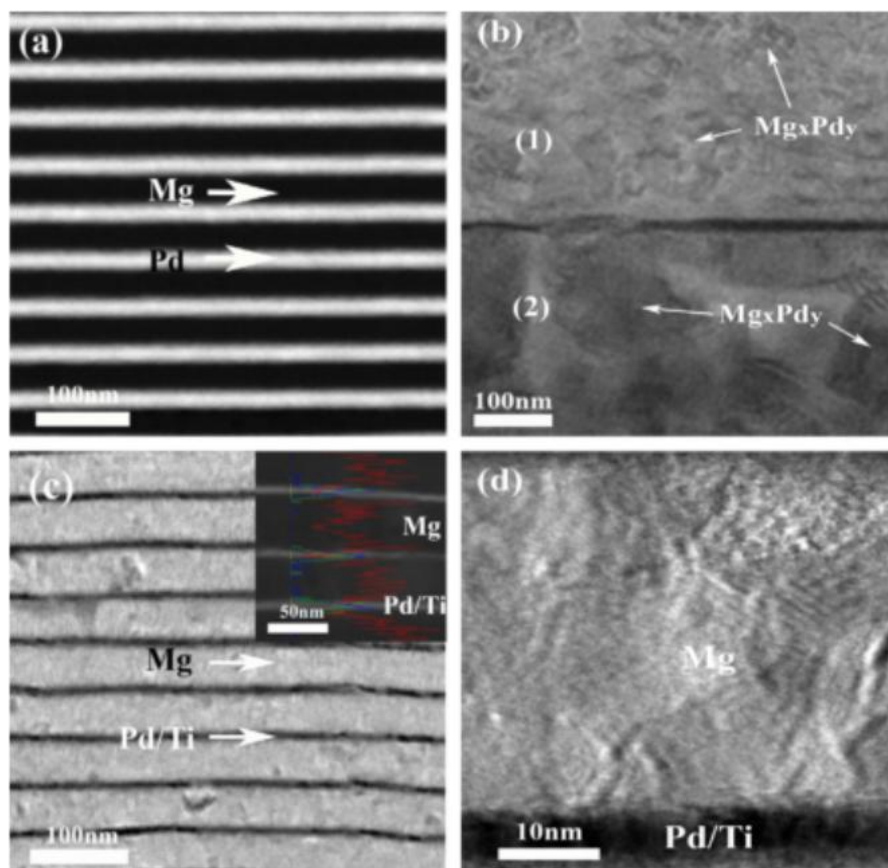


Fig 2.3.13 TEM images of cross sections of (a) an as-sputtered Mg/Pd multilayer film (b) Mg/Pd multilayer film after hydrogenation at 200 °C (c) low resolution (d) high resolution images of a Ti/Mg/Ti/Pd multilayer film after hydrogenation at 200 °C. [50]

Based on the TEM images in Fig 2.3.13, Fig 2.3.14 shows schematic diagrams of Pd/Mg and Pd/Ti/Mg multilayer films, as sputtered and after heating to 200 °C in H<sub>2</sub>. Without a Ti interlayer, Mg and Pd atoms can inter-diffuse at high temperature, to form Mg<sub>x</sub>Pd<sub>y</sub> alloying phase. With a Ti interlayer, Pd, Mg and Ti atoms move in the same direction instead of the random direction.

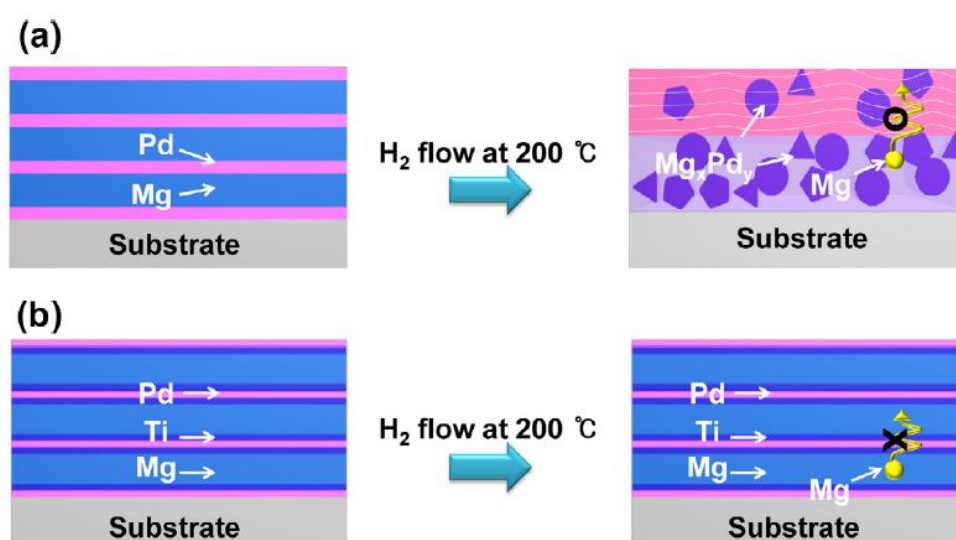


Fig 2.3.14 Schematic diagrams of (a) Mg/Pd multilayered film and (b) Ti/Mg/Ti/Pd multilayer film on a substrate, before and after hydrogenation at 200 °C [50]

Fig 2.3.15 (a), shows XRD pattern for as prepared MgTi<sub>x</sub> (x= 0.11-0.29) film. X-ray peaks for Si and Pd are observed. However, there are no peaks for Mg or Ti, suggesting the formation of amorphous phase(s). The short range order of the MgTi<sub>x</sub> films were examined by TEM selected area electron diffraction, as shown in Fig 2.3.15 (b). Diffraction crystalline rings for Ti, Mg, Pd, are indicated. The diffraction rings of Mg and Pd phase are almost the same. These results indicate that Ti dissolves into Mg but that no Mg-Ti alloy forms in the as-sputtered MgTi<sub>x</sub> films. [51]

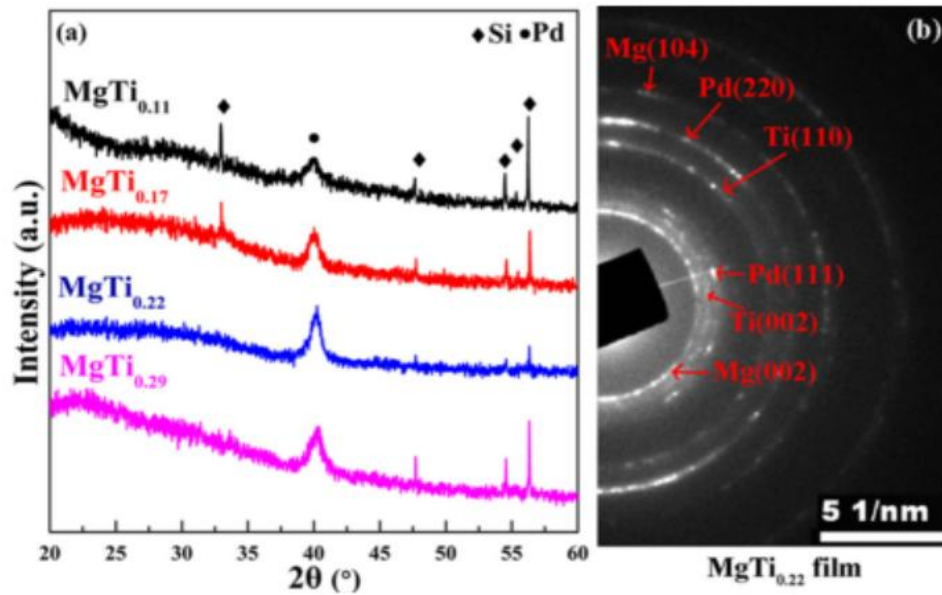


Fig 2.3.15 (a) XRD patterns of as-prepared MgTi<sub>x</sub> (x= 0.11-0.29) films and (b) TEM selected area electron diffraction of MgTi<sub>0.22</sub> thin film. [52]

TEM was used to study [52] the microstructure of Pd-capped Mg films as shown in Fig 2.3.16. A boundary between the Mg and Pd layers is apparent and a columnar structure is visible throughout the Mg film. In this study, the substrate is Si instead of glass. The orientations of the column are different as well which can be shown as random orientations. Substrate change has a clamping effect on thin films, which can lead to a stress build-up during hydrogen absorption and desorption. It is shown that thin films under in-plane compressive stress are susceptible to buckling-driven de-lamination. [53, 54]

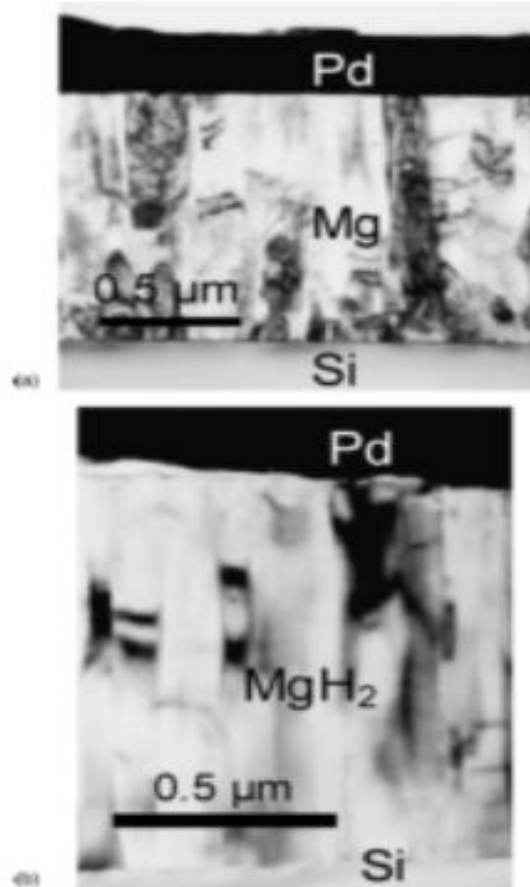


Fig 2.3.16 Cross section TEM images of 100 nm Pd-capped layer with 1000 nm Mg film layer plasma sputtered (in an argon atmosphere at 0.1-0.3 Pa) onto a silicon (001) substrate: (a) as-prepared and (b) hydrogenated Mg films (hydrogenated at 473 K, 0.25 MPa during 2 h) [53]

As shown in Fig 2.3.17 (a), the columnar structure extends throughout the thickness of thin films. A magnesium oxide layer was observed to form between the interface of the Mg and Pd layers. The sample was transferred in air between the PLD system (for Mg) and the sputtering system (for Pd). The oxide layer of Mg acts as a barrier to hydrogen absorption which means that the oxide makes it more difficult to hydrogenate the Mg layer. Higher  $H_2$  pressure and temperature is required for absorption. In addition, a variety of grains with slightly different orientation are present inside the thin films. The columns of laser deposited films are clearly visible in Fig 2.3.17 (a). After hydrogenation at 520 K at 0.25 MPa for 10 hours, the electron microscopy image is shown in Fig 2.3.17 (b). In Fig 2.3.17 (b) the

columns are better visible than columns in Fig 2.3.17 (a). It can be caused by the release of stresses in the film during the transformation. The transformation is from the hcp-Mg structure into tetragonal  $\text{MgH}_2$ , and so a  $\text{MgH}_2$  layer can be seen between the Si substrate and the intermediate layer. The intermediate layer is a mixture of  $\text{MgH}_2$  crystallites and amorphous Mg,  $\text{MgH}_2$  and  $\text{MgO}$  phases. [53]

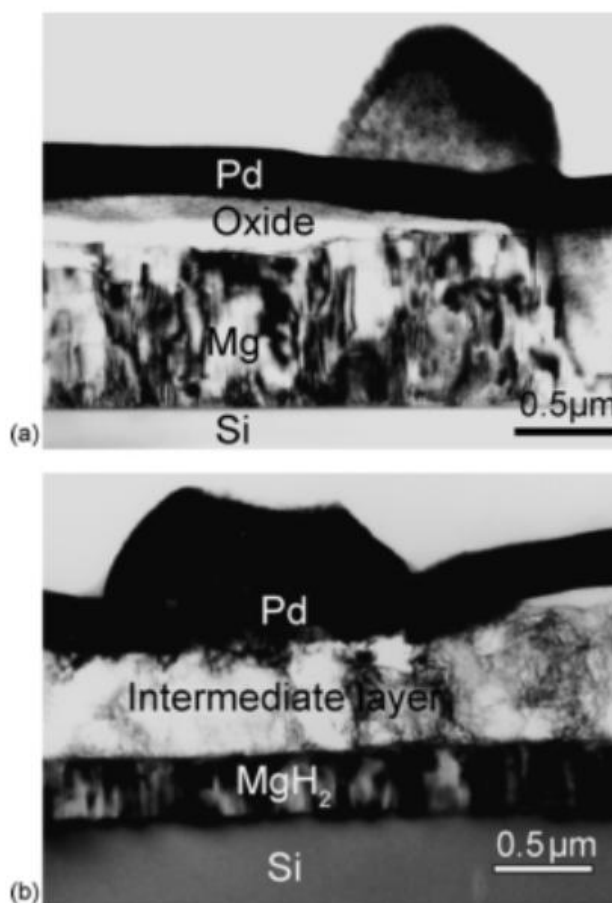


Fig 2.3.17 Cross section TEM micrographs of Mg film pulse laser deposited (in an Ar atmosphere) onto a silicon (001) substrate, with a Pd layer sputtered on top: (a) as-prepared and (b) hydrogenated Mg/Pd films (hydrogen loading was carried out in the pressure of 0.25 – 1 MPa and at temperature ranging from 298 to 673 K for 2-24h). [53]

As shown in Fig 2.3.18, hydrogen loading of as sputtered Pd/Mg films (silicon substrate) were carried out at different temperatures in the range of 298-673 K under 0.25 MPa with hydrogenation for 2 h. For a few of the films, a hydrogen pressure of 1 MPa was used at 24 h

for hydrogen absorption. Pd can act as catalyst which reduces the temperature of hydrogen uptake to 470 K. The maximum capacity was reached at 490 K by heating in 1 MPa hydrogen for 24 h, which indicates the conversion of Mg to MgH<sub>2</sub>. Above 490 K, the maximum uptake is reduced which may correlate with the partial detachment of the Pd cap layer. Higher temperatures (540 K) may lead to the Pd top layer peeling off.

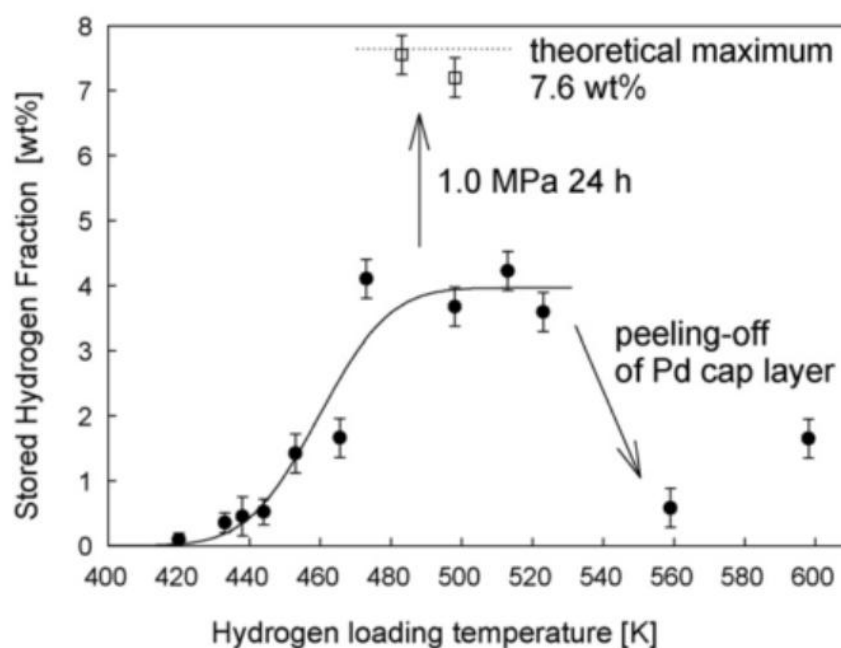


Fig 2.3.18 Hydrogen uptake for as sputtered Mg/Pd films as a function of loading temperature, indicating that maximum capacity of 7.6 wt% is reached at 490 K and 1.0 MPa after 24 h. Heating above 520 K results in a lower hydrogen uptake due to peeling off from the Pd cap layer [54]

In Fig 2.3.19, the cross sectional SEM images indicate a dense structure which consists of columns with an average width of around 50 nm arranged perpendicular to the substrate. The cross sectional SEM images indicate a dense microstructure which is affected by substrate temperature. After changing the substrate temperature from 50 °C to 28 °C, the surface morphology varies from dense columnar type to a slightly porous microstructure made up of

discontinuous grains. In Fig 2.3.19 (a) is dense, (b) and (c) has more porosity. This indicates that the substrate temperature affects the surface mobility of the deposited atoms.

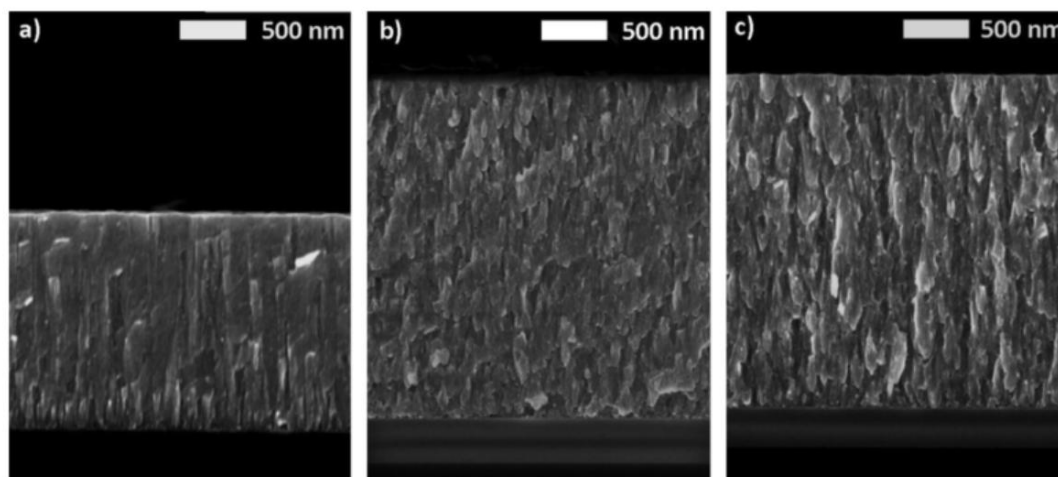


Fig 2.3.19 SEM fracture cross-sectional images for  $\text{MgH}_2$  films deposited using the assisted plasma sputtering technique at different substrate temperature: a)  $T_s = 50\text{ }^\circ\text{C}$ ; b)  $T_s = 37\text{ }^\circ\text{C}$ ; c)  $T_s = 28\text{ }^\circ\text{C}$  with similar total pressure (0.4 Pa) and  $\text{H}_2$  partial pressure (0.2 Pa). Micrograph a) links to a film which was deposited on Si substrate for 80 min whereas films shown in b) and c) were grown on  $\text{SiO}_2 / \text{Si}$  for 105 min and 90 min, respectively. [55]

Fig 2.3.20 (a) indicates a morphology which is similar to the reference film. The deposition rate is  $13.8\text{ nm mn}^{-1}$  in pulsed mode and  $30.1\text{ nm mn}^{-1}$  in continuous mode. Due to the hydrogen concentration, variations are smaller comparing to the high residence time of atomic hydrogen in the plasma chamber. In Fig 2.3.20 (b), sample with  $98\% \pm 4\%$   $\text{MgH}_2$  is shown in the XRD pattern which is calculated on a film deposited by 1ms on and 2ms off. The error for  $\text{MgH}_2\%$  is less than 5%. The (002) and (101) miller planes for Mg are still visible, which indicates that it is difficult to completely hydrogenate magnesium.

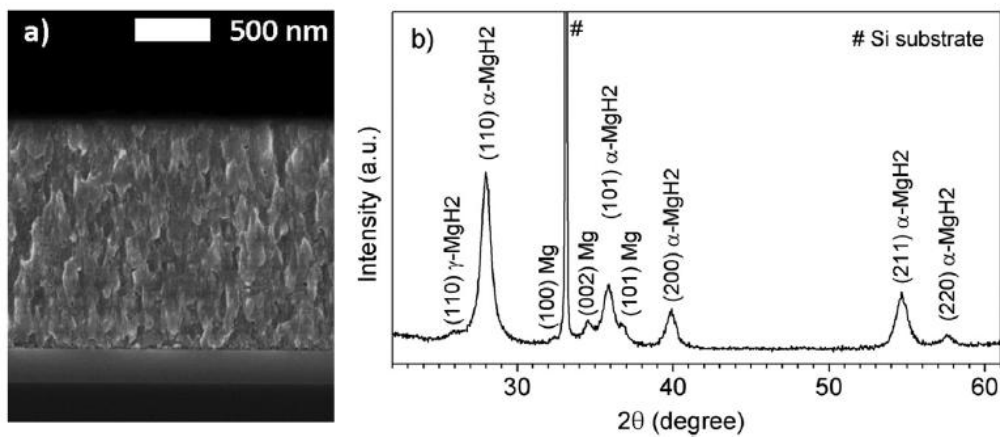


Fig 2.3.20 SEM fracture cross sectional image of Pd-Mg thin film after hydrogenation a) XRD pattern b) of film deposited in pulsed mode, substrate temperature  $T_s = 26 \text{ }^\circ\text{C}$  [55]

Fig 2.3.21 shows an investigation of the substrate effect in Pd thin films. The films with quartz substrates had thermodynamic values very similar to bulk values. The plateau pressure was different to bulk with a high adhesion for thermodynamic modifications. The substrate clamping effect adjusts thermodynamic measurements together with a Pd capping layer. The hydrogen capacity is reduced for Pd on crystal quartz. The substrate has the influence on hydrogen capacity.

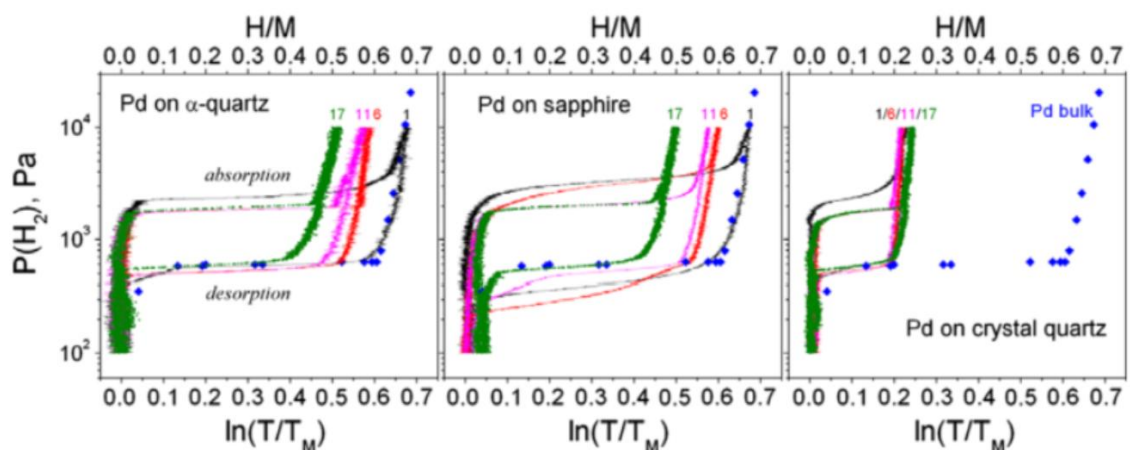


Fig 2.3.21 PCIs of Pd thin films on different substrates for a repeated number of cycles Changes in thermodynamic behavior such as temperature are observed due to stress

relaxation effects in the different substrates. The H/M ratio for the film on crystal quartz would appear to show an incomplete loading – no comment was made by the authors. [56]

Fig 2.3.22 indicates [56] that the difference in film stress measured on films as a function of volume strain, for films that became delaminated from their substrate (green); and those that remained adhered to the substrate (red). The higher level of adhesion promotes additional storage of elastic energy and stress release via plastic deformation.

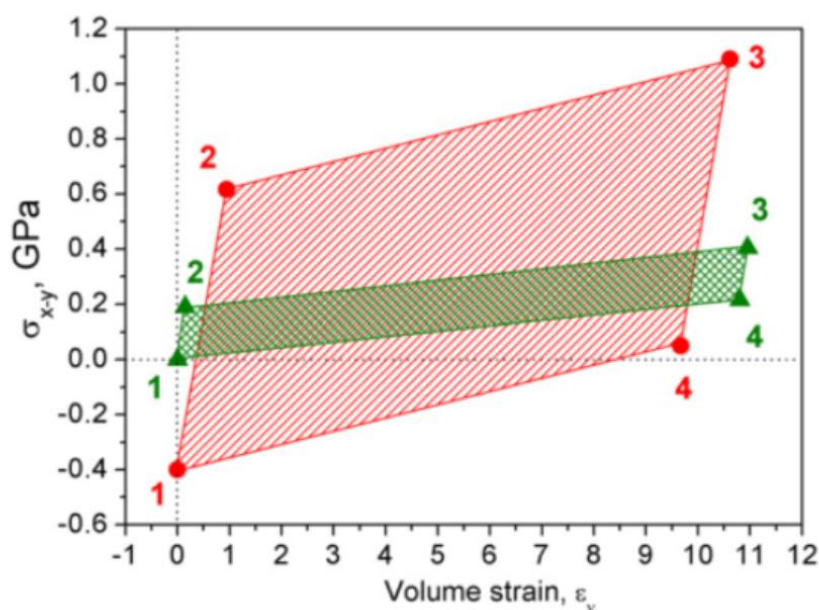


Fig 2.3.22 Stress strain analysis during hydrogen absorption / desorption for palladium films on sapphire substrates with an additional titanium ‘adhesion’ layer (red) and without an adhesion layer (green). [57]

In Fig 2.3.23, the effect of higher temperature decreases hysteresis and the removal of defects is easier at high temperatures. This similar effect is found in  $Mg_2NiH_4$  films. The increase in absorption and decrease in desorption plateau was observed. Both  $\Delta S$  and  $\Delta H$  of hydrogen absorption and desorption can be measured through the Van’t Hoff equation.

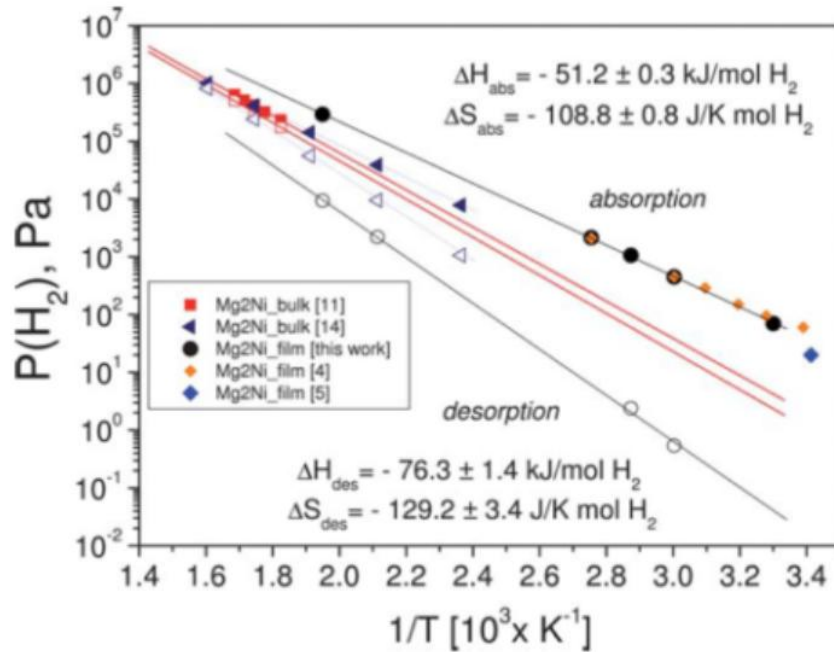


Fig 2.3.23 Van't Hoff plots of the hydrogen absorption and desorption properties of  $\text{Mg}_2\text{NiH}_4$  thin films with glass substrate. A widening of the hysteresis is observed, suggesting a complex mechanism involving the preferential orientation and nucleation of hydride phases in the parent phase, driving a large change in thermodynamic values. [58]

SEM and XRD results indicate [54] that  $\text{Mg}_2\text{Si}$  forms at the interface between the Mg film and the substrate at 300 °C. Mg and  $\text{Mg}_2\text{Si}$  (and Si substrate) can be observed in the XRD pattern. Destabilization induced by  $\text{Mg}_2\text{Si}$  formation occurs with an increase in the equilibrium pressure: the overall reaction is  $\text{MgH}_2 + 1/2 \text{Si} = 1/2\text{Mg}_2\text{Si} + \text{H}_2$ .

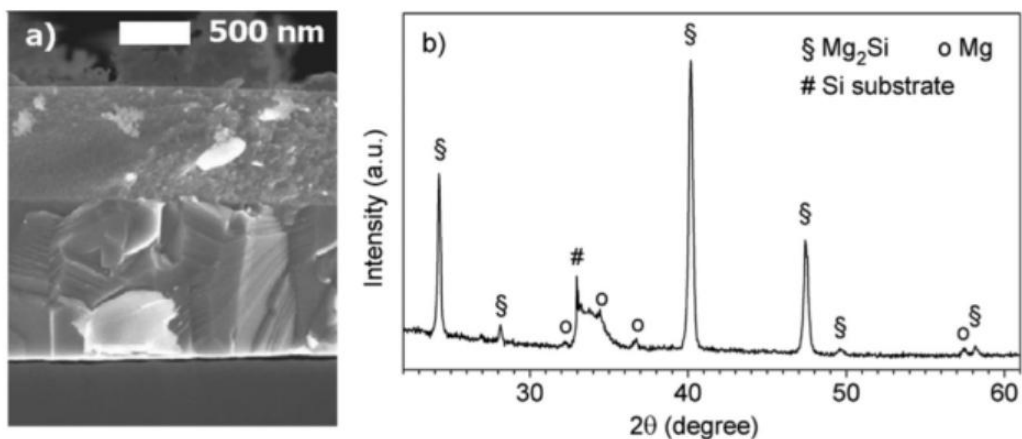


Fig 2.3.24 Illustration of the thin film with the substrate at high temperature during hydrogen desorption measurement. a) Cross sectional SEM image showing the densely crystallized  $\text{Mg}_2\text{Si}$  interface between Si substrate and the film. b) XRD pattern of the thin film [55]

A technique method called ‘hydrogenography’ was developed by Dam and co-workers. [59] This technique is based on the measurement of the transmission of light through thin-film samples exposed to hydrogen, and can be a very useful way of characterizing the affects of differences in hydrogen sorption properties, e.g. in the Mg-Ni-Ti ternary system. The light transmitted through the thin films is measured by a 3CCD camera, which is then used to construct Van’t Hoff plots that illustrate the thermodynamic properties of the hydride films as a function of film composition in Fig 2.3.25 (c). These results have shown the ternary compositional range, for the Mg-Ti-Ni system, which corresponds to an ideal hydride formation enthalpy of -40 kJ/mol.

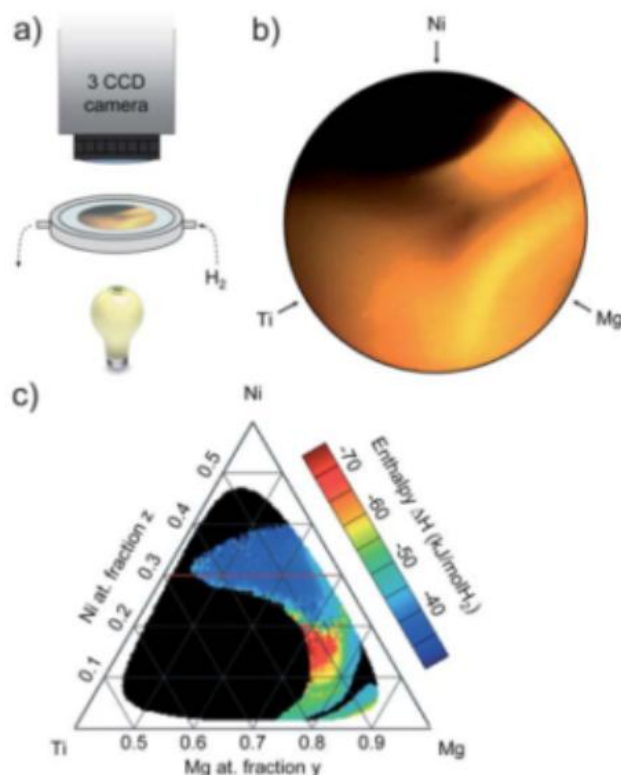


Fig 2.3.25 (a) Optical set up. (b) Optical transmission image of the film specimen of  $\text{Mg}_y\text{Ni}_z\text{Ti}_{1-y-z}$  loaded at 333 K with hydrogen. (c) The enthalpy map of a thin film with ideal thermodynamics identified in the composition region  $\text{Mg}_{69}\text{Ni}_{26}\text{Ti}_5$  with an ideal enthalpy of around 40 kJ/mol  $\text{H}_2$  and a reversible hydrogen content around 3.2 wt% ( $\text{H}/\text{M}=1.1$ ) through electrochemical galvanostatic measurements. [59]

In Fig 2.3.26, it is shown that hydrogen equilibrium pressure is dependent on thin film thickness. Thinner Mg layers have higher equilibrium pressures, among the Pd-Mg-Ti samples. The clamping effect between the Mg and Pd layers occurs by the formation of Pd-Mg alloy layers. [59]

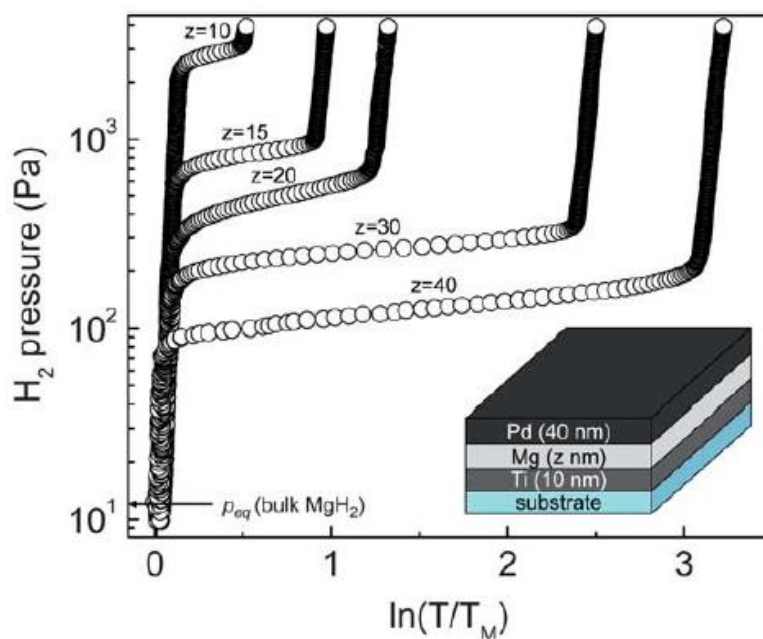


Fig 2.3.26 Ti (10 nm)-Mg (z nm)-Pd (40 nm) thin films with  $z=10, 15, 20, 30$  and  $40$  nm measured by ‘hydrogenography’ at 333 K. The x axis shows the logarithm of the optical transmission  $T$  normalized by transmission in the initial metallic state  $T_M$  which according to the Beer Lambert law is proportional to the hydrogen concentration in the film. [59]

### 2.3.8 Optical transmittance of thin film

Transmittance is the fraction of incident electromagnetic power that is transmitted through a sample. Internal transmittance indicates the energy loss by absorption. The glass tube is first measured as the baseline, followed by the thin film sample transmittance. Based on the baseline, the value of the transmittance is acceptable. During the hydrogen absorption process, the transmittance is always changing because the thickness of Mg layer is different.  $\text{MgH}_2$  forms after hydrogenation which will influence the transmittance properties such as optical reflectivity.

In Fig 2.3.27 (a), 3CCD camera and white light source measure thin films optical behaviors. Transmittance is used to represent the optical properties of the thin film. 3nm Ti interlayer is inserted into the films. In Fig 2.3.27 (b), as the Mg thickness increases from 5 nm to 40 nm, the transmittance decreases from about  $10^{-2}$  to nearly  $10^{-4}$ . While increasing the  $\text{MgH}_2$  thickness only results in a very small increase in the transmittance.

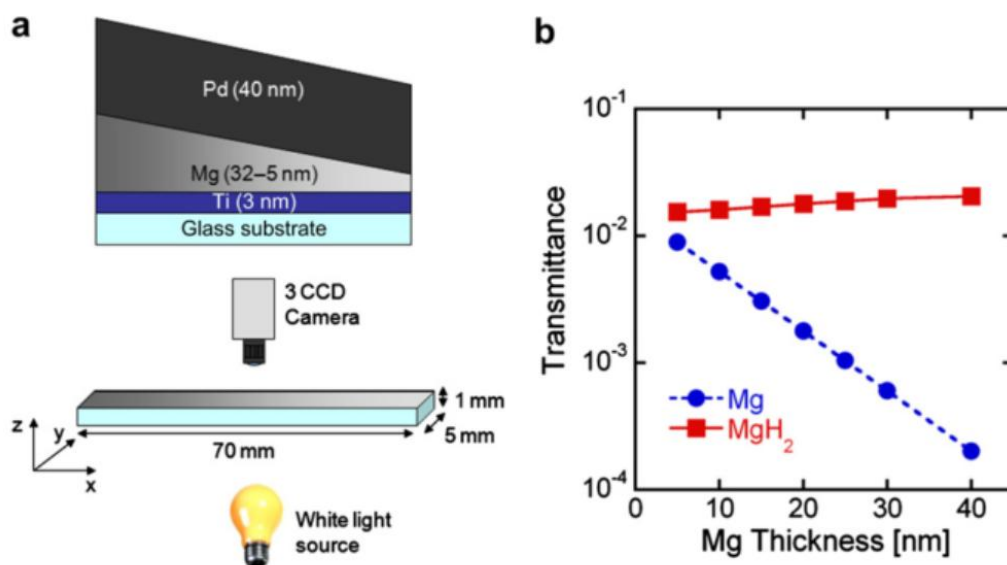


Fig 2.3.27 (a) Sample design: a wedge of Mg with varying thickness along the x direction is grown on a glass substrate  $70 \times 5 \times 1 \text{ mm}^3$ . The Mg wedge is sandwiched between a Ti adhesion layer 3 nm thick and a Pd cap layer 40 nm thick. (b) Simulation generated through

the optical simulation tool SCOUT of the optical transmittance of the sample before (circles) and after (squares) the hydrogenation of the Mg layer at various thicknesses [60]

In order to measure the plateau pressure, the hydrogen partial pressure is gradually increased for each film. The measured PTIs of the sample with various Mg thicknesses are shown in Fig 2.3.28. As the Mg layer gets thinner, the optical contrast given by the plateau width decreases. The optical contrast is lower than value of 2. Due to the elastic thin film model, the hydrogen pressure is sensitive to the Mg thickness.

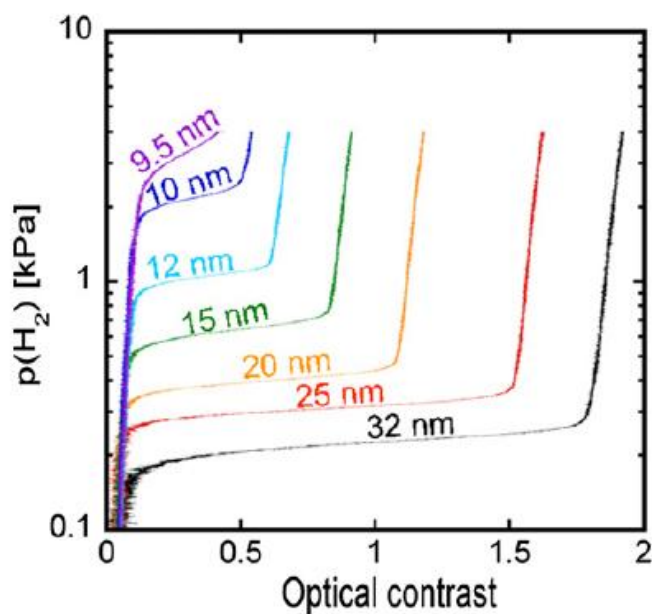


Fig 2.3.28 PTIs measured at 333 K corresponding to different Mg thicknesses: increasing Mg thickness results in an increase of the optical contrast and a decrease of the plateau pressure [60]

In Fig 2.3.29, shows the optical reflectance change at 670 nm for different Mg or Pd thicknesses. After exposure to a 4%  $\text{H}_2$  atmosphere, the reflectance decreases within 5 seconds. The percentage change of the reflectance increases with increasing Mg layer thickness. Samples with thinner Pd layer and Mg layer of sample Pd (4 nm)/Mg (60 nm) exhibit a slower change.

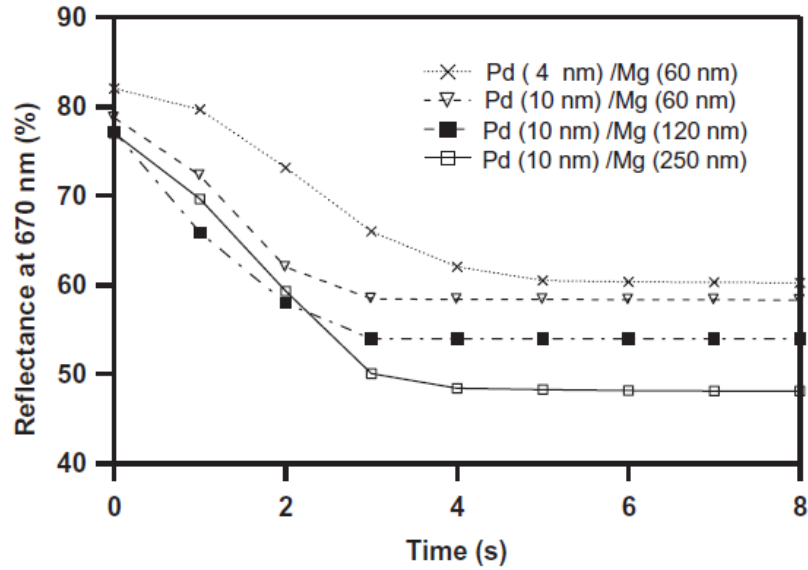


Fig 2.3.29 Time evolution of optical reflectance at 670 nm after 4 % H<sub>2</sub> exposure for Pd capped Mg thin films with different thickness. [61]

Fig 2.3.30 (a) shows the hydrogen sorption properties of thin Mg- M/Pd layers with M= Al, Fe, V, Ti and Zn. The reflectance changes due to the transition of inter-metallic Mg-M to hydride. The reflectance decreases quickly after hydrogenation to 6.4, 7.4, 8.4, 9.0 and 9.3 % for Fe, Zn, V, Ti and Al, respectively. In Fig 2.3.30 (b), the switching amplitude decreases with decreasing the hydrogen concentration from 4 to 0.1 % due to incomplete hydrogenation of these samples. This shows the sensitivity at low hydrogen concentrations is quite low in case of Al, V, Ti and Zn, except the Fe element.

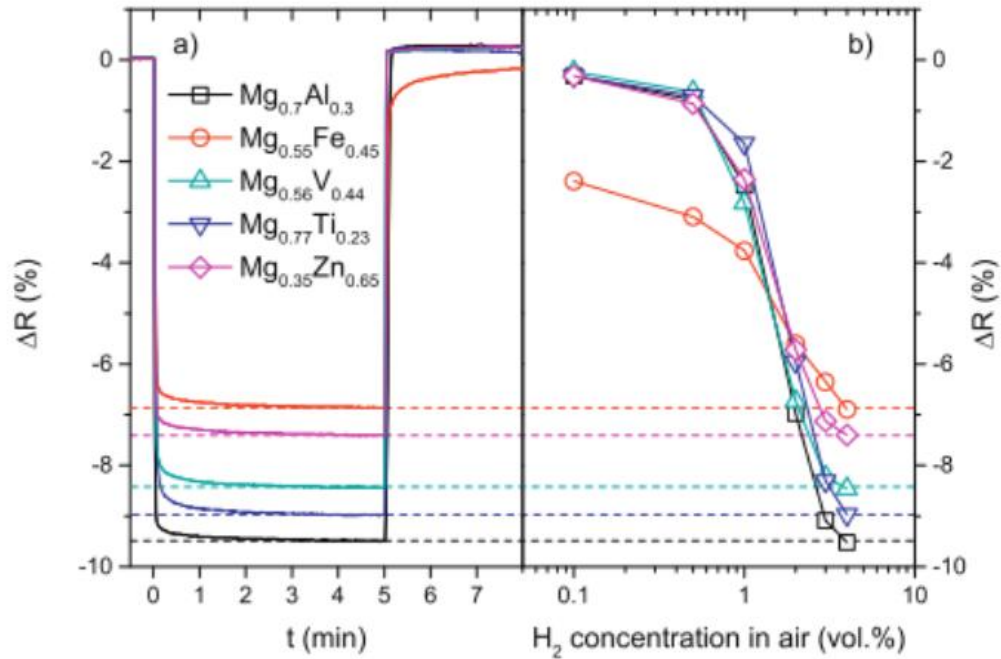


Fig 2.3.30 (a) Reflectance change (at wavelength = 950 nm) of Mg-M/Pd films with M = Al, Fe, V, Ti and Zn during hydrogen loading with 4 vol%  $H_2$  in air. Hydrogen is introduced at  $t=0$  min and flushing with pure air starts at  $t=5$  min. (b) Total reflectance change after saturation is shown for different hydrogen concentrations of 0.1-4% in air. [62]

### 2.3.9 Sheet resistivity of Mg-based thin film

The sheet resistivity can be measured through two probe and four probe techniques. The relative resistivity change indicates the change of hydrogen capacity. The hydrogen sorption kinetics can also be estimated by measuring the rate of resistivity change. After hydrogenation, resistivity increases due to the barrier  $MgH_2$  layer. When inserting Ti interlayer, the resistivity will have a quick response. Therefore, the interlayer can have a large effect on the resistivity change.

In Fig 2.3.31 (a), it is shown that  $Mg_{100}Ti_1$  sample has the most promising hydrogenation kinetics at 298 K. The other samples remained unchanged. Through increasing the

temperature to 353 K, the rate of hydrogen absorption of all the samples was improved. Compared with Mg500-Pd, the other samples' resistivity increased at fast rates. In Fig 2.3.31 (b), the Mg100-Ti1 sample had the fastest hydrogenation rate of all these samples; it can reach hydrogenation saturation in about only 5 hours.

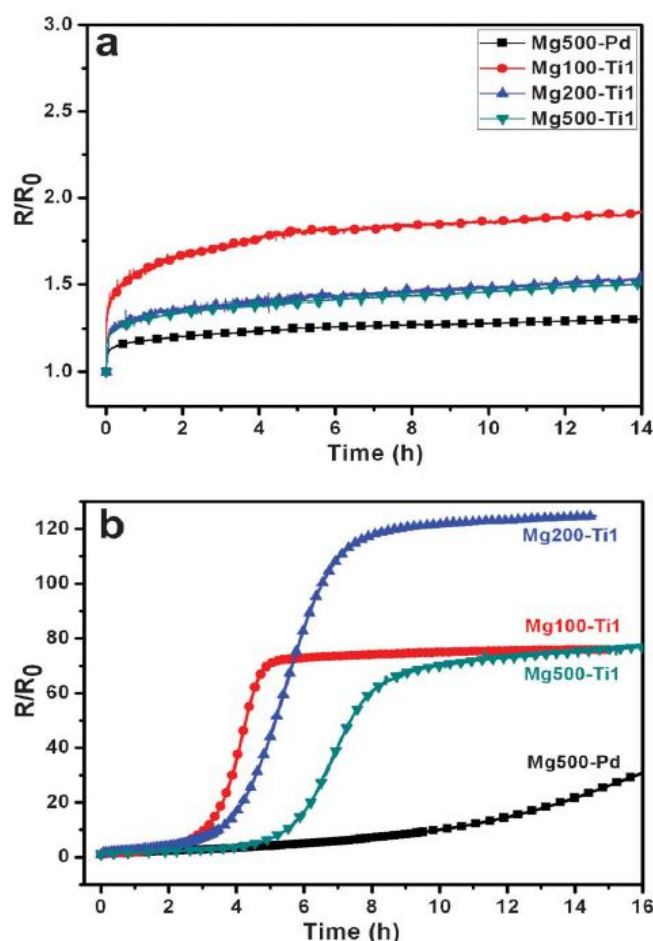


Fig 2.3.31 Relative resistance changes ( $R/R_0$ ) of the 500 nm Mg-Pd films during the hydrogenation in 0.1 MPa  $H_2$  at 298 K (a) and 353 K (b). [63]

In order to further investigate the hydrogen sorption kinetics of the Mg100-Ti sample, the relative resistance changes under hydrogen sorption circles at 353 K were shown in Fig 2.3.32. The results indicate that the Mg100-Ti1 sample has reasonable hydrogenation reversibility. In the second cycle, it exhibits the fastest hydrogen absorption and desorption kinetics: hydrogenation in 3 hours, and dehydrogenation within 1 hour. After the sixth cycle,

the hydrogen capacity is significantly reduced which may be due to the oxidation layer. Desorption time is also reduced at the same time.

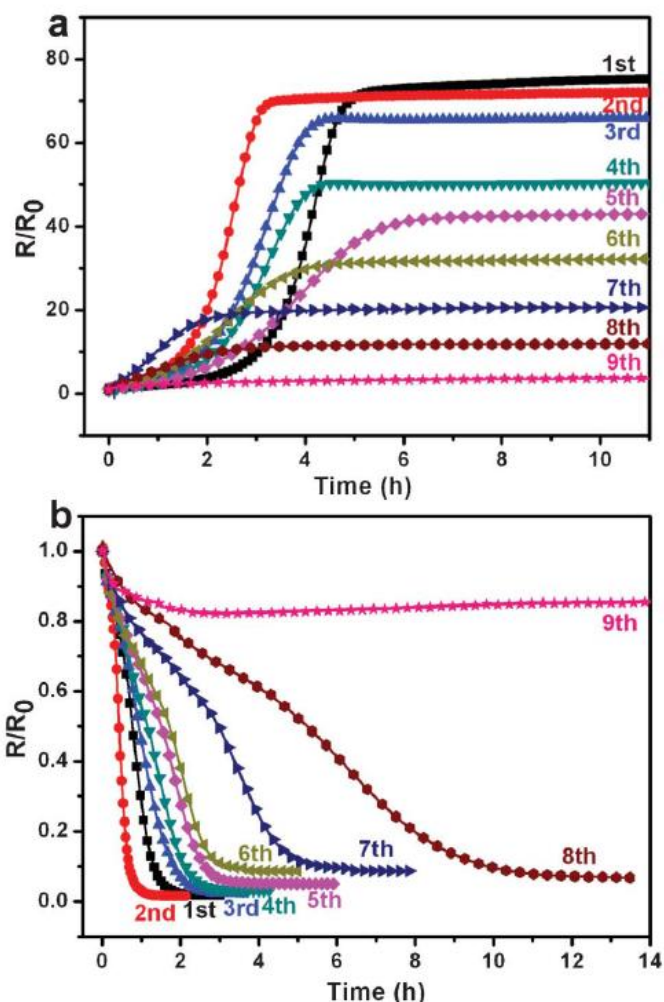


Fig 2.3.32 The relative resistance changes ( $R/R_0$ ) of the Mg100-Ti1 sample during hydrogen sorption cycles: (a) hydrogenation cycles in 0.1 MPa  $H_2$  at 353 K; (b) dehydrogenation cycles in air at 353 K. [63]

At room temperature, the time dependent resistance of sample Pd-Mg-Pd based thin films were investigated.  $R/R_0$  was measured and  $R_0$  was the initial resistance of the metallic film. Among all the samples, Pd-Mg (40 nm)-Pd changed fastest when reaching the saturated plateau  $R/R_0$  in less than 2 minutes. The hydrogenation rate was the highest which was about six times larger than that of Pd-Mg (80 nm)-Pd and eighteen times that of Pd-Mg (100 nm)-Pd. In the initial hydrogenation process, the resistance increased slowly.

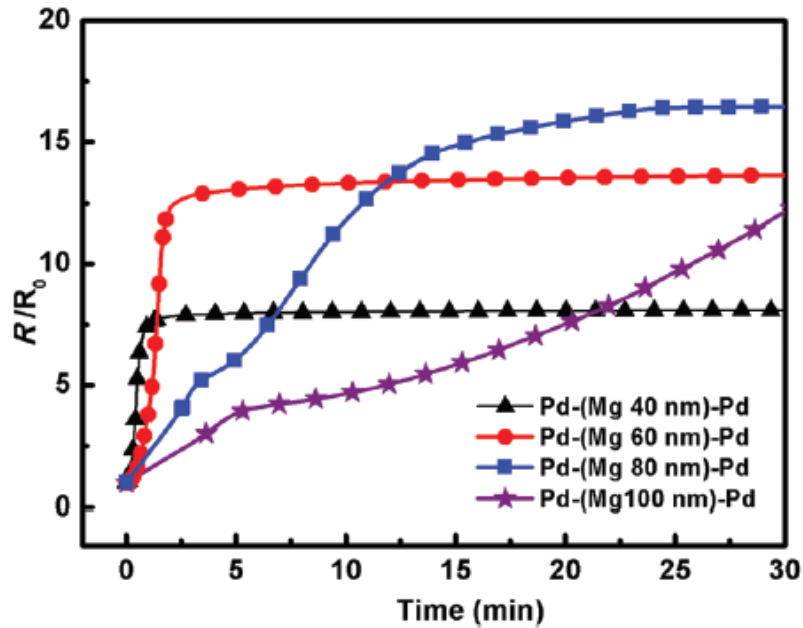


Fig 2.3.33 the relative resistance changes  $R/R_0$ , Pd-Mg-Pd thin films with different thicknesses of Mg layers with respect to absorption time in  $4 \times 10^3$  Pa  $H_2$  at 298 K. [38]

### 2.3.10 Multilayer

A multilayer can be defined as a system of adjacent layers or monolayer by (IUPAC) the international union of pure and applied chemistry. For multilayers, transition metals such as Y, V and Ni are often used to try to increase the hydrogen reaction kinetics and hydrogen capacity. With using Cr and Ti multilayer, the hydrogen capacity was about 4.6 wt% under 10 minutes 250 °C condition. [64] Besides, change the thickness of each inserting layer can also influence the hydrogen sorption properties of multilayer. Different multilayer construction will have a big influence on hydrogen sorption temperature. The principle of the multilayer thin film is investigated.

There is no big effect on thermodynamics changes on the multilayer. The interface is incoherent because of the immiscibility of Mg/Ti. In the Mg/Ti multilayer systems, thermodynamic is changing when the layer thicknesses approach 4 nm. [65] The Ti addition

can be used to decrease the temperature of dehydrogenation which changes the thermodynamics. [66] In the paper, it suggested that interfacial surface free energy change can cause a thermodynamic change. [67]

Mg-Ti multilayer can be made by sputtering. The number of multilayer can be varied in studies. The hydrogen pressure along with various temperatures is shown in Fig 2.3.34. The plateau pressure is demonstrated. After hydrogenation at the same temperature, the 6-layer-stack multilayer sample has higher hydrogen pressure than that of 3-layer-stack Pd-Mg-Ti sample. The multilayer conditions and constructions have a big influence on the plateau pressure and hydrogen sorption temperature.

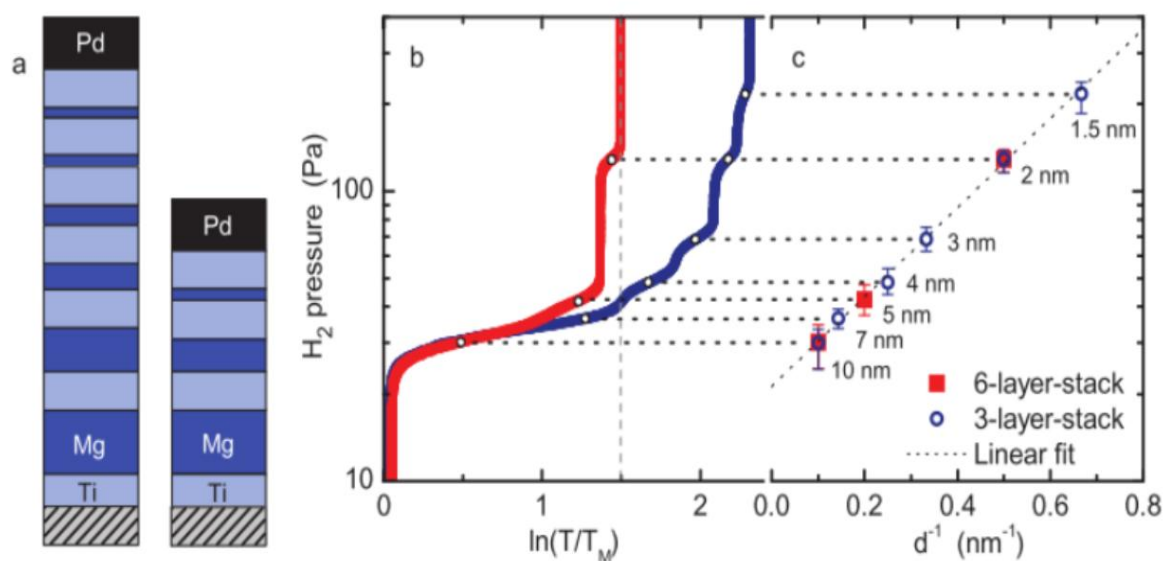


Fig 2.3.34 The demonstration of plateau pressure increase with decreasing layer thickness in Mg-Ti multilayer structures. A new potential method to tailor thermodynamics of MgH<sub>2</sub> [67]

The series of pressure-composition isotherms (PCI) was taken between 250 °C to 350 °C. The samples of Mg/TM multilayer were hydrogenated at 250 °C, 290 °C and 330 °C. In Fig 2.3.35, the plateau pressure is corresponding with hydrogen capacity. In an isotherm, the hydrogen capacity is about  $4.6 \pm 0.1$  wt % H<sub>2</sub> which is lower than 5 wt %. At higher

temperatures, it requires a higher pressure to reach the maximum hydrogen capacity. The hydrogen pressure changes in the hydrogenated circle.

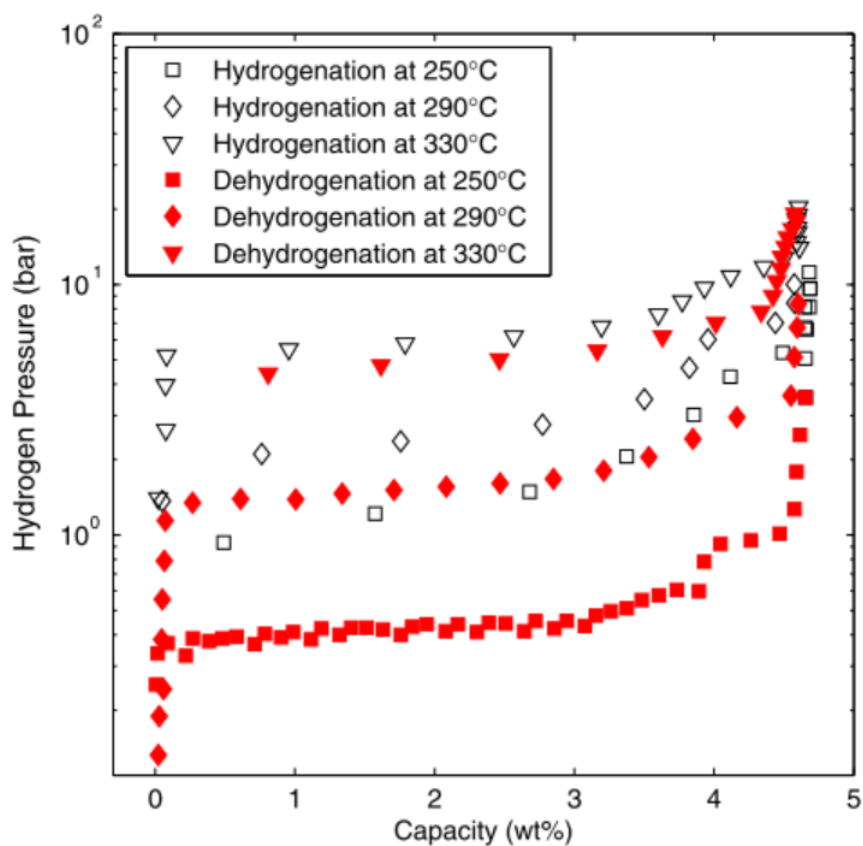


Fig 2.3.35 PCI of the Mg/TM (transition metal) multilayer sample at 250 °C, 290 °C and 330 °C The curve shows the relationship between the hydrogen plateau pressure and hydrogen capacity. [64]

The plateau pressure against the temperature is shown in Fig 2.3.36. From the slope and intercept of two Van't Hoff plots, the reaction enthalpies and entropies were measured. They are the pressure-composition-isotherm. The lower plateau pressure has the dehydrogenation enthalpy of  $\Delta H = 80.5 \pm 2.4 \text{ kJ mol}^{-1} \text{ H}_2$  and the entropy of  $\Delta S = 142 \pm 4 \text{ J K}^{-1} \text{ mol}^{-1} \text{ H}_2$ . Comparing with lower pressure, higher plateau pressure has the  $\Delta H = 66.6 \pm 2.4 \text{ kJ mol}^{-1} \text{ H}_2$  and  $\Delta S = 123 \pm 4 \text{ J K}^{-1} \text{ mol}^{-1} \text{ H}_2$ .

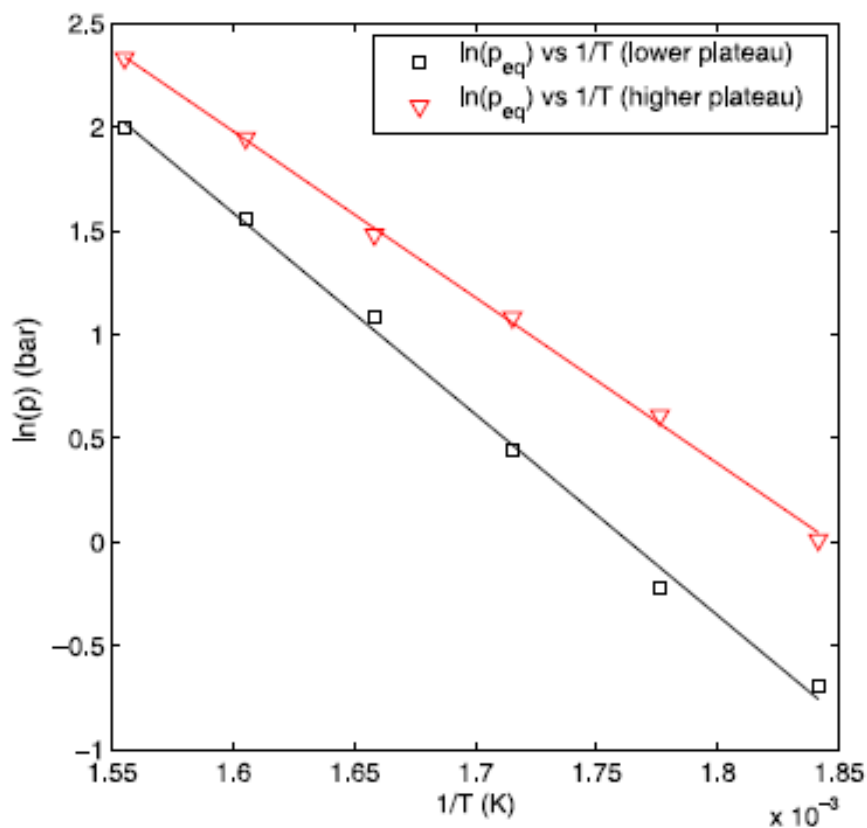


Fig 2.3.36 Van't Hoff plots for the two dehydrogenation plateaus of the Mg/TM multilayer sample. Two curves indicate the relationship between plateau pressure and temperature. They are linear relationship. The straight lines are fitted by the data. [64]

In Fig 2.3.37, a series of DSC measurements made by heating a small amount of hydrogenated thin film at 2 °C min<sup>-1</sup>, 10 °C min<sup>-1</sup> and 20 °C min<sup>-1</sup>. The hydrogen absorption temperature is changing with different heating rate. At 10 °C min<sup>-1</sup>, the absorption temperature is around 275 °C. At 2 °C min<sup>-1</sup> and 20 °C min<sup>-1</sup>, there are two peaks in the DSC curves which mean thermal energy is changing twice during the hydrogenation process. After increasing the heating rate, the hydrogenation temperature can increase.

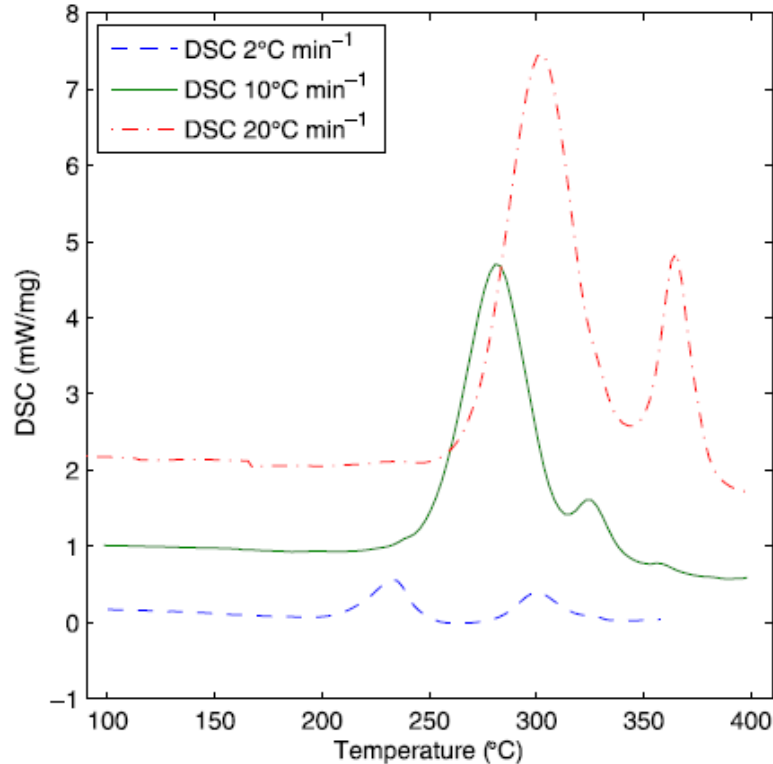


Fig 2.3.37 Differential scanning calorimetry (DSC) measurements of the Mg/TM multilayer samples at 2 °C min<sup>-1</sup>, 10 °C min<sup>-1</sup> and 20 °C min<sup>-1</sup>. [64]

Hydrogenation properties of sample Pd/Ti/Mg/Ti multilayer with different Ti film thickness were measured under 30 bar pressure at 150 °C. Hydrogen capacity of sample Pd (40 nm)/Ti (10 nm)/Mg (360 nm)/Ti (10 nm) was the lowest among all the samples which was around 3.54 wt%. Other samples' hydrogen capacity was above 4 wt%. In the thickness range of 30-50 nm, the hydrogen absorption saturated after 39–56 min. In Fig 2.3.38(b), hydrogen absorption rate increased with increasing Ti thickness. Ti thickness influences the absorption time and absorption capacity. A Ti film of 30-50 nm acts as the catalyst which shows the fastest kinetics among these samples.

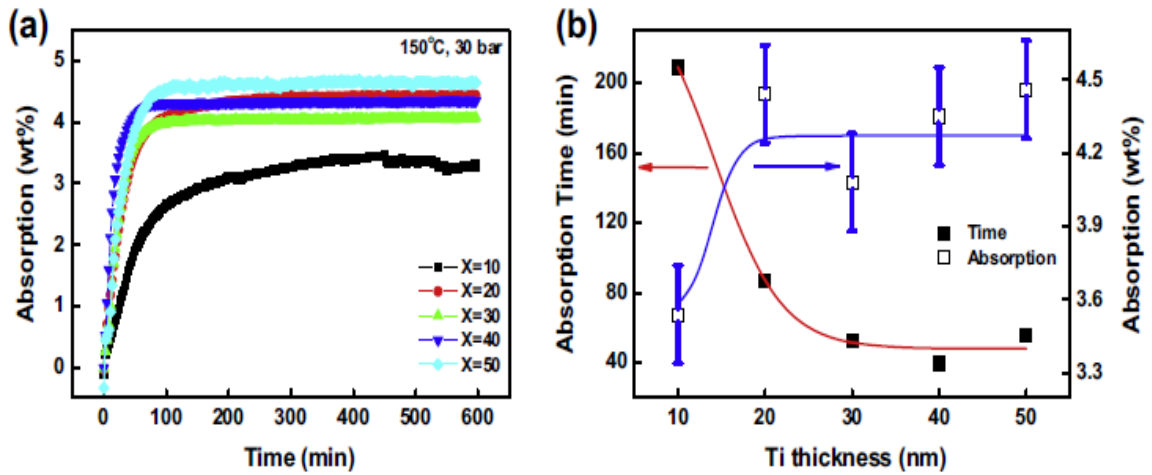


Fig 2.3.38 (a) Hydrogen absorption capacity of Pd(40 nm)/Ti(x nm)/Mg(360 nm)/Ti(x nm) multilayer films with x=10, 20, 30, 40 and 50 and (b) saturation time vs Ti thickness under a hydrogen pressure of 30 bar at 150 °C. [68]

Cross sectional TEM analysis of sample Pd(40 nm)/Ti(10 nm)/Mg(360 nm)/Ti(10 nm) and Pd(40 nm)/Ti(40 nm)/Mg(360 nm)/Ti(40 nm) was shown in Fig 2.3.39. Multilayer films were observed slightly wavy lines due to volume expansion. Mg, Pd and Ti can be seen clearly without intermixing. The EDX data indicated that Ti interlayer make a role as an effective barrier layer in the Pd/Ti/Mg/Ti multilayer films.

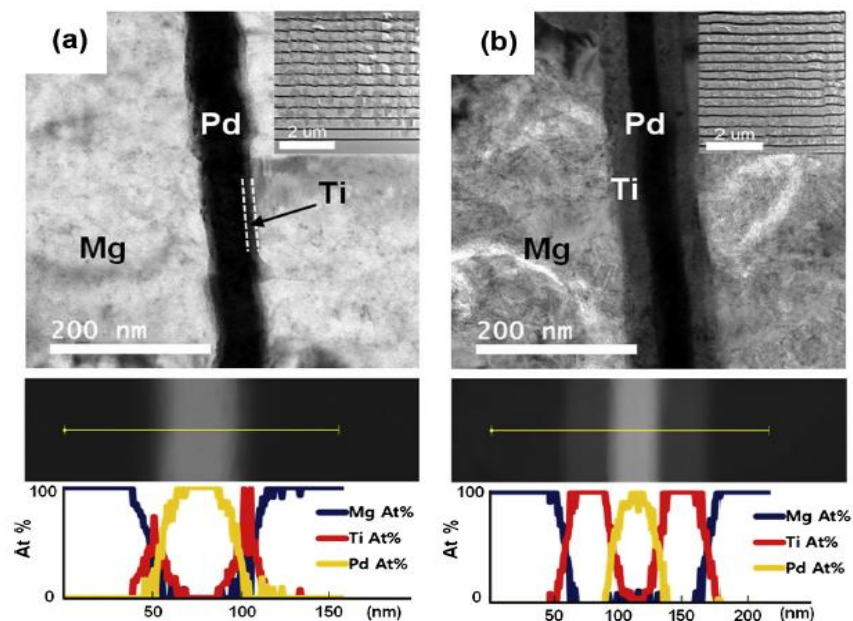


Fig 2.3.39 Cross sectional TEM images of (a) Pd(40 nm)/Ti(10 nm)/Mg(360 nm)/Ti(10 nm) and (b) Pd(40 nm)/Ti(40 nm)/Mg(360 nm)/Ti(40 nm) multilayer films after hydrogenation and dehydrogenation under 30 bar of hydrogen vacuum at 150 °C. [68]

### 2.3.11 Conclusions of thin films

Thin film is a kind of model system which needs more relevant investigations. Many phenomena are interesting and useful, which occurs in a small scale including microstructure and the lattice strain. The investigation needs complementary characterization techniques such as Profilometer, Confocal microscopy, TPD, SEM, TEM and so on. It also seems that there is a lot of evidence which shows that the phase transition can affect the hydrogen absorption and desorption thermodynamics. The microstructure, resistivity and transmittance change can be evaluated during the hydrogen sorption process. The relationship between hydrogen sorption temperature and physical properties can then be compared and discussed. These physical properties may have a significant influence on the hydrogen sorption properties. As an example, sheet resistivity measured as  $R/R_0$  can have a big affect on the temperature. The hydrogen capacity increases when the sheet resistivity changes. Thus  $R/R_0$  value can be used to represent the hydrogenation conditions. Hydrogen sorption properties such as thermodynamics and kinetics can be well considered which is useful for the hydrogen storage and hydrogen sensor applications.

However, there is still a great amount of further understanding needed in the area of  $MgH_2$  formation. There is no depth study of the effect on microstructure and the influence that this may have on the kinetics of hydrogen diffusion into thin films. The influence of three thin film growth mechanisms can be taken into consideration: different growth mechanisms may influence the hydrogenation conditions such as different temperature and pressure. In the end, there are still some questions to be asked and considered. If these questions are answered, it

may lead to a greater understanding of Mg thin film hydrogen sorption mechanisms. Some questions will be investigated in this research thesis, and some questions fall outside the scope and/or timeframe of this work but will be preliminarily discussed in the future work section. The questions are shown below:

Can the substrate, microstructure and hydrogenation conditions be optimized to take advantages of volume expansion? Can the microstructure of the thin films can be modified and controlled to improve the hydrogen sorption behaviors? Can the low hydrogen capacity be used and replaced in hydrogen storage application if considering the weight and the volume of the substrate? Can we find good transition metals in multilayer systems in order to improve the hydrogen sorption properties? Can we alter the mechanical properties such as compressive and tensile stresses in the Mg thin film without considering much of the hydrogen capacity? Can we make a link between interface shear stress value and the different hydrogenation state? Does the hydrogen absorption temperature have a relationship with the hydrogen desorption temperature?

#### 2.4 Thin film deposition systems

The thin film deposition systems are based on physical vapor deposition (PVD). The deposition parameters can be controlled which means that the thin film growth mode can be well tailored to achieve the requiring properties. These changes have a big effect on thickness and adhesion of the thin films. Both the thin film microstructure and surface roughness will be influenced under different deposition parameters. The microstructure is important when considering magnesium thin film applications. Hydrogen sorption properties can be controlled by grain size and column width changes. The atmosphere is under pure Ar without any H<sub>2</sub> gas in order to avoid hydrogenation of the Mg thin film. In this section, we will focus on how the thin film parameters and properties can be tailored by changing deposition

conditions and parameters. How the nucleation will occur which will be discussed in this chapter as well.

#### 2.4.1 Nucleation of free energy consideration

There are three modes for thin film nucleation from the beginning as shown in Fig 2.4.1. In the first mode, it is called Vollmer Weber. In this growth mode, thin film nucleates in the X-Y direction first. Thin films nucleate layer by layer to form a complex structure. The second mode is called Frank-van der Merve mode. The thin films form islands first. Then thin films nucleate island by island which at last has a small region nucleation. For the third growth mode, it is called Stranksi-Kranstanov mode. In this mode, it nucleates quicker than the first two mode. It nucleates island and form layer at the same time. Finally, it will have a big region of nucleation. Both (a) and (c) modes will have better adhesion energy than the energy in mode (b). In mode (b), the adhesion energy is low.

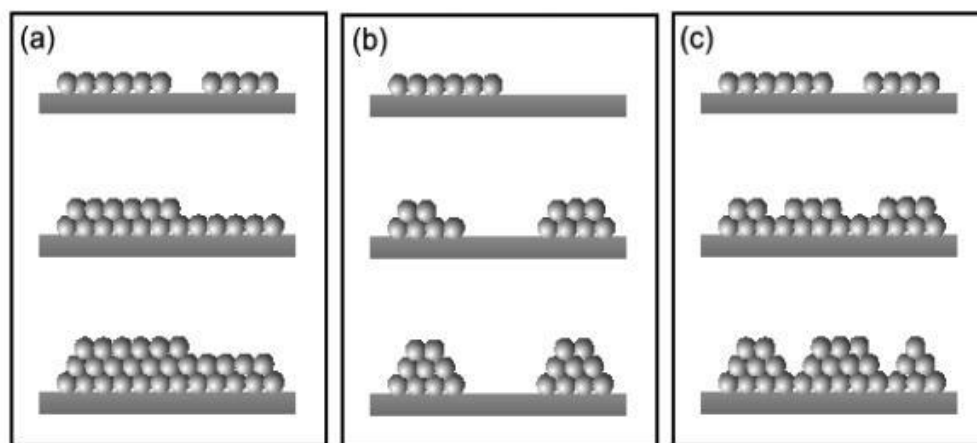


Fig 2.4.1 There are three thin film growth modes: a) Vollmer Weber, b) Frank-van der Merve, c) Stranksi-Kranstanov All the three growth mode is shown in Fig 2.4.1.

For the growth mechanisms, the expressions are shown from Ohring [67]. The equation is shown below. In the equation, the free energy change is  $\Delta F$ . The spherical surface of radius is  $r$ . The sum of the decrease in volume free energy is  $\Delta F_v$  and increase in the surface free

energy is  $\gamma_{AB}$ . The unit of  $\Delta F$  is J. The units of  $\Delta F_V$  and  $\gamma_{AB}$  are  $J/m^3$  and  $J/m^2$ , respectively. The relationship among them is shown in the equation.

$$\Delta F = \frac{4}{3}\pi r^3 \Delta F_V + 4\pi r^2 \gamma_{AB} \quad (8)$$

The above critical radius ( $r^*$ ) with the system is stable. The change in free energy by addition more atoms becomes zero. Thus the equation is shown below:

$$\frac{d(\Delta F)}{dr} = \frac{d\left(\frac{4\pi r^3 \Delta F_V + 12\pi r^2 \gamma_{AB}}{3}\right)}{dr} = 0 \quad (9)$$

$$\text{Thus the result is } \gamma_{AB} = \frac{-\Delta F_V r^*}{2}$$

$$r^* = \frac{2\gamma_{AB}}{\Delta F_V} \quad (10)$$

After calculation, the critical radius is  $\frac{2\gamma_{AB}}{\Delta F_V}$ .

Take  $r^*$  into (1) to provide the critical free energy  $\Delta F^*$  for a particle critical radius:

$$\Delta F^* = \frac{16\pi\gamma_{AB}^3}{3(\Delta F_V)^2} \quad (11)$$

At last, the final equation shows the energy barrier for nucleation of a homogenous and spherical particle. The free energy changes with the change of critical radius. The free energy has a linear relationship with the particle critical radius. [69]

#### 2.4.2 Determining $\theta$

The energy barrier for nucleation is as a function of the surface energy of the Mg-based thin films. As for heterogeneous nucleation, the energy barrier can be shown as a function of  $\theta$ . It is important to quantify  $\theta$  to understand different thin film growth modes. Different growth modes have the different  $\theta$  value.

The adhesion energy can be estimated and calculated as shown below:

$$E_{adh} = \gamma_A + \gamma_B - \gamma_{AB} \quad (12)$$

The  $E_{adh}$  is the adhesive energy.  $\gamma_A$  is the surface energy of material A,  $\gamma_B$  is the surface energy of material B and  $\gamma_{AB}$  is the interface energy between A and B. Suggesting that A is liquid and B is solid, we can describe the angle through the liquid solid interface as shown in the Fig 2.4.2.

$$\cos\theta = \frac{\gamma_A \gamma_{AB}}{\gamma_B} \quad (13)$$

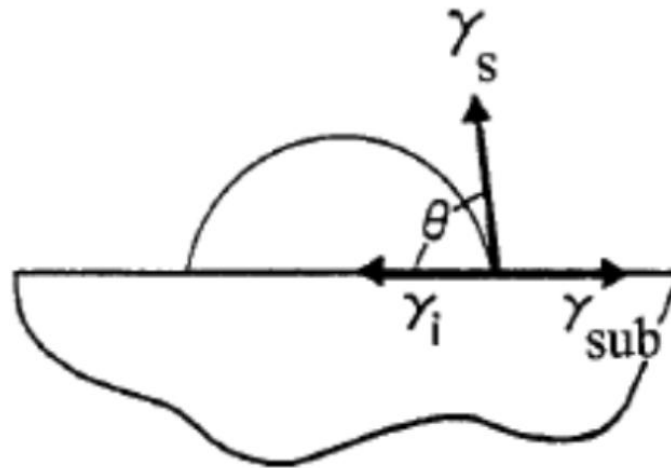


Fig 2.4.2 a schematic diagram of a water droplet on a substrate (Adapt from the author Thompson [70])

### 2.4.3 Temperature effect

The rate equation of heterogeneous nucleation is shown below:

$$N = N^*A*\omega \text{ (Nuclei/ cm}^2\text{sec)} \quad (14)$$

$N^*$  is given by this equation:

$$N^* = n_s \exp\left(\frac{-\Delta G^*}{K_B T}\right) \quad (15)$$

In these equations,  $N^*$  is the equilibrium number of nuclei,  $\omega$  is the rate of atom impingement onto the nuclei of critical area  $A^*$  and  $K_B$  is the Boltzmann constant.  $n_s$  is the density of nucleation sites. In addition, the temperature can be a big factor governing the grain size. During sputtering, it is difficult to control the substrate temperature. The substrate temperature will increase after atoms knock. The barrier for nucleation is controlled by surface energy in the Mg thin film systems. Surface energy has a big effect on the nucleation process.

## 2.5 Hydrogen storage applications and hydrogen sensors

Hydrogen storage and hydrogen sensors are two different applications that have various targets, which depend on the type of the application. Thin films can store hydrogen and release hydrogen under different temperatures and pressures. However, the hydrogen capacity of these thin films is low because of the substrate's volume and weight. Thus, reducing the thickness of the substrate is required in order to improve the storage capacity. For the hydrogen sensors, the parameters such as hydrogen response time, optical properties and sheet resistivity can be used to characterize the thin film samples. It is a promising application for Mg based thin films. Among Mg-Ni and Mg-Ti based alloys, using a 50 nm thick  $Mg_{70}Ti_{30}$  film capped with a 30 nm Pd catalytic layer acts as the sensing layer. The optical fiber sensor can be shown in Fig 2.5.1. There is a protective top layer for coating. It can be used to prevent degradation of film by condensed water. Beneath the optional coating is a palladium layer which act as catalyst for hydrogen absorption. Beneath the Pd layer, there is the switchable mirror which is not completely transparent. An example of a hydrogen detector is shown in Fig 2.5.1. The fiber optic hydrogen detector includes many parts such as protective coating, switchable mirror, multimode fiber and fiber jacket. [72] As for the

hydrogen sensors, the optical switch mirror properties are useful. Pd capped Mg-Al, Mg-Fe, Mg-Ti and Mg-V thin films have been used. During the hydrogen sorption process, there is a switching from a shiny metallic state to a transparent appearance. The sensitivity of the hydrogen gas is 0.1 vol% in air. Among all the samples, Mg-Fe exhibits the best optical properties which make it interesting for hydrogen sensor applications. The three layer system of Mg/Pd-Fe provides high durability. The hydrogen sorption kinetics is quick. The entire dehydrogenation process can take less than 1 min which is useful for hydrogen sensors' applications. [71]

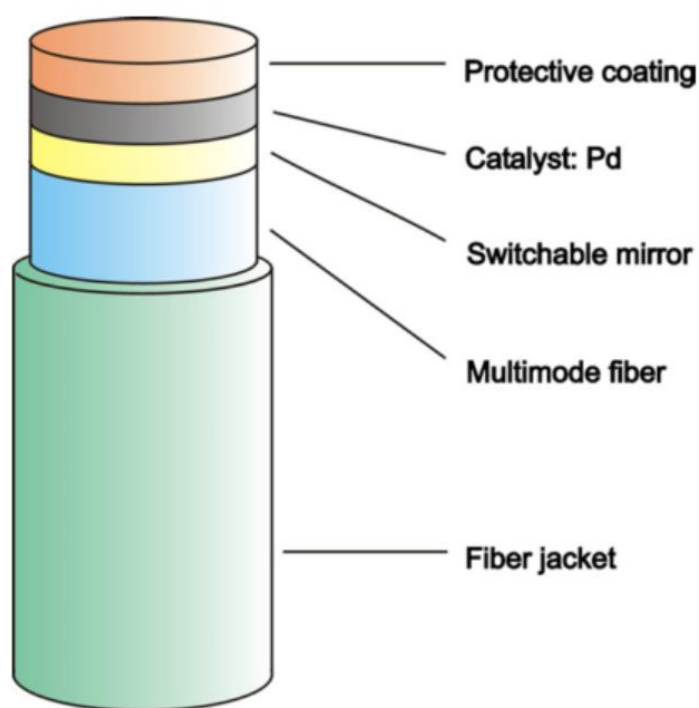


Fig 2.5.1 Layout of the fiber optic hydrogen detector [71]

The Fig 2.5.2 indicates the photographs in transmitted light for a hydrogenated 200 nm Mg film with 10 nm coating Pd. After hydrogenation, the film is in an optically transparent state, as shown in Fig 2.5.2a. When temperature increasing, the nontransparent scratch like parts form as shown in Fig 2.5.2b and Fig 2.5.2c. More scratches are observed in the Fig 2.5.2c. It indicates that nontransparent precipitates are linked with the dehydrogenated Mg. Among these samples, the optical features correspond to the Mg based thin films. In future, this

feature can be used as hydrogen sensors based on the change of optical behaviors after the hydrogenation process.

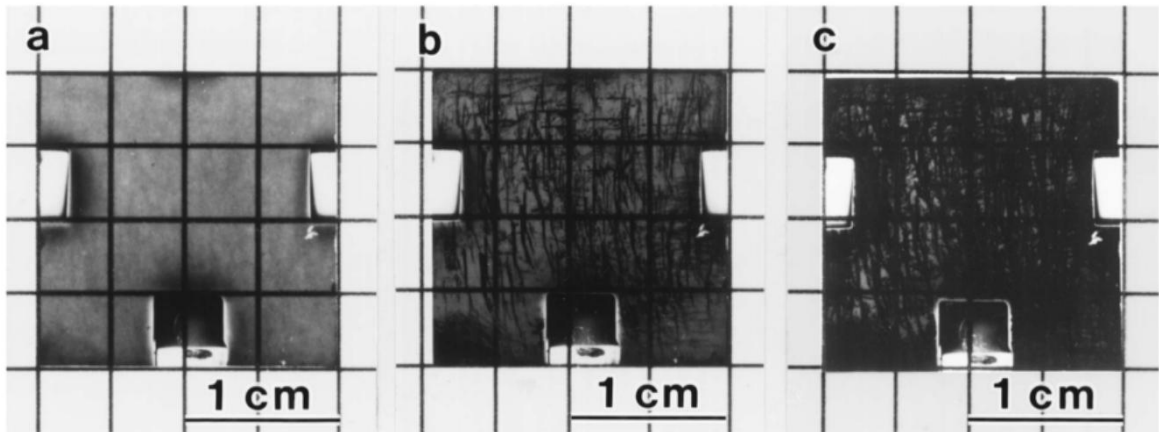


Fig 2.5.2 The photographs in transmitted light for hydrogenated 200 nm Mg thin film coating with 10 nm Pd, (a) after hydrogenation at 373 K under a hydrogen pressure of 0.1 MPa for 24 h in an in situ system, and after heating at (b) 393 K and (c) 453 K for 300 s in air [73]

In Fig 2.5.3, it indicates that the transmission spectra as a function of wavelength for a hydrogenated 200 nm Mg thin film coating with 10 nm Pd. The reflection and absorption can limit the maximum transmission. After correction for quartz glass substrate, the transmission of hydrogenated film can meet around 25% in the range of 400-1000 nm. After correction for the quartz glass substrate with 10 nm Pd thin film, the transmission reaches 82% maximum at around 900 nm.

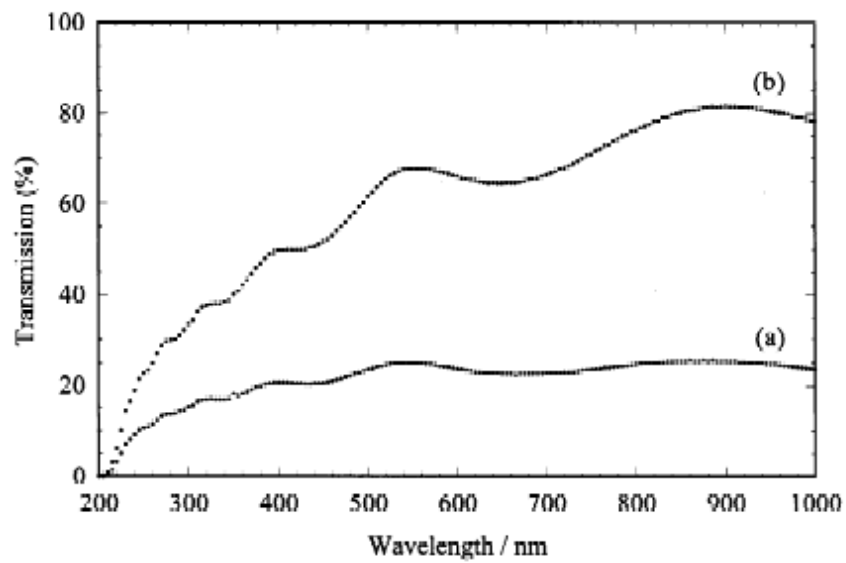


Fig 2.5.3 Transmission spectra in the function of wavelength for hydrogenated 200 nm Mg thin films coating with 10 nm Pd (a) after correction for the quartz glass substrate and (b) after correction for the quartz glass substrate with 10 nm Pd thin film The spectra were measured in air at room temperature [73]

### 3. Aims and Objectives

The literature review shows the importance of Mg based thin film's study. In these aspects, Mg-based thin film has many useful prospects such as hydrogen storage application and hydrogen sensors. However there are some key concepts in the area of thin film research haven't studied in much depth. It is shown that thin film behaves quite differently with powders in stress and microstructure. The aims of this research are to build a complete picture for properties of Mg-based thin films. The main point is focus on Mg thin hydrogen sorption properties especially thermodynamics and kinetics for hydrogen storage. And build the relationship between hydrogen sorption properties and thin films' physical properties for hydrogen sensors. The physical properties considered are stress, surface roughness, sheet resistivity and transmittance.

The specific research objectives for hydrogen storage and hydrogen sensors investigations are as follows:

- To investigate the effect of different sputtering conditions (sputtering current and base pressure) on thin films' microstructure, lattice parameter and Mg grain size. Estimate the grain size based on microstructure.
- To find the new phases formation based on ex-situ XRD and in-situ XRD measurements under different atmosphere (under H<sub>2</sub> / He) in order to know the reaction mechanisms of Mg based thin films.
- To investigate the various Mg thicknesses, interlayer (eg. Ti interlayer) and substrate (eg. Si substrate) influence on hydrogen sorption temperature and kinetics based on in-situ XRD results. Think the useful method to improve Mg based thin films' hydrogen storage behavior for hydrogen storage. Find better method to store hydrogen with low sorption temperature, quick sorption kinetics and high hydrogen capacity.

- To combine the surface roughness and buckling appearance of Mg-based thin films under different hydrogenated and vacuum conditions (Temperature, Pressure). Make the link between hydrogen sorption behavior and thin films' physical properties such as surface roughness.
- To investigate the intrinsic stress and the interface shear stress of Mg-based thin film under various hydrogenation conditions. Make the link between interface shear stress and hydrogenation process.
- To investigate the phase change after hydrogenation multilayer samples with the transition metal Y. Think about other transition metals such V and different construction effects on hydrogen sorption behavior. Find a potential route to store hydrogen.
- To measure the sheet resistivity of Mg-based thin film change during hydrogen sorption process using both two probe and four probe techniques. Using sheet resistivity change is to compare the kinetics and hydrogen capacity properties.

## 4. Experimental Techniques

In this section, equipment technique will be introduced. Firstly, the samples are deposited on the glass substrate. Sputtering machine (CFUBMSIP) is used. Secondly, Confocal microscopy and SEM are used for characterization for the microstructure. Ex-situ XRD and in-situ XRD can detect sample at room temperature and various temperature  $H_2$  or He atmosphere. Then, the samples can be hydrogenated on different conditions by using hydrogen chamber. And finally, dehydrogenate samples using RGA techniques. Both hydrogenation and dehydrogenation can be measured. Raman spectroscopy and optical UV laser can be measured and used. These methods are useful for characterization and discussion of Mg-based thin films.

### 4.1 Sputtering machine (CFUBMSIP)

There are three main ways to deposit the thin films such as physical vapor deposition, chemical deposition and electrochemical deposition. In my research, physical vapor deposition is used to deposit thin film onto the substrate. (eg. Glass substrate) PVD are cheaper and more versatile comparison to other systems. For the principle of PVD can be shown below. Argon atoms bombard the Mg target at first. The ions interact with the target and knock out an atom of target material. The deposited atoms will form as a layer on the metal layer. There is no chemical reaction happened in this process. The reaction is physical dependent. Deposited speed is controlled by sputtering parameters such as sputtering current and Ar flow rate.

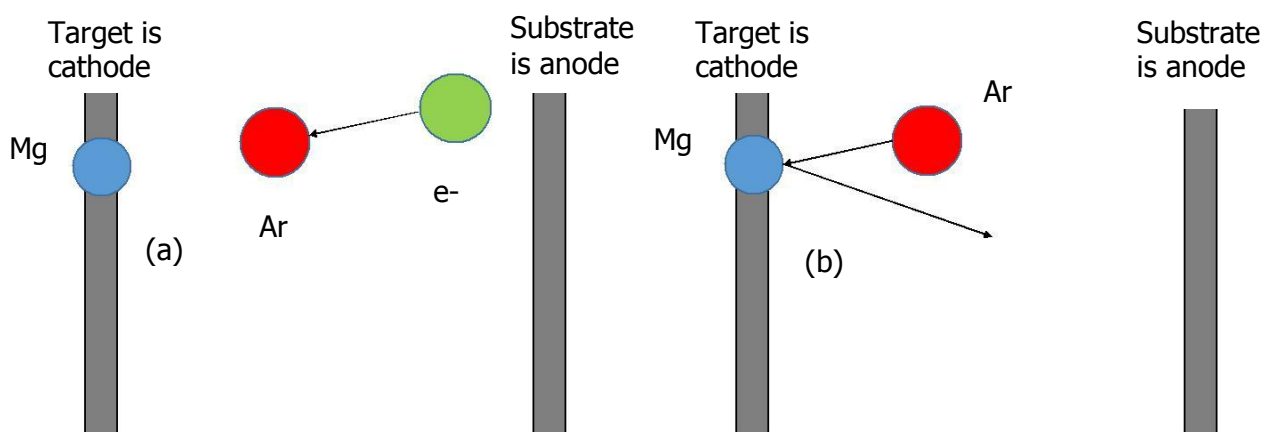


Fig 4.1 Schematic appearance of magnetron sputtering process (a) Due to potential difference between the cathode and anode electrons are generated which corresponding with argon atoms. (b) The positive charged Ar ions bombard Mg target which can deposit the thin films.

In Fig 4.2 a unique CFUBMSIP (Closed Field Unbalanced Magnetron Sputter Ion Plating) has advantages over conventional sputtering systems. The sketch is shown below. Sample holder is in the middle which is rotation. The arrangement of the magnetrons is that alternating poles on the target materials (cathode). The plasma can enhance the density around the work-region (anode).

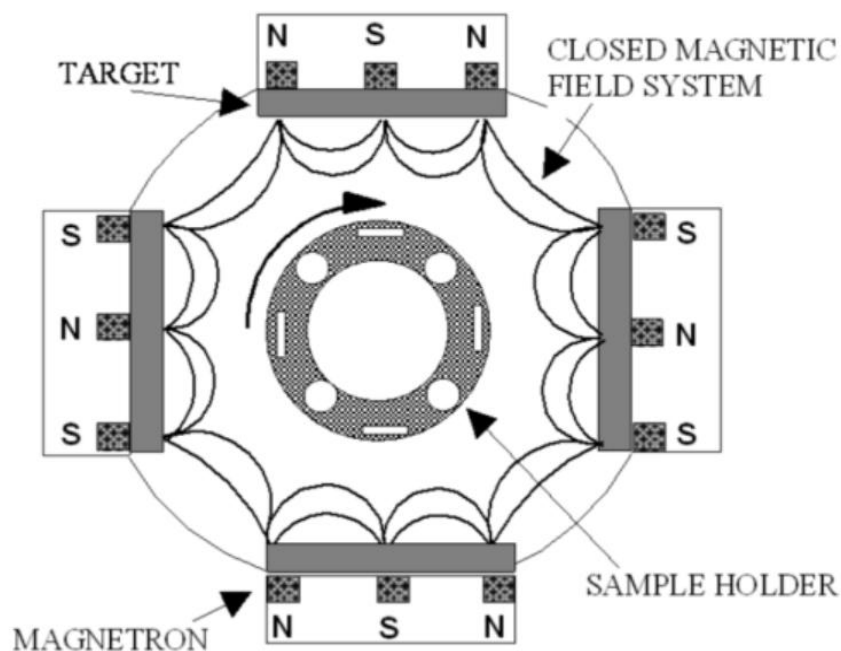


Fig 4.2 the schematic representation of Teer Coatings CFUBMSIP system used in work. The polarity of the adjacent magnetrons is opposite; showing magnetic field lines link up and plasma density is increased. This has advantage for material use, homogenous and uniform coatings. [74]

The system is closed magnetic field system. In comparison, conventional balanced and unbalanced magnetron systems have less confinement of plasma. The high density of plasma

has the bombardment of the work piece with a high number of lower energy ions which is shown in Fig 4.3. The field lines are towards the chamber walls instead of closing. The ion current density is low in the substrate region. The advantages of this system are that it can improve the homogeneity and crystallographic perfection.

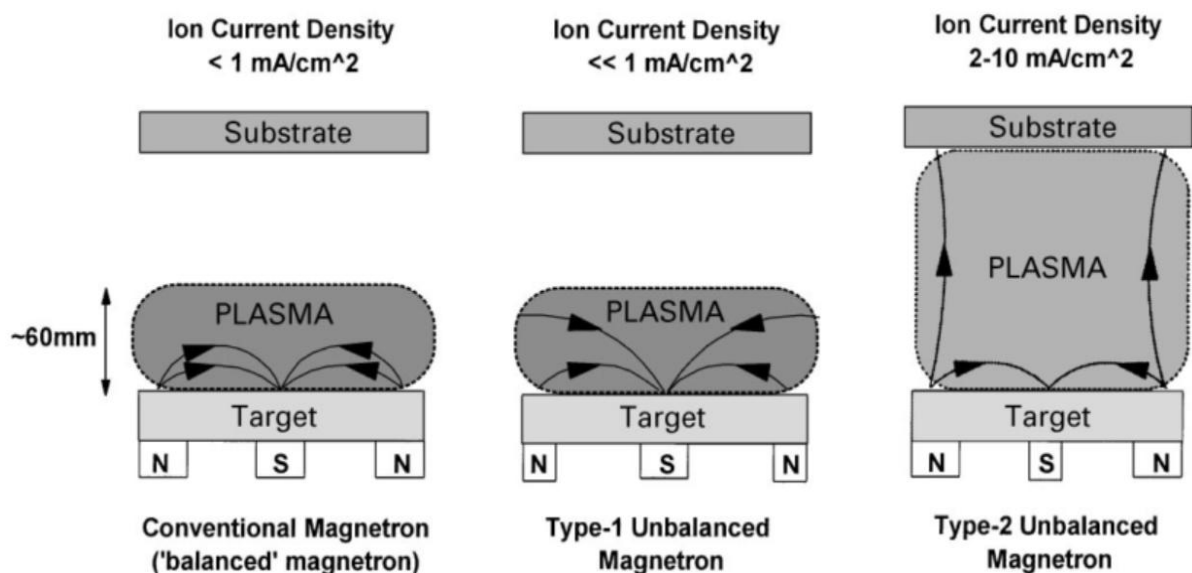


Fig 4.3 Schematic representation of the plasma confinement observed in conventional and unbalanced magnetrons Left: Conventional magnetron sputtering with a small volume of plasma trapped in front of the target. Middle: Unbalanced magnetron with ion current density lower than 1 mA cm<sup>-2</sup>. Right: Unbalanced magnetron with greater plasma volume and influence on the directionality of ballistic target ions. [74]

#### 4.2 Confocal microscopy and SEM

Macroscopic photos were taken by using Confocal microscopy (Olympus LEXT 3100 series). The optical behaviors of Mg thin films can be measured and some features are visible to our eyes by Confocal microscopy. The magnification can be changed from 5 times to 100 times. By scanning through a number of Z planes, the 3D sample topography can be measured. The pinhole is acted as filters which can be used only in the focus plane. The resolution can be

chosen dependent of the area of samples. The schematic picture of the operating principles of Confocal microscopy is shown in the Fig 4.4.

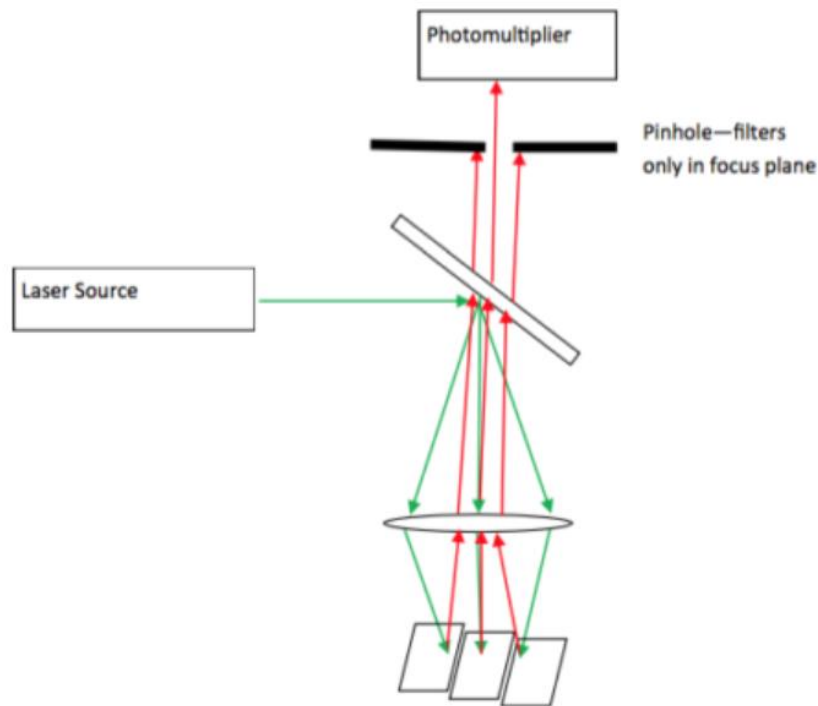


Fig 4.4 Schematic diagram of the Confocal microscopy The pinhole is used to only detect items within a very specific focal plane allowing a 3D layered image to be built up through a variety of Z axis scanning.

Comparing with Confocal microscopy, the microscopic photos can be measured through SEM. The microstructure characterization was the important features which were detected by a JEOL 7000 FEG SEM and a Phillips ESEM. The operating principle is using a focused beam of electron which can produce the image of a sample by scanning. The electron produces various signals which can obtain the image of sample's surface topography and composition. As shown in Fig 4.4, the electron gun produces electrons with using a hot tungsten filament. Then the electrons are emitted and accelerated. A condenser lens and an objective lens focus the electron beam onto the samples' surface.

In Fig 4.5, electron can interact with samples in different ways. At first, the electrons can go through the sample. These electrons have low energy which is called secondary electrons. These electrons can create microstructure images which show 3D features. At second, some electrons can collide with the nucleus of the atoms in the sample which produces high energy back scattered electrons. The angle can be limited by limiting aperture. Thus this technique can be used to identify densities and phases of different sample. It is useful to detect the multilayer of the Mg thin films. In additions to image the features, SEM can analyze the chemical composition of different elements based on EDX analysis.

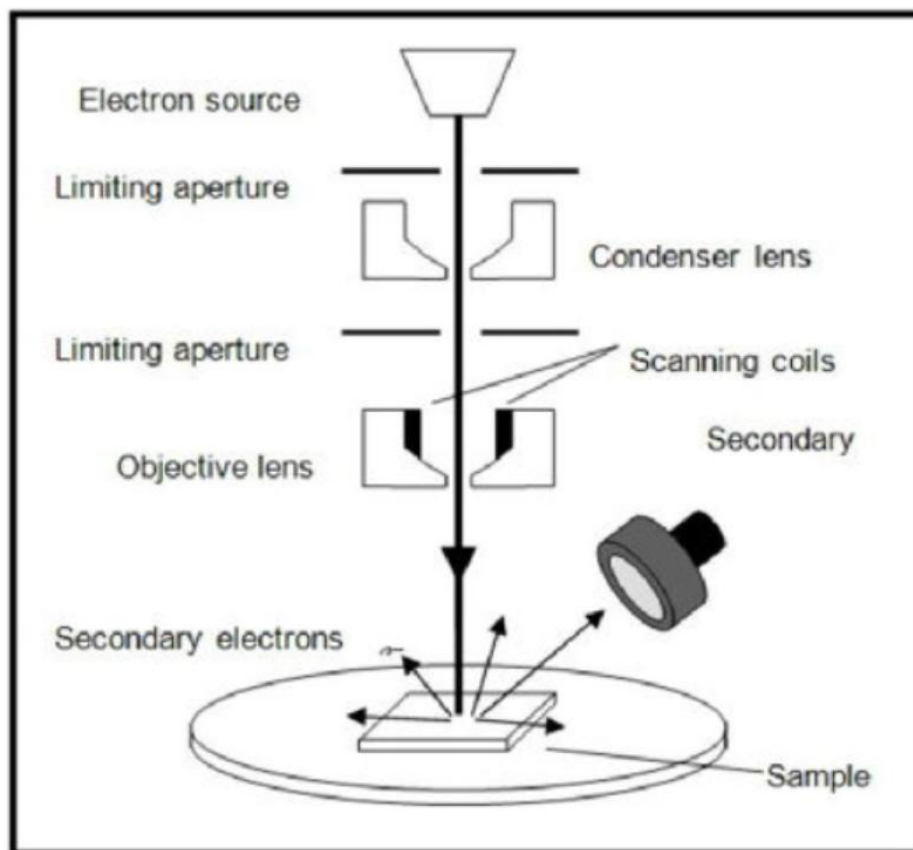


Fig 4.5 a schematic diagram is showing the operating principle of the traditional SEM. [75]

### 4.3 XRD (X-ray diffraction)

XRD is one of the most powerful tools for the study of sample's crystallographic properties. As the wavelength has the relationship with the lattice spacing. Diffraction can occur and follow the Bragg's law which the equation is shown below. The  $\lambda$  is an incident X-ray beam of given wavelength  $d$ .  $n$  is a positive integer. Diffraction will occur at a given angle of incidence in Fig 4.6. The equation is shown below:

$$n\lambda = 2d\sin\theta \quad (16)$$

The angle of incidence which produces a diffraction signal shows coherent scattering. If we assumed that the sample is powder like, an infinite number of grains will arrange in an infinite number of orientations. The inter-planar distance changes due to the observed plane. Each pattern of the peaks will be the unique of the given materials.

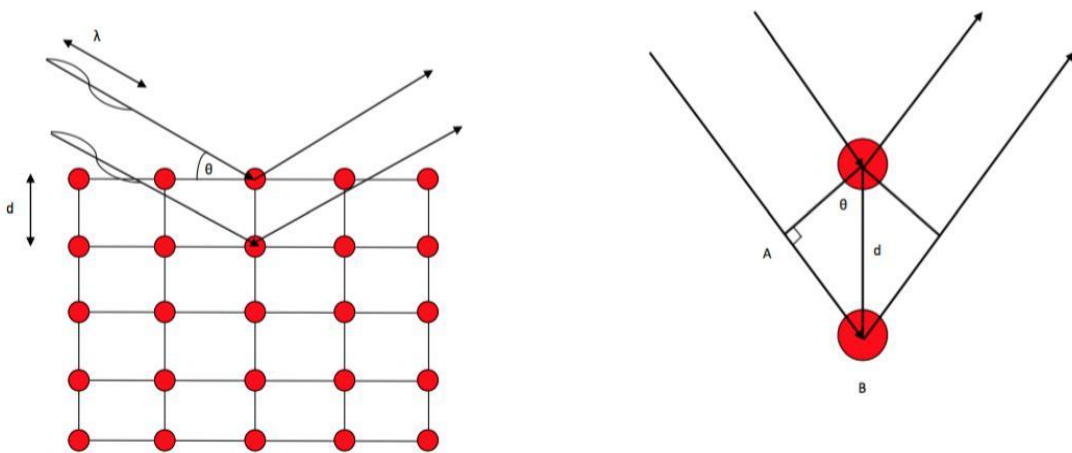


Fig 4.6 Geometric representation of Bragg's law and the assumptions required to generate a powder diffraction pattern through XRD measurement.

XRD can be used at room temperature or various temperatures. In Fig 4.7, a Bruker D8 Advance diffractometer was used. The copper source was used with the wavelength of 0.15418 nm. A divergent slit in the range of 0.1 to 0.6 mm was used for enhance the peak broadening. The XRD alignment can be calibrated with a standard  $\text{Al}_2\text{O}_3$ . As for ex-situ XRD measurements, the samples are exposed to air. Mg thin film is stable in atmosphere. It was

usually to use a detector scan with an incident angle of around  $2^\circ$  instead of the locked coupled scan.

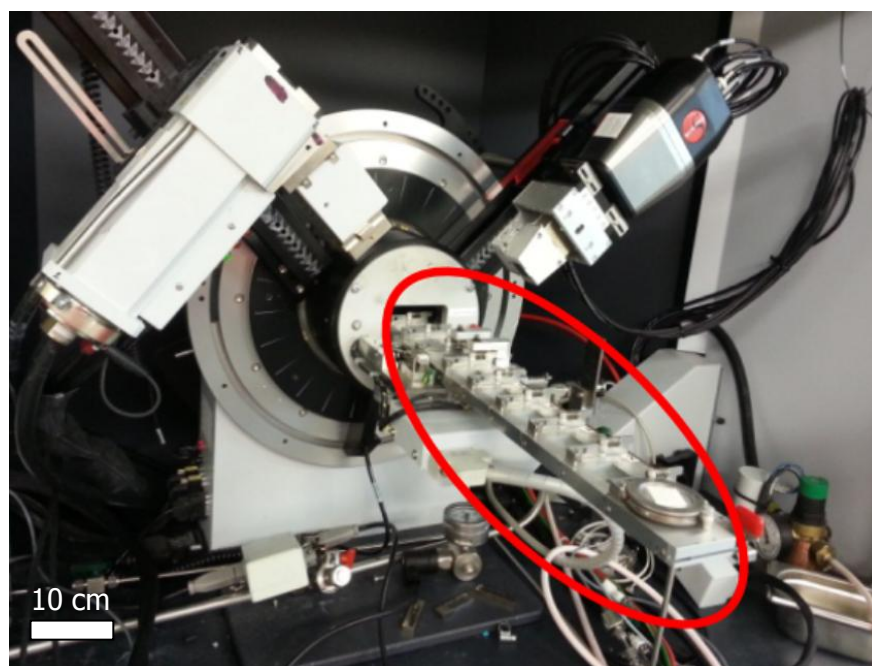


Fig 4.7 Photographs of XRD equipment with multichanger unit attached under the room temperature scanning

For in-situ XRD, an Anton Paar XRK 900 cell was used to obtain results with different temperatures and pressures. The thin films' kinetic properties can be measured by in-situ XRD in the hydrogenation process. The alignment of the sample was used by movement in a vertical (Z) axis. The highest intensity of the peaks could be observed. The alignment is to be used for improving the measurement accuracy.

By analysis of XRD patterns, the IGOR pro graphical software can be used to fit the peak shapes, peak area, peak intensity and positions along with the FWHM (full width at half maximum). FWHM is used to calculate the grain size by using the Scherrer equation.

The Scherrer equation is shown below:

$$D = K\lambda / \beta \sin\theta \quad (17)$$

In the equation,  $K$  is a shape factor which is constant value of 0.9,  $\lambda$  is the wavelength,  $\beta$  is the FWHM and  $\theta$  is the peak position. The equation assumes a spherical grain and has limitation down to 0.1 to 0.2 microns. Besides, the lattice parameters were obtained from the ICSD (Inorganic crystal structure database). Williamson Hall method is another method to calculate the lattice strain and Mg thin film grain size.

#### 4.4 Hydrogenation chamber

For long term hydrogenation of samples, the hydrogenation chamber can be used. The chamber is made by steel reactor. For the samples, we hydrogenated them at low pressures from 1bar to 3bar. The accuracy can be detected. The samples were then placed into a furnace with a thermocouple located next to the samples for accurate temperature control. For dehydrogenation, the hydrogenation chamber can control in the vacuum atmosphere. The temperature can be modified by thermocouple and the pressure in the furnace can be controlled by the pressure valves.

#### 4.5 Profilometer

Profilometer can measure the surface conditions of Mg-based thin films. Surface roughness and buckling are shown in Profilometer measurement. During the surface scanning, interface shear stress can be calculated by Stoney equation. In this equation, scan speed and scan length will have effects on the results of interface shear stress. The scan speed is 0.1mm/s or 0.05 mm/s. The scan length is tried from 1 mm to 5 mm. The longer the scan length the more accuracy the results are. Thus, the 5 mm scan length is chosen at last.

#### 4.6 Four probe and two probe resistivity measurement

There are two methods to measure thin films' resistivity. One method is using two probes and another one is using four probes sheet measurement. By comparing, four probe sheet resistivity method is more accurate than two probe measurement because two probe has the limitation of the contact resistivity. It assumes that each distance of two probes are the same. The equation is  $R=U/I$ . At the beginning, the resistivity can be written as  $R_0$ . We can use the  $R/R_0$  to represent the resistance change of Mg based thin films under the different hydrogenation state.

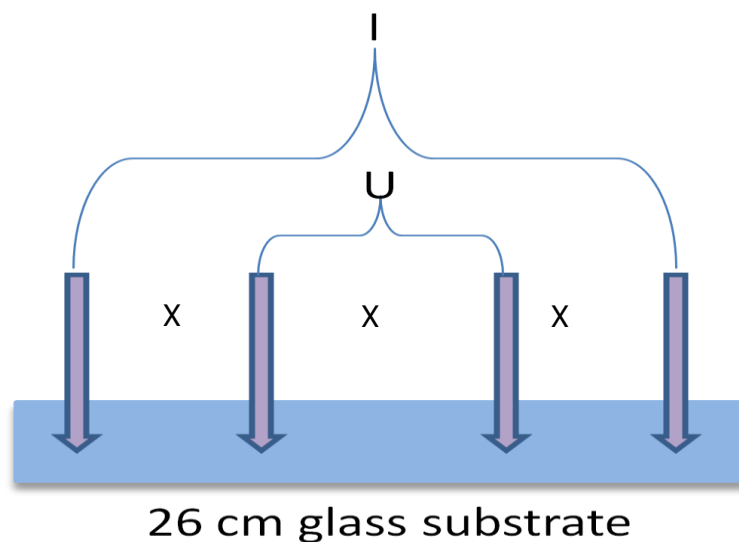


Fig 4.8 Schematic image of four probe measurement of sheet resistivity, each distance of two probes is X cm. The resistance value is measured by the equation of  $R=U/I$ .

#### 4.7 Optical UV-laser

Optical UV laser is a kind of technology to focus on light properties. The transmittance index and reflectance index can be measured by optical UV-laser technology. At first, optical UV-laser can measure the baseline with using the glass substrate as an example. Then the Mg thin film's transmittance and reflectance can be measured through optical UV-laser. There are

some relationship between the light absorption and light transmittance. According to the Beer's law, transmittance is regarded as T and absorbance is indicated as A. The equation of transmittance is shown below:

$$T = P/P_0 \quad (18)$$

% Transmittance, %T = 100T

$P_0$  is a beam of monochromatic radiation of radiant power. P is absorption take place and the beam of radiation leaving the sample has radiant power. The equation of absorbance is shown below:

$$\text{Absorbance, } A = \log_{10} P_0/P \quad (19)$$

$$\text{Thus } A = 2 - \log_{10} \%T \quad (20)$$

#### 4.8 TPD measurement (RGA)

TPD is short for temperature programmed desorption. This technique heated samples at a constant rate and is a thermodynamic measure of a given compound. It is most often used for the analysis of multilayer of gas species adsorbed onto single crystals. The schematic diagram of TPD is shown below. The sample is put into sample container with the furnace to heat it up. The thermocouple can measure the temperature change. Vacuum gauge can control the dehydrogenation conditions. Residual gas analysis (RGA) performed under high vacuum conditions (eg  $< 10^{-5}$  mbar).

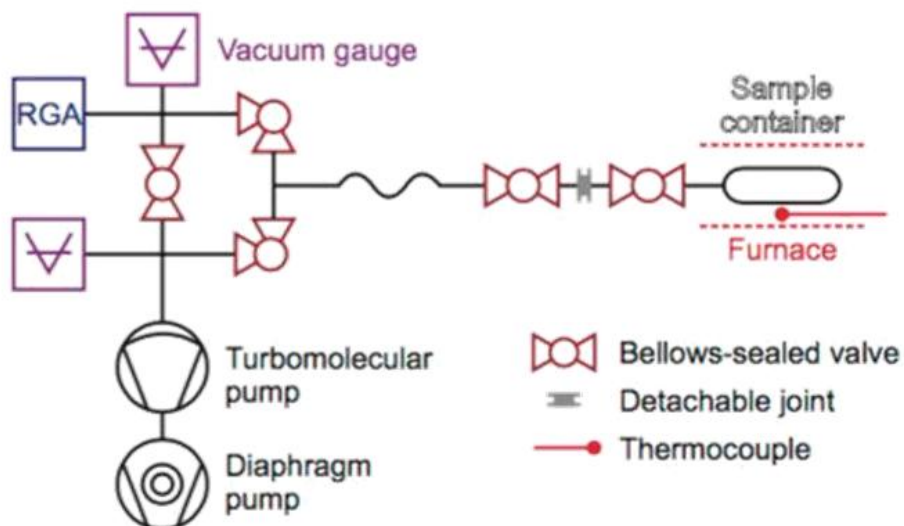


Fig 4.9 Schematic diagram of TPD is used in this work. A mass spectrometer can be used to monitor the desorbed gas species from the sample which is heated at a constant rate in a UHV atmosphere. The UHV atmosphere is generated by a rotary backed turbo molecular vacuum pump. [76]

As shown in Fig 4.10, the mass spectrometer was used for residual gases investigation. The schematic of a QMS (quadrupole mass spectrometer) is shown below. Gas flows with a hot tungsten filament which acts as a high energy electron source. The ions go through the quadrupole rods are resonant ion (detected). The quadrupole mass analyzer has four rods which are electrified with DC and RF currents. The alternating RF brings different  $m/z$  into focus on the detector to build up mass spectrum. The motion of ions through the electric fields will depend on  $m/z$  value.

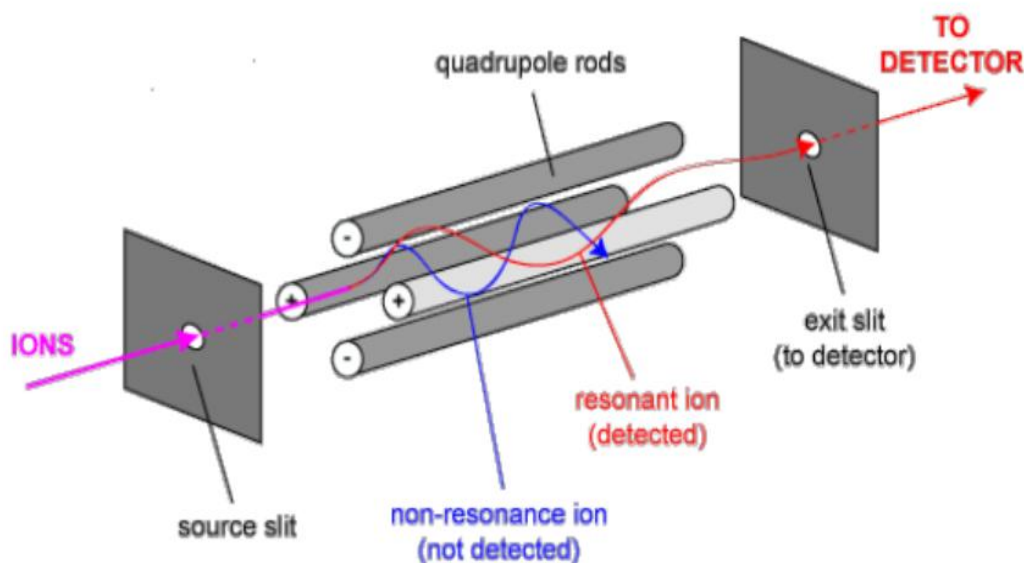


Fig 4.10 Operating schematic of a quadrupole mass spectrometer QMS. Electrons ionize a sample gas, which is then selectively filtered with the use of RF currents in a four pole configuration. [77]

#### 4.9 Raman spectroscopy

Raman spectroscopy is a kind of technique which can observe the vibrational mode and other low frequency modes. It relies on inelastic scattering or Raman scattering. Raman technique can measure crystalline, amorphous and liquid samples. The laser is focused on as-measured samples. The laser light can interact with molecular vibrations, phonons or other excitations in the system which will lead to the laser photons being shifted up and down. As shown in Fig 4.11, the energy level program was showing the states within Raman spectra. Raman shifts are reported in wave-numbers which have units of inverse length. In order to convert between spectral wavelength and wave-number of shift, the formula is shown below in Fig 4.11. Raman spectroscopy can be used to identify molecules and chemical bonding at the same time. The disadvantage of Raman is limited database through using DFT calculations to predict vibrations. The picture of Raman spectroscopy was shown in Fig 4.12. The samples

were placed and measured in Raman cell under the room temperature. In Fig 4.12, the construction of Raman machine including the CCD, pinhole, grating and focusing length was shown below.

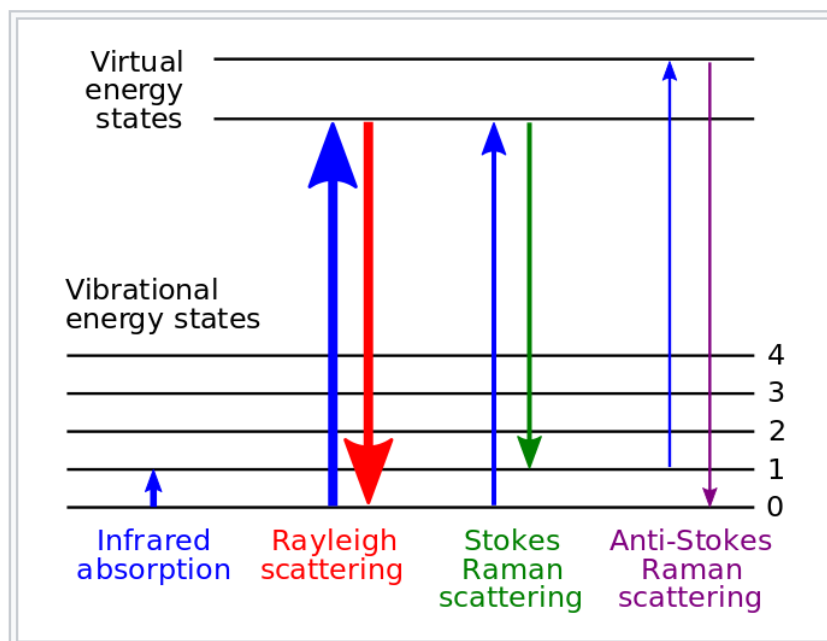


Fig 4.11 Energy level schematic picture showing the states involved in Raman spectra

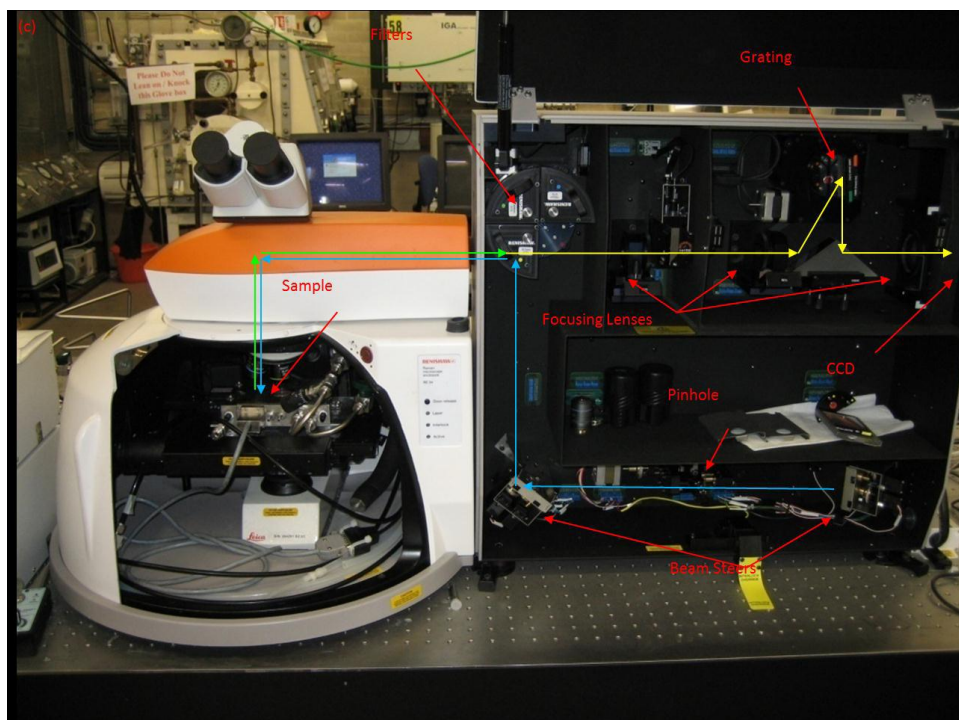


Fig 4.12 a schematic picture of Raman spectroscopy with sample in the Raman cell under room temperature The construction of Raman spectroscopy is shown in the picture.

## 5. Results

All the results are collected in this chapter. In this chapter, the results are described clearly which is relevant with these figures. All the results are shown in a correct way. The results are including effects of sputtering conditions and parameters, en-situ and in-situ XRD results, microstructure of Mg thin films, buckling appearance, surface roughness, thin film thickness, sheet resistivity and the interface shear stress. In the results, hydrogenation and dehydrogenation behaviors of Mg thin films were investigated which were relevant with research aims of hydrogen storage. Besides, the relationship between hydrogen sorption properties and thin films' physical properties can be characterized as well which could be useful for hydrogen sensors investigations.

### 5.1 Effect of sputtering conditions

In Fig 5.1.1, Mg thin films without Pd top layer can be characterized below. Only Mg layer is deposited onto glass substrate. Mg peaks are shown clearly. The highest Mg peak with high Mg intensity has the angle about  $35^\circ$ . The Mg miller planes are about (002) and (004) which are shown below.

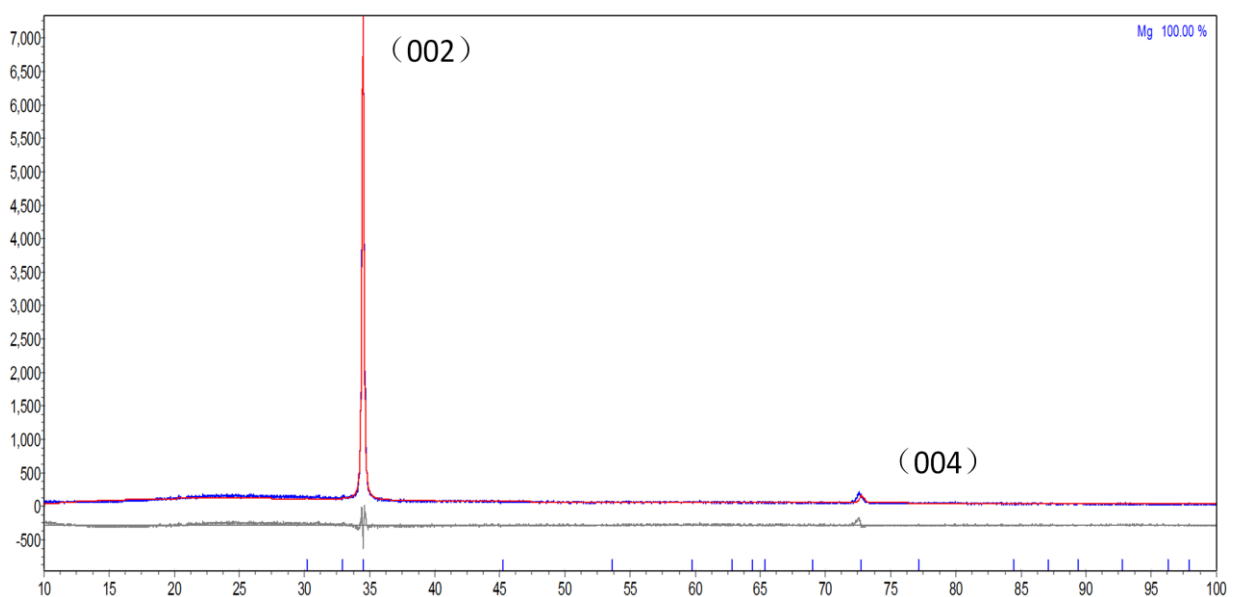


Fig 5.1.1 Topas modifications of sample Mg thin film showing the Mg peak position and miller plane of (002) and (004) planes

As shown in Fig 5.1.2, all the samples are as-sputtered materials. All the Mg films were deposited onto glass substrate with different sputtering parameters. The sputtering current and the Ar flow are both parameters which can influence the Mg peaks shift among sample (a) to sample (e). The Mg has (002) miller plane and the lattice parameter changes under different sputtering parameters as well. On 2A 25 sccm (standard-state cubic centimeter per minute) Ar conditions (sample e), the peak has the highest Mg intensity among these samples which the Mg position is around  $34.398^\circ$ . As the current increases, the peak intensity increases as well. Mg peaks intensity reduces due to the Ar flow increasing. Besides, as the sputtering parameters change, the Mg peaks shift which leads to lattice parameter change. Higher current causes the Mg peak shift to the left as shown in sample (e).

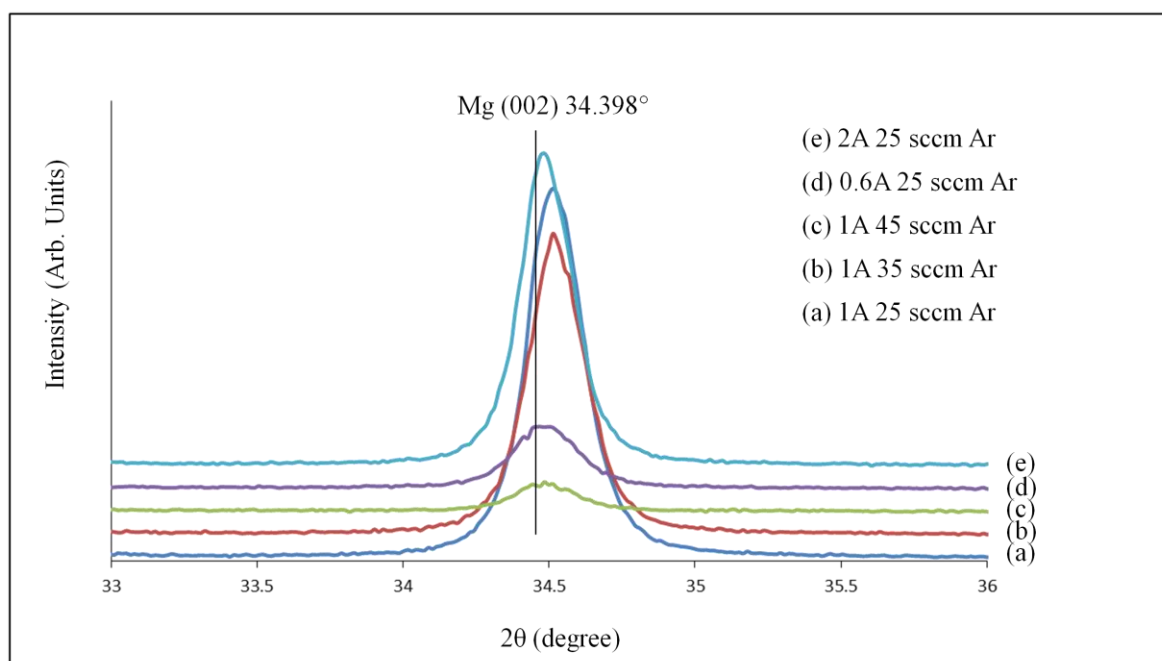


Fig 5.1.2 XRD measurement at room temperature at various sputtering conditions sample (a): 1A 25 sccm Ar, (b): 1A 35 sccm Ar, (c): 1A 45 sccm Ar, (d): 0.6A 25 sccm Ar, (e): 2A 25 sccm Ar deposited on glass substrate

Among sample (a), (b) and (c), Mg crystallite size decreases with increasing of Ar flow, which leads to higher Mg buckling stress. Higher argon flow provides higher base pressure which increases the Ar bombardment energy. High base pressure leads to low atom mobility in Mg thin films. [78] More energy can deposited more atoms leading to denser film. Among samples (a), (d) and (e), Mg crystallite size increases which leads to Mg buckling stress reduction with the bias current increases. Linear relationship between film buckling stress and magnetron current is shown in Table 5.1.3. Higher current leads to good Mg crystal orientation which reduces buckling stress between crystals. All the samples' buckling stress is below 1 GPa. Besides, Mg intensity is different among sample (a)-(e), which is due to different Mg quantity. Sample (e) indicates the best Mg crystallinity which is good for XRD detection. Same coating time (5 minutes) has been chosen. Various sputtering conditions also influence the thickness of Mg thin film. Higher Ar flow rate leads to thicker and denser films. With increase of sputtering current, Mg thickness increases. Base on calculation, sputtering speed of Mg is 0.9 nm/s-1.5 nm/s and sputtering speed of Pd is about 2 nm/s. Mg buckling stress is around 1 GPa based on Scherrer equation and Jade software. The lattice parameter of Mg can be measured by Topas software. The results show that higher current with less Mg buckling stress has the largest c-axis value among all the samples. The lattice parameter of c value of sample (e) is about 5.44016 which is extended comparing to the sample (a), (b), (c) and (d). Sample (a), (b), (c) and (d) have similar lattice c value. Their samples' c value is about 5.2. Higher current provides higher value in c-axis orientations. The lattice parameters of both a and b are similar among sample (b), (c) and (d) which the value is around 3.2.

Table 5.1.3 Sputtering parameters influence on Mg thin film thickness, Mg crystallite size, Mg buckling stress and lattice parameter of Mg. All the data including the error bar is also including as shown below.

As-sputtered sample	Profilometer measure thickness of Mg thin film	Scherrer equation measures crystallite size of Mg	Mg buckling stress	Lattice parameter of Mg measured by Topas software
(a) 1A 25 sccm	200 nm $\pm$ 10 nm	76.0 nm $\pm$ 0.4 nm	749 MPa	a=b= 3.44502_0.00304 c= 5.19747_0.00027
(b) 1A 35 sccm	240 nm $\pm$ 10 nm	72.5 nm $\pm$ 0.7 nm	786 MPa	a=b= 3.21418_0.00678 c= 5.19677_0.00031
(c) 1A 45 sccm	270 nm $\pm$ 10 nm	62.2 nm $\pm$ 0.9 nm	916 MPa	a=b= 3.25135_0.01390 c= 5.20157_0.00161
(d) 0.6A 25 sccm	170 nm $\pm$ 10 nm	63.2 nm $\pm$ 0.5 nm	901 MPa	a=b= 3.23996_0.03184 c= 5.20127_0.00079
(e) 2A 25 sccm	230 nm $\pm$ 10 nm	82.8 nm $\pm$ 0.6 nm	688 MPa	a=b= 3.41506_0.00197 c= 5.44016_0.01070

In Fig 5.1.4, Mg morphology is shown. The grain size and porosities were observed. SEM reveals that the films grow with basal texture and the hexagonal platelets of Mg are visible. From sample (a) to sample (e), the grain size is around the 200 nm to 350 nm. Among all the samples, the grain size looks similar. In sample (b) and sample (d), small inhomogeneous regions appear and the grains have grouped together. The grain size can be measured by SEM which is shown in Table 5.1.5.

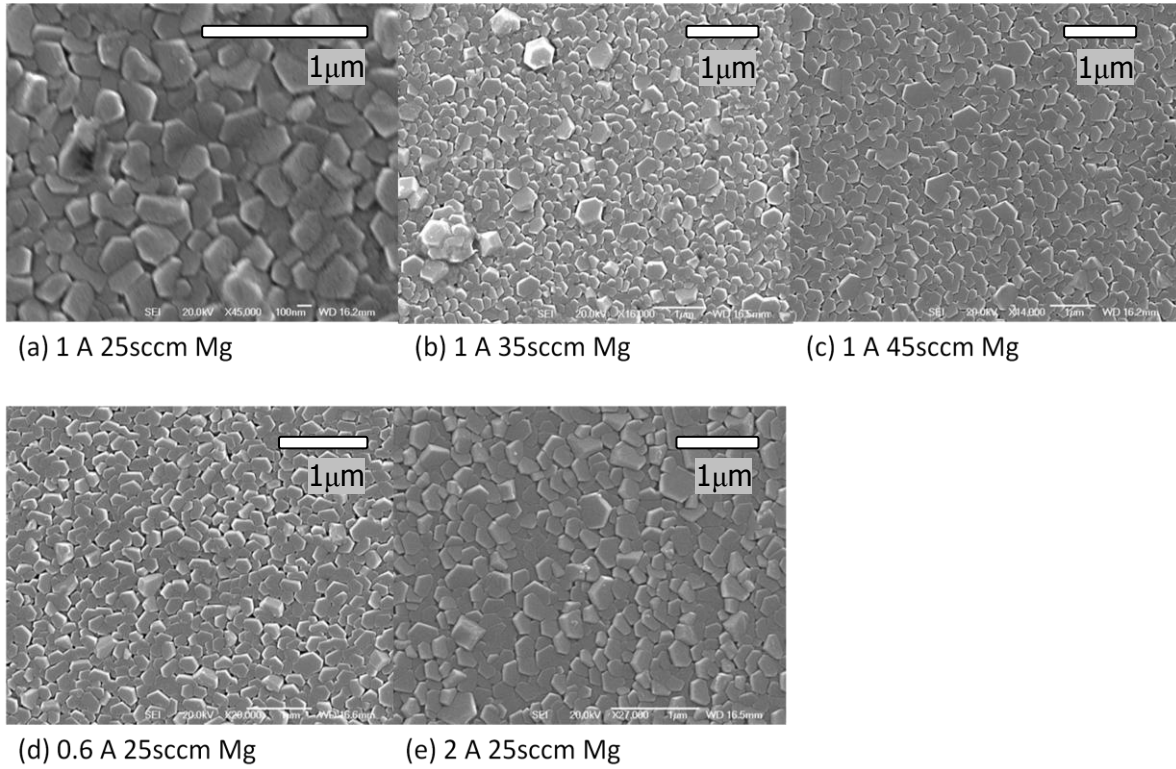


Fig 5.1.4 SEM microscopy of sample (a) to (e) Inhomogeneous grain clusters is observed as well as surface porosities.

Table 5.1.5 SEM measurement of sample grain size from the sample (a) to sample (e) The grain size of Mg thin film samples are shown below.

Sample ID	Grain size measurement by SEM
Sample (a) 1A 25 sccm	Around 200 nm
Sample (b) 1A 35 sccm	Around 350 nm
Sample (c) 1A 45 sccm	Around 300 nm
Sample (d) 0.6A 25 sccm	Around 260 nm
Sample (e) 2A 25 sccm	Around 240 nm

### 5.1.1 Summary

In Fig 5.1.2, it shows that both current and Ar flow are the two parameters to influence the peaks positions of XRD. High current improves the lattice parameter of c value. High Ar flow indicates high base pressure with high bombard energy. Mg buckling stress is lower than 1 GPa which was calculated through XRD software. Besides, morphology was shown in Fig 5.1.4, which shows the grain size of Mg thin film. The grain size is around 200 to 350 nm which is larger than the results measured by Jade software. The actual grain size should be between them in nano-scale.

## 5.2 XRD results (under He or H<sub>2</sub>)

Samples can be detected under room temperature. Peak property is characterized. Besides, XRD can also be used at various temperatures to measure samples. He atmosphere can find the alloying phase properties of Mg based thin films. Under H<sub>2</sub> atmosphere, samples hydrogen absorption properties can be characterized with the temperature increase. After hydrogenation, new phase can be detected through XRD pattern. The pressure is controlled at 3 bar during in-situ XRD. The plateau pressure is 2 bar. The temperature is increasing from room temperature to 300 °C. Every temperature step is around 25 to 50 °C.

### 5.2.1 Room temperature XRD

As-received MgH<sub>2</sub> powders were measured by XRD at room temperature. MgH<sub>2</sub> and Mg peaks were both observed in Fig 5.2.1. The main peaks are MgH<sub>2</sub> with small peaks of Mg. The sample is well stored without any oxidation. The miller planes are the random orientations which are shown below.

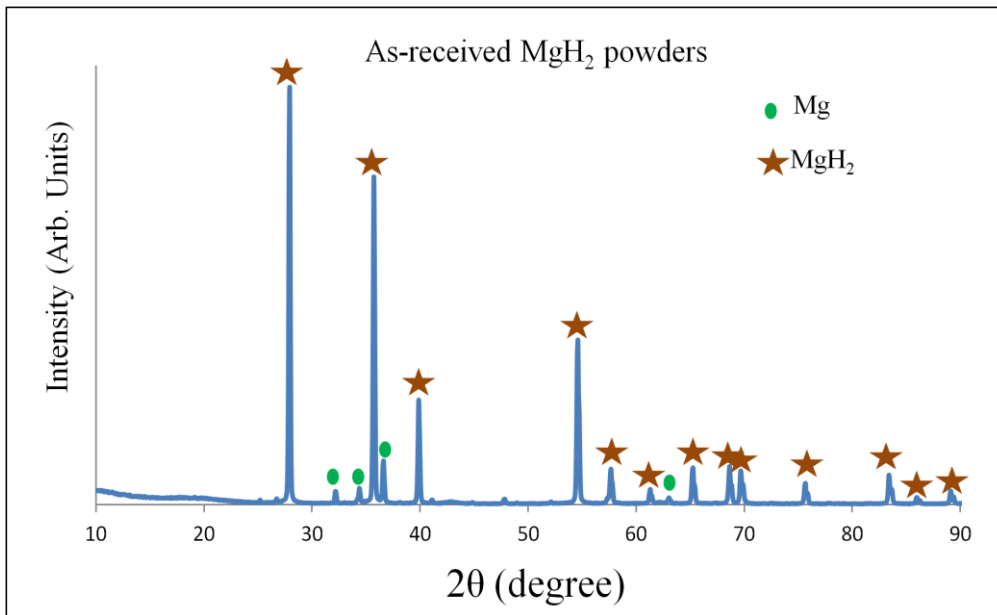


Fig 5.2.1 Ex-situ XRD results of as-received  $\text{MgH}_2$  powders. The main peaks are represented as  $\text{MgH}_2$  and the other small peaks are Mg.

In Fig 5.2.2, Pd has the sharp peak around 40 degree with (111) miller plane. Mg has (002) miller plane around 35 degree which match previous paper. [78] Detect scan and locked coupled scan are two methods for scanning samples. As the detector scan angle increases, Mg peaks become sharp and clear. Under locked coupled conditions, both Pd and Mg peaks can be observed clearly. Thus, it seems locked coupled condition has less influence on Mg and Pd peaks comparing with detector scan. Detect scan  $4^\circ$  and  $8^\circ$  have good peaks which can be well observed by XRD among all the Mg based thin film samples.

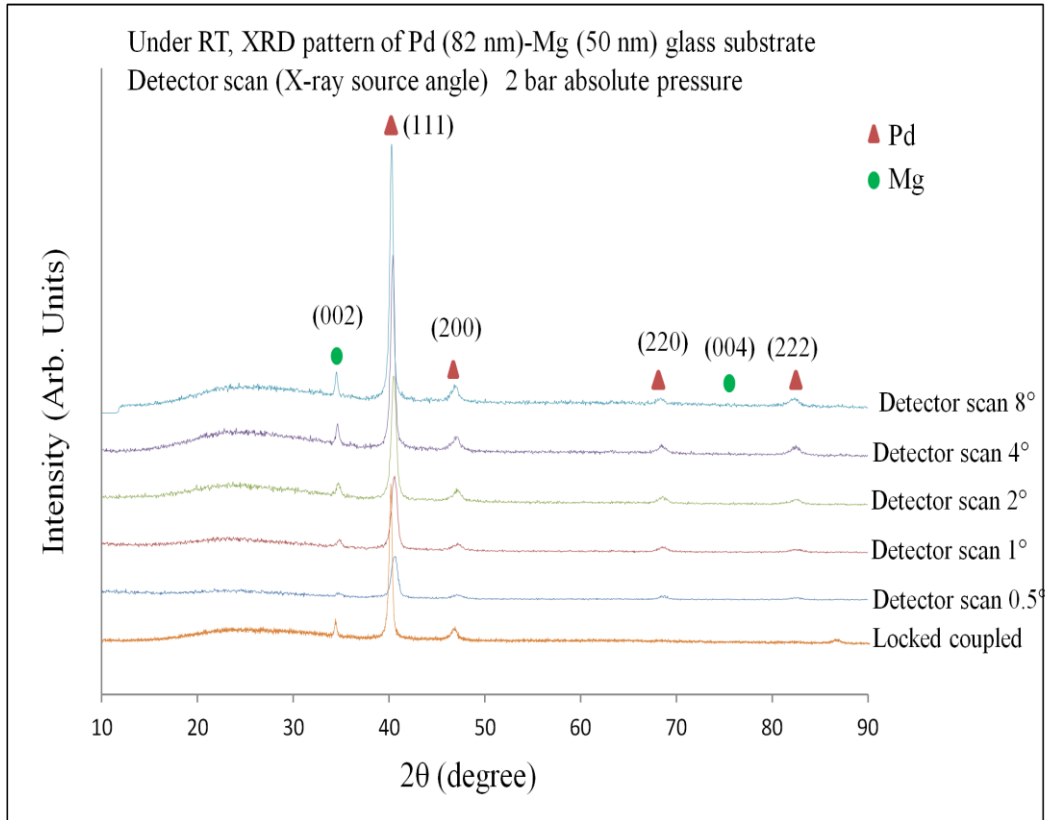


Fig 5.2.2 Room temperature XRD measurement of sample Pd(80 nm)-Mg(50 nm) glass substrate with different detector scan conditions (angle) or Locked coupled conditions. Mg out of plane texture (002) is at around 35° and Pd plane texture (111) is at about 40°.

Samples (A)-(D) were characterized by XRD at room temperature. They are all as-sputtered samples. Pd, Mg, Si and Ti peaks were observed in Fig. 5.2.3. Mg intensity is improved with the increasing thickness of Mg. No alteration is in observed growth direction. The sputtering conditions of sample (A), sample (B), sample (C) and sample (D) were shown in table 5.2.1. The deposition conditions include DC bias voltage and base pressure. The sputtering frequency is 250 Hz and DC bias voltage is 50 V. The base pressure is  $1.2 \times 10^{-7}$  bar.

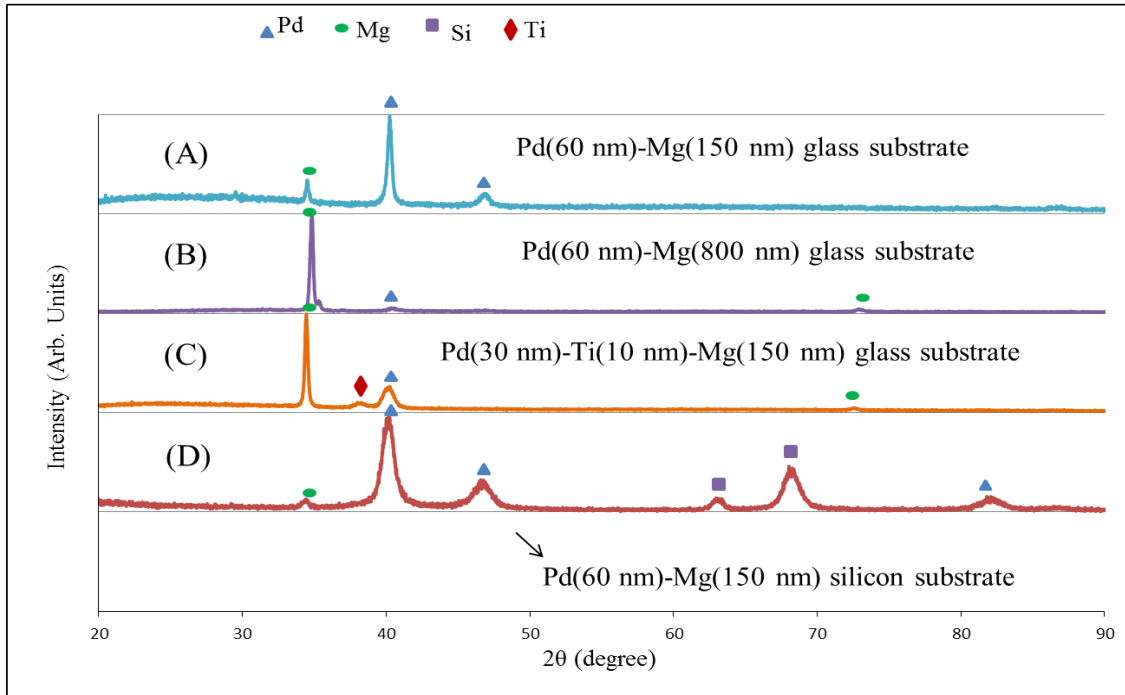


Fig 5.2.3 Ex-situ XRD of as-sputtered samples (A)-(D). (A): Pd(60 nm)-Mg(150 nm) glass substrate; (B): Pd(60 nm)-Mg(800 nm) glass substrate; (C): Pd(30 nm)-Ti(10 nm)-Mg(150 nm) glass substrate; (D): Pd(60 nm)-Mg(150 nm) silicon substrate

Table 5.2.1 Samples (A). sample (B), sample (C) and sample (D) with different sputtering conditions including sputtering current, bias voltage and the sputtering base pressure

Sample ID	Mg current	Pd current	Ti current	DC bias voltage (250 Hz pulsed)	Base pressure
(A) Pd(60nm)-Mg(150nm) glass substrate	1 (A)	1 (A)		50 V	$1.2 \times 10^{-7}$ bar
(B) Pd(60nm)-Mg(800nm) glass substrate	2 (A)	1 (A)		50 V	$1.2 \times 10^{-7}$ bar
(C) Pd(30nm)-Ti(10nm)-Mg(150nm) glass substrate	1 (A)	0.5 (A)	0.75 (A)	50 V	$1.2 \times 10^{-7}$ bar
(D) Pd(60nm)-Mg(150nm) silicon substrate	1 (A)	1 (A)		50 V	$1.2 \times 10^{-7}$ bar

### 5.2.2 In-situ XRD of thin-films under He atmosphere

In Fig. 5.2.4, sample (A) Pd(60 nm)-Mg(150 nm) was measured as a simple model with the heating rate of  $2\text{ }^{\circ}\text{C min}^{-1}$  at 3 bar He atmosphere. Mg phase is reduced to form alloying phase. Around  $300\text{ }^{\circ}\text{C}$ , Mg peak disappears. After calculating, the atomic weight percentage of Mg is about 26.8%. According to the Pd-Mg binary phase diagram, Mg-Pd alloying phase is confirmed to be  $\text{Mg}_5\text{Pd}_2$  which appears above  $250\text{ }^{\circ}\text{C}$ . At  $300\text{ }^{\circ}\text{C}$ , alloying peaks  $\text{Mg}_5\text{Pd}_2$  can become clearly observation.

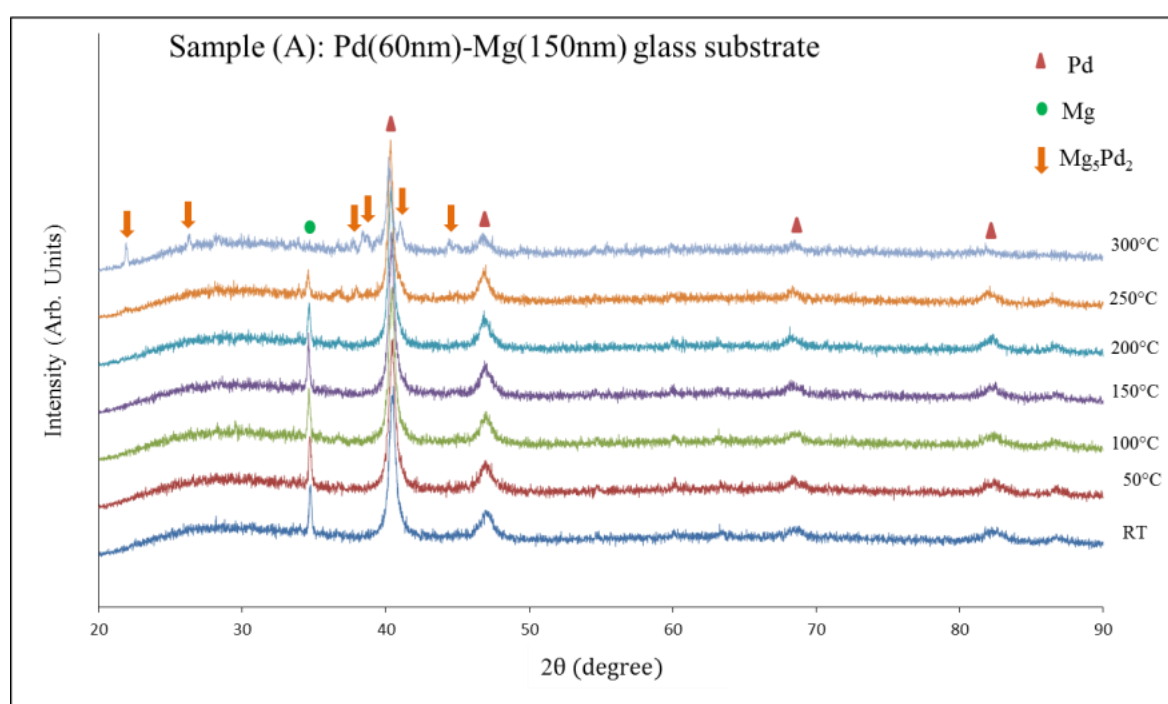


Fig 5.2.4 Sample (A) heated at 3 bar He from room temperature to  $300\text{ }^{\circ}\text{C}$  (room temperature,  $50\text{ }^{\circ}\text{C}$ ,  $100\text{ }^{\circ}\text{C}$ ,  $150\text{ }^{\circ}\text{C}$ ,  $200\text{ }^{\circ}\text{C}$ ,  $250\text{ }^{\circ}\text{C}$ ,  $300\text{ }^{\circ}\text{C}$ )

### 5.2.3 In-situ XRD of thin-films under $\text{H}_2$ atmosphere

Fig. 5.2.5 shows in-situ XRD of sample (A) measured at the heating rate of  $2\text{ }^{\circ}\text{C min}^{-1}$  at 3 bar  $\text{H}_2$ . As the temperature increases, Mg phase is reduced and  $\text{MgH}_2$  phase is observed.  $\text{Mg}_5\text{Pd}_2$  alloying phase is observed in high temperature ( $300\text{ }^{\circ}\text{C}$ ) but it is reduced in Fig. 5.2.5

comparing with Fig. 5.2.4. Pd can absorb hydrogen at room temperature to form PdH<sub>0.6</sub> and PdH<sub>0.6</sub> dissociates hydrogen at high temperature around 225 °C. Mg began to hydrogenate at room temperature and fully hydrogenated at 125 °C. Pd hydrogenated at room temperature to form PdH<sub>0.6</sub> then dehydrogenated at about 175 °C. Contour plots of in-situ XRD patterns indicate the properties of hydrogen absorption temperature.

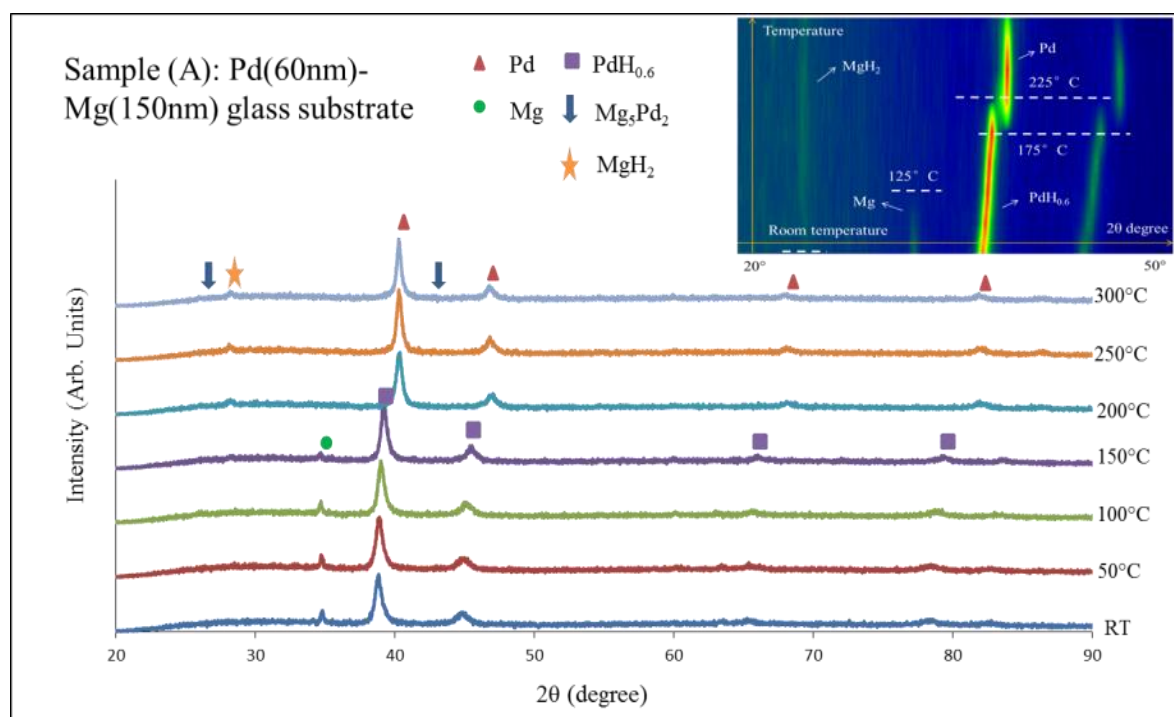


Fig. 5.2.5 Sample (A) heated at 3 bar H<sub>2</sub> from room temperature to 300 °C (RT, 50 °C, 100 °C, 150 °C, 200 °C, 250 °C, 300 °C) Contour plots of in-situ XRD patterns of sample (A) heated under H<sub>2</sub> (3 bar 100 ml/min) from RT to 300 °C. The brighter color corresponds to higher peak intensity.

Sample Pd(60 nm)-Mg(250 nm) glass substrate was hydrogenated from room temperature to 300 °C. The hydrogenation temperature is a little difference with sample (A) Pd(60 nm)-Mg(150 nm). Pd can absorb hydrogen at room temperature to form PdH<sub>0.6</sub> and PdH<sub>0.6</sub> dissociates hydrogen at 200 °C. Mg began to hydrogenate at about 125 °C and fully hydrogenated at 225 °C. Pd hydrogenated at room temperature then dehydrogenated at about

200 °C. Thicker Mg layer of sample Pd(60 nm)-Mg(250 nm) has higher Mg hydrogenation temperature than thinner thin films of sample (A) shown in Fig 5.2.5 and Fig 5.2.6.

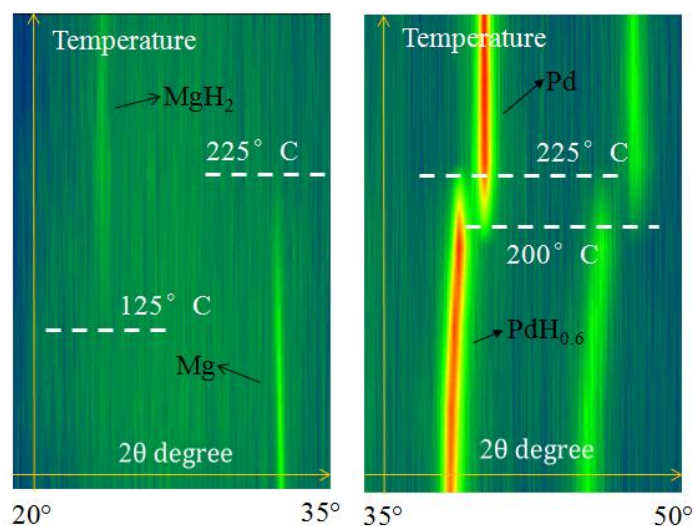


Fig 5.2.6 Contour plots of in-situ XRD patterns of sample Pd(60 nm)-Mg(250 nm) glass substrate heated under H<sub>2</sub> (3 bar 100 ml/min) from room temperature to 300 °C. The brighter color corresponds to higher peak intensity.

After hydrogenation of sample (B) Pd(60 nm)-Mg(800 nm) glass substrate, Pd peaks can be observed around 40 degree. Same sample is hydrogenated under different conditions. At 3 bar 100 °C 24h, only Pd peak is observed during 38-42 degree. While at 3 bar 250 °C 24 hour condition, two more peaks are observed which seems to be the alloying Mg<sub>5</sub>Pd<sub>2</sub>. It shows that high temperature can form new phase of Mg<sub>5</sub>Pd<sub>2</sub> which can reduce Pd intensity which proves the previous results. Higher temperature makes alloying formation according to the Pd-Mg binary phase diagram.

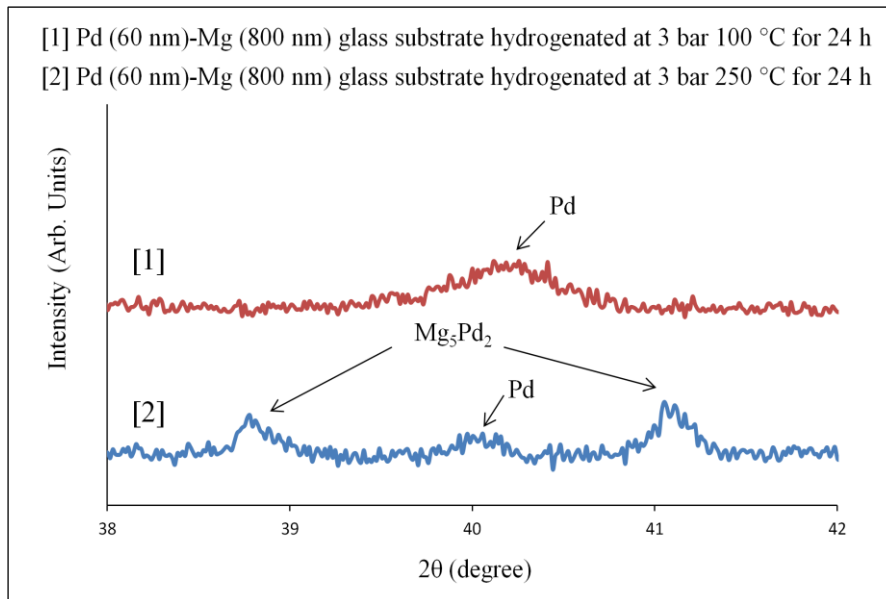


Fig 5.2.7 Sample [1] and sample [2] hydrogenate at 3 bar 100 °C 24 h and 3 bar 250 °C 24 h respectively. After hydrogenation, sample [1] and [2] were measured under ex-situ XRD.

In Fig 5.2.8, at room temperature, Si peaks can be observed at about 55 degree and 60 degree. Sample (D) Pd(60nm)-Mg(150nm) silicon substrate was measured under 3 bar  $H_2$ . Si peaks are clearly observed after temperature change.  $MgH_2$  peaks are less visible to be observed. Pd absorbs hydrogen to form  $PdH_{0.6}$  at room temperature. Then  $PdH_{0.6}$  dissociates  $H_2$  to form Pd during increasing temperature. After cooling down to room temperature, Pd and  $Mg_5Pd_2$  alloy were observed.  $Mg_5Pd_2$  is existence due to the Mg/Pd binary phase diagram. Mg intensity decreases with the temperature changes. Besides, Mg can be alloyed with Si to form  $Mg_2Si$  according to the Mg-Si binary phase diagram as shown below in Fig 5.2.9. In binary phase diagram Si can alloy with Mg to form  $Mg_2Si$  without considering Si mass percent. As shown in Fig 5.2.9, Pd-Mg-Y multilayer will form  $Mg_2Si$  after temperature heating up to temperature 500 K. No matter how the Si mass percent changes,  $Mg_2Si$  phase will form.

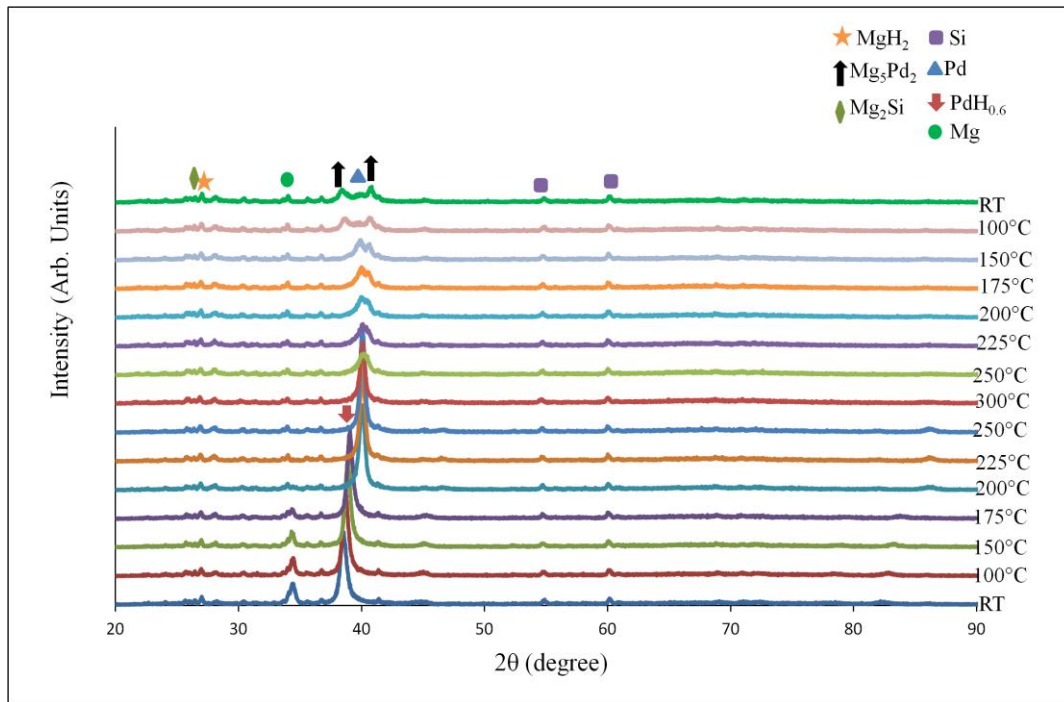


Fig 5.2.8 Sample (D) Pd(60nm)-Mg(150nm) silicon substrate heated at 3 bar  $H_2$  from room temperature to 300 °C (RT , 100 °C, 150 °C, 175 °C, 200 °C, 225 °C, 250 °C, 300 °C) then cooling down to room temperature. Every temperature step is 25 or 50 °C.

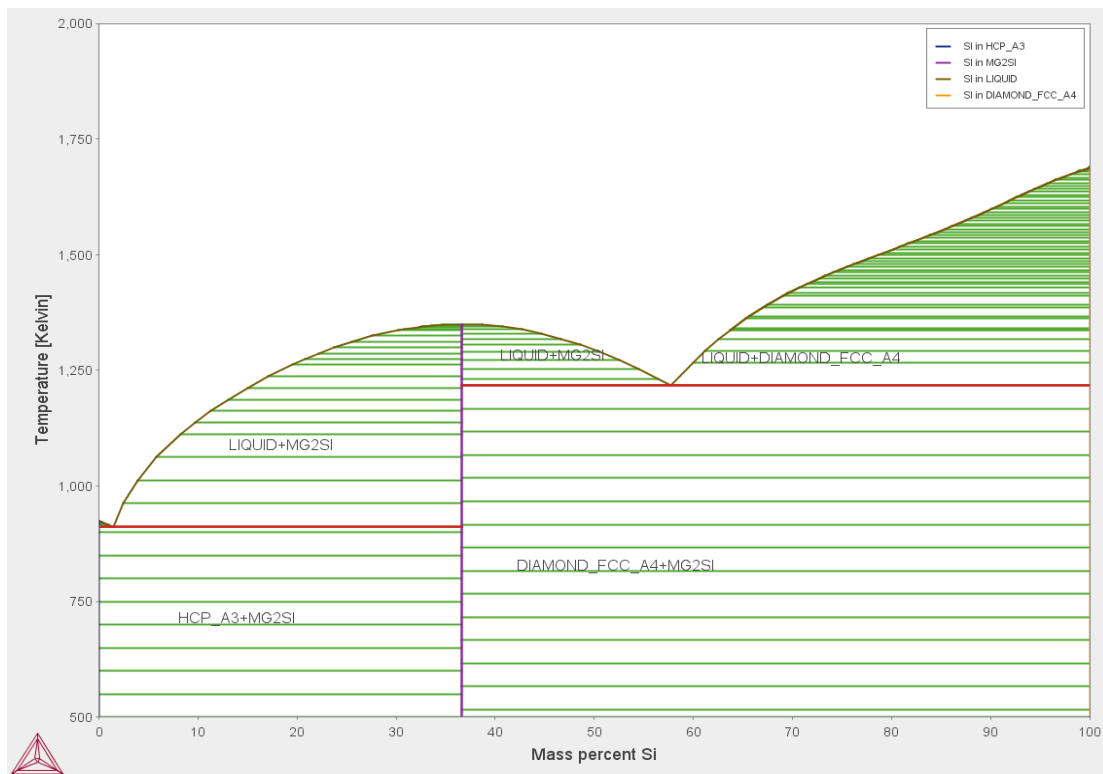


Fig 5.2.9 The Mg-Si binary phase diagram with x axis of mass percent Si and y axis of temperature Different phases can be observed.

#### 5.2.4 Conclusions

For the Mg thin films, the mechanisms of hydrogen storage were shown in XRD results. Pd top layer can alloy with Mg to form  $Mg_5Pd_2$  under He with temperature increase. Mg can react with  $H_2$  to form  $MgH_2$  in low temperature (below  $125\text{ }^\circ\text{C}$ ). Pd can react with  $H_2$  to form  $PdH_{0.6}$  and then dissociate at high temperature. If changing the glass substrate with Si substrate, alloying phase  $Mg_2Si$  will form after increasing temperature. In Fig 5.2.7, 5.2.8 and 5.2.9, the phase transformation was proved.

#### 5.3 Hydrogen sorption properties of Mg thin film

Under hydrogen absorption period, X-ray measurement at room temperature is shown in Fig 5.3.1. Sample Pd (60 nm)-Mg (800 nm) with glass substrate was hydrogenated in different time and then measured under the room temperature XRD. Mg peak around 35 degree which is reduced after hydrogenation. After 72 h hydrogenation, Mg peaks are disappeared.  $MgH_2$  peaks are observed after hydrogenated 48h. It shows that both Mg and  $MgH_2$  can be observed during hydrogenation time 24 h-48 h at room temperature.

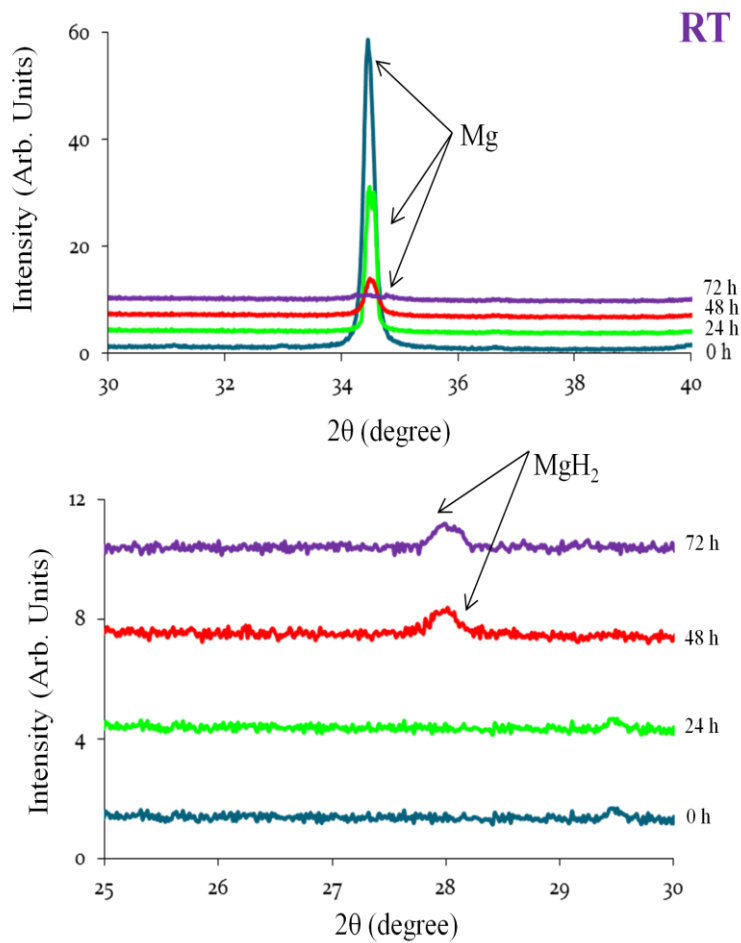


Fig 5.3.1 Sample Pd (60 nm)-Mg (800 nm) with glass substrate hydrogenated at 24 h, 48 h 72 h at room temperature and then measured the sample under X-ray sources.

Hydrogen sorption includes hydrogen absorption and hydrogen desorption process. Under hydrogen absorption period, all the samples Pd (60 nm)-Mg (800 nm) with glass substrate were hydrogenated at 100 °C. Then the X-ray measurement at room temperature is shown in Fig 5.3.2. Mg peak around 35 degree is reduced after hydrogenated. After 48 h, Mg peaks are disappeared.  $MgH_2$  peaks appear after hydrogenated 24 h at 100 °C. It shows that Mg peaks can be observed during 0h-48h and  $MgH_2$  peaks is observed during 24 h-72 h.  $MgH_2$  peak is around 28 degree.

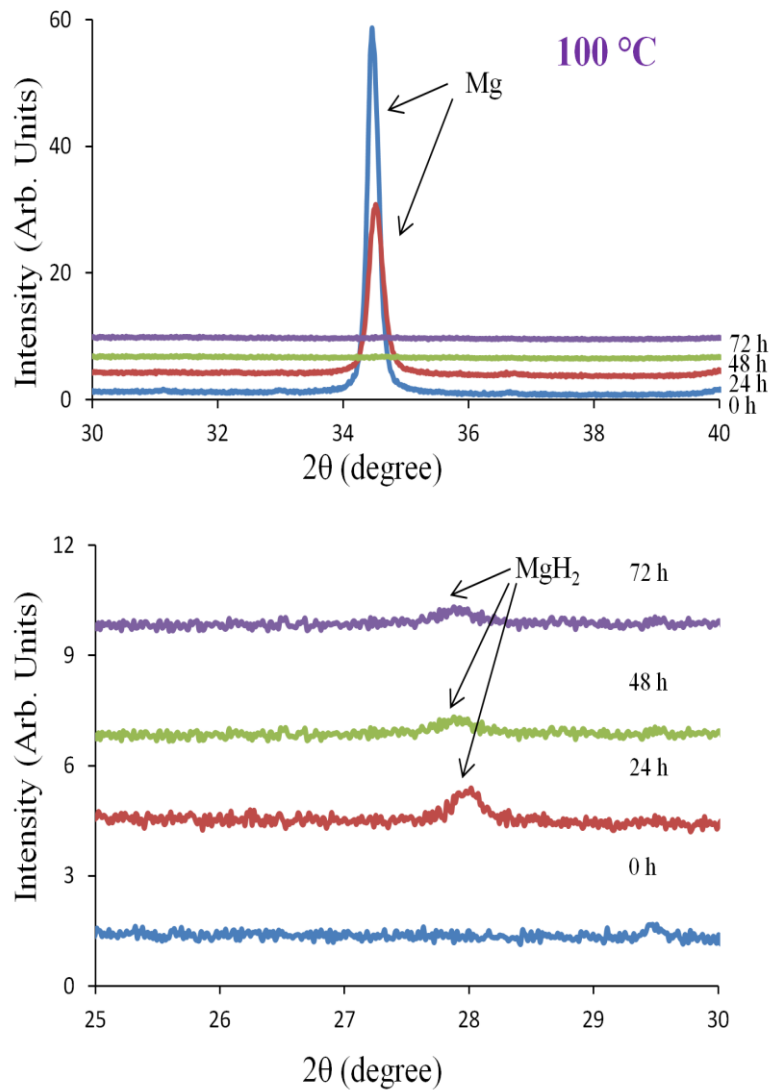


Fig 5.3.2 Sample Pd (60 nm)-Mg (800 nm) with glass substrate hydrogenated at 24 h, 48 h 72 h at 100 degree and then measured the sample under X-ray sources.

There is no accurate peaks of Pd(60 nm)-Mg(800 nm) thin film in Fig 5.8.1. The two broad peaks in the Fig 5.8.1 may be glass substrate. After hydrogenation 48 h of sample Pd(60 nm)-Mg(800 nm) thin film, two small peaks appear. The vibrational modes are  $1312\text{ cm}^{-1}$  and  $1448\text{ cm}^{-1}$  which may represent  $\alpha$ - $MgH_2$  peaks. In the paper, it shows the vibration mode of  $MgH_2$  peak is about  $312\text{ cm}^{-1}$ ,  $954\text{ cm}^{-1}$  and  $1279\text{ cm}^{-1}$ .

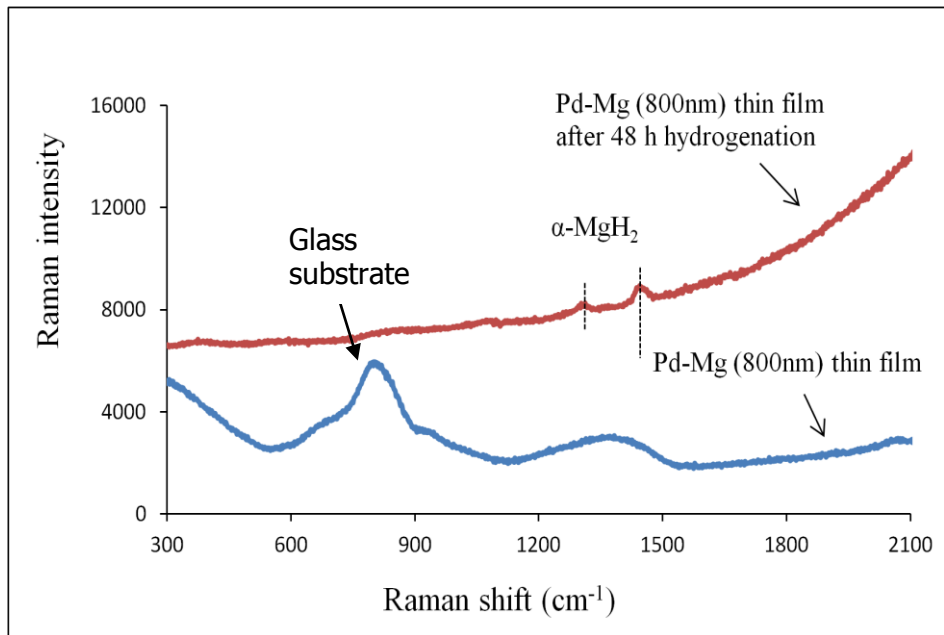


Fig 5.3.3 Raman intensity against Raman shift of sample Pd(60nm)-Mg(800nm) thin film and Pd(60 nm)-Mg(800 nm) thin film after 48 h room temperature hydrogenation process

As shown in Fig. 5.3.4, sample (A) without Ti interlayer, PdH<sub>0.6</sub> peaks are reduced in cooling process. It indicates that the alloying phase Pd<sub>5</sub>Mg<sub>2</sub> is formed and the Pd are not fully dissociated. By comparison, sample (C) with Ti interlayer, only PdH<sub>0.6</sub> phase is observed. It shows Ti interlayer can avoid the alloying between Mg and Pd. Sample (A) has clear Pd peaks from the temperature range of 225-300 °C. Sample (C) forms Pd from the temperature range of 200-300-150 °C. It means Pd phase exists with Ti interlayer in a wide temperature range. Pd has catalyst effect on hydrogen absorption rather than PdH<sub>0.6</sub> which will improve hydrogen absorption kinetics. Pd can enhance the dissociation of PdH<sub>0.6</sub>.

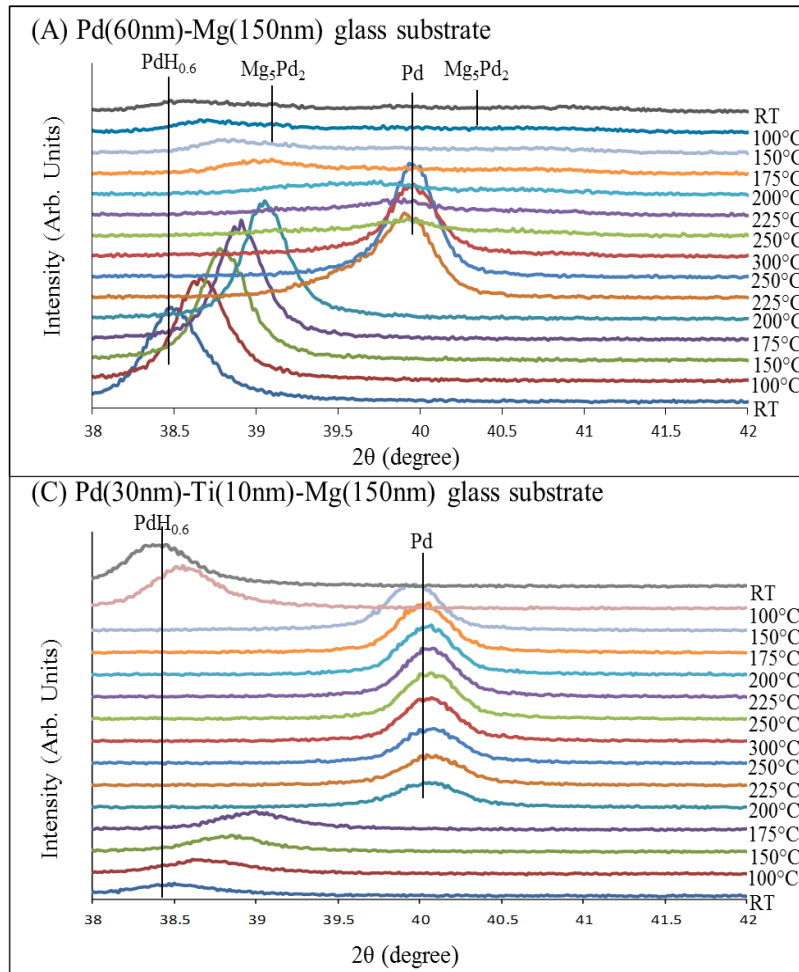


Fig. 5.3.4 In-situ XRD patterns of sample (A) Pd (60 nm)-Mg (150 nm) glass substrate and sample (C) Pd (30 nm)-Ti (10 nm)-Mg (150 nm) glass substrate under 3 bar  $H_2$  heating from room temperature to 300 °C and then cooling down to room temperature.

Sample (A) is Pd(60nm)-Mg(150nm) glass substrate. After inserting Ti interlayer, hydrogen absorption begins after 150 °C and finish at 200 °C. The temperature range is about 50 °C. Sample (A) absorbs hydrogen at room temperature and finishes at 150 °C. The kinetics of sample (C) is improved comparing with sample (A). However, sample (A) can absorb hydrogen at room temperature which the temperature is quite lower than sample (C). The possible reason is Ti thin layer reduction of hydrogen molecules absorbing. Besides, the results also show the kinetics change during inserting Ti interlayer. The hydrogen absorption temperature range is reduced which means the reaction time is shorten. Ti may act as the catalyst to improve the hydrogen sorption kinetics.

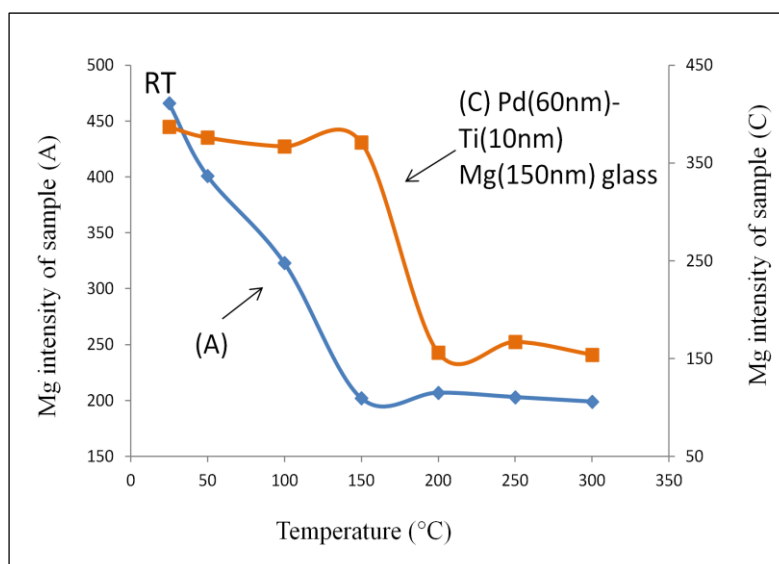


Fig. 5.3.5 Mg phase intensity against temperature change from room temperature to 300 °C of sample (A) and sample (C)

Based on in-situ XRD of Pd/Mg thin films, temperature against the Mg intensity was investigated as shown in Fig. 5.3.6. Mg intensity drop represents hydrogen absorption of Mg thin films. All samples are hydrogenated at 3 bar H<sub>2</sub> from RT to 300 °C. For sample (A), it is found that Mg began to react with hydrogen at room temperature. Sample (B), the hydrogen absorption temperature increases with the temperature range of 100-250 °C. The differences between sample (A) and (B) are Mg thickness and crystallinity. Thickness will influence hydrogen atoms diffusion pathway and crystallinity, which at last leads to thermodynamics properties change. Thick film with high crystallinity increases hydrogen absorption temperature. After changing the glass substrate to silicon substrate, hydrogen absorption started from 50-200 °C in sample (D). Si substrate increases the hydrogen absorption temperature range about 50 °C which further influence Mg thin films thermodynamics.

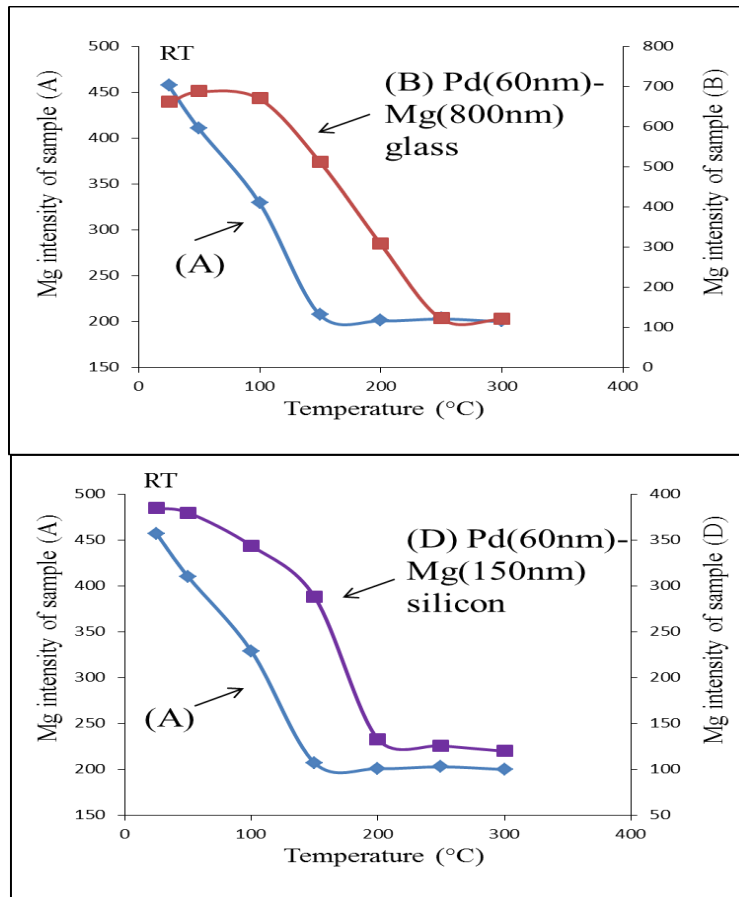


Fig. 5.3.6 Mg phase intensity against temperature change from room temperature to 300 °C of sample (A); sample (B) and sample (D)

By stress strain analysis, it was possible to plot kinetic points of peak intensity versus time as shown in the Fig 5.3.7. According to the intensity change, the reaction follows a diffusion-like mechanism. It is shown that the loading pressure is far above the plateau pressure. Around 150 min hydrogenation time, the Mg intensity percentage is similar with MgH<sub>2</sub> intensity percentage. The reaction of Mg and H<sub>2</sub> spend around 500 minutes in total.

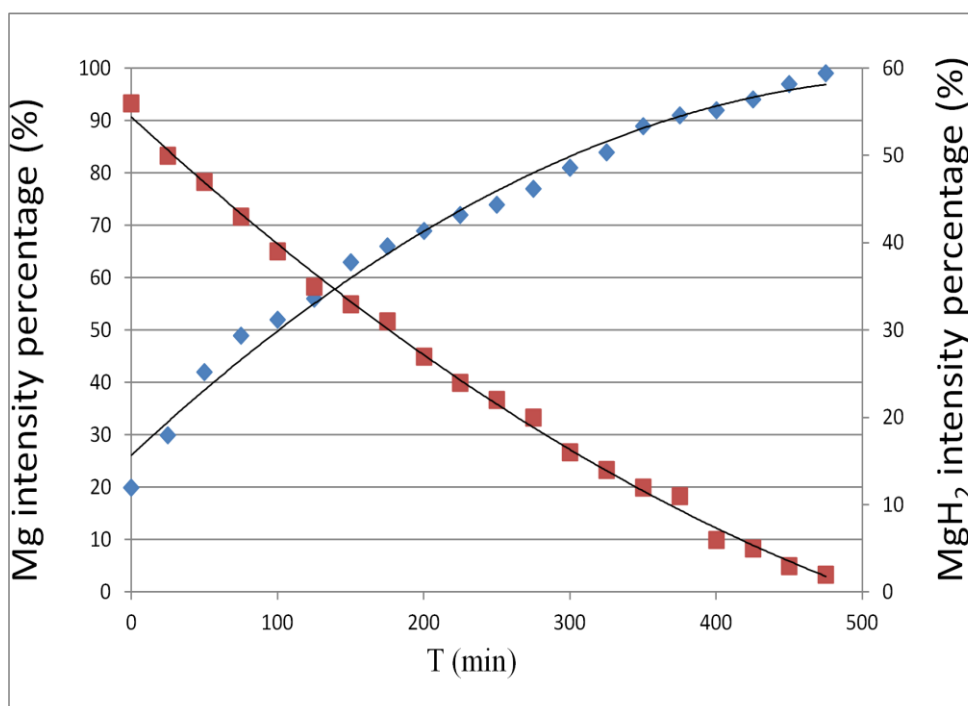


Fig 5.3.7 In-situ XRD peak intensity plot versus time. The reaction appears to be first order, showing that the factor is diffusion through the growing MgH<sub>2</sub> film. (Every scan took 25 minutes – total reaction time was about 8.3 hours 100 °C at 3 bar H<sub>2</sub>)

Sample (E) Pd(60 nm)-Mg(800 nm) glass substrate after 24h hydrogenation 100 °C 3bar pressure. Pd, Mg and MgH<sub>2</sub> peaks are shown in sample (E) Pd(60 nm)-Mg(800 nm) glass substrate after 24h hydrogenation 100 °C 3bar pressure. Then sample (E) was dehydrogenated under vacuum condition with different constant temperature. It use intensity ratio of Mg/Pd to represent dehydrogenation conditions change. After vacuum for 1 hour room temperature, Mg/Pd ratio is about 6 which is almost no change. After increases the temperature to 100 °C, the hydrogenation begins. After increasing the temperature to 200 °C and 250 °C, Mg/Pd ratio turns to around constant value of 13 which means that the sample (E) is fully dehydrogenated comparing to the other conditions. We use Mg/Pd ratio to represent the dehydrogenation conditions. MgH<sub>2</sub> peaks disappear above 200 °C as shown in Fig 5.3.7.

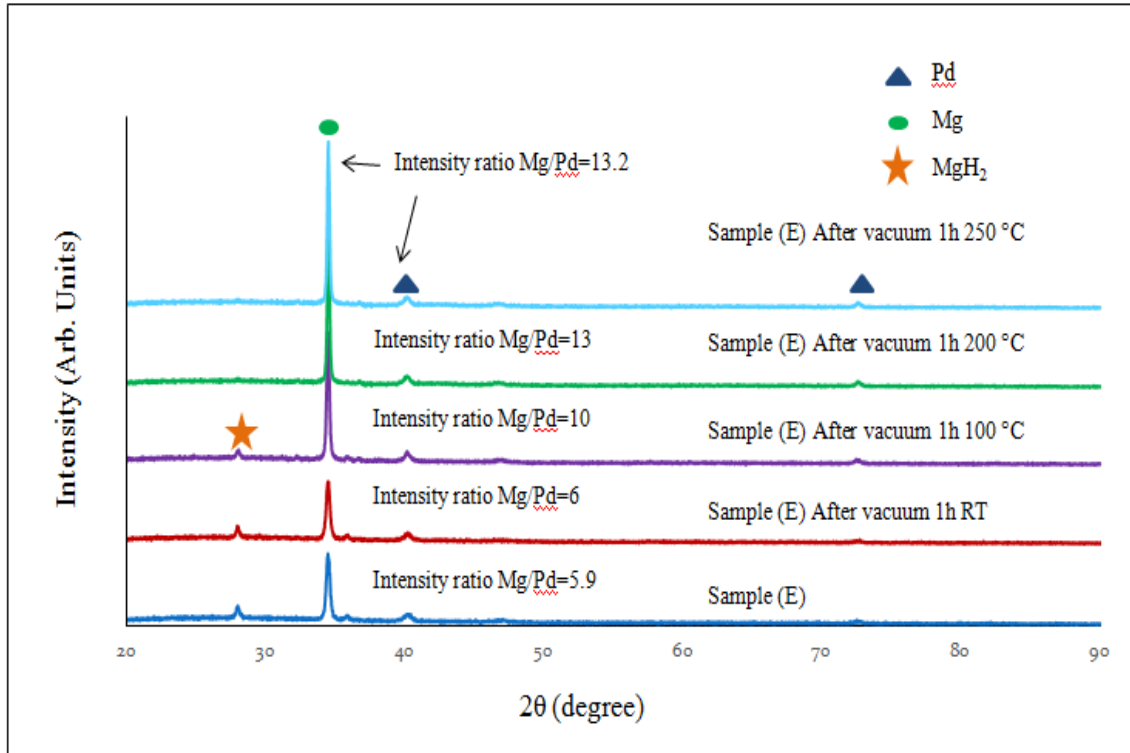


Fig 5.3.8 Sample (E) Pd(60 nm)-Mg(800 nm) glass substrate after 24h hydrogenation 100 °C 3 bar pressure. Different hydrogen desorption process of sample (E) under various vacuum conditions by changing the time and temperature

### 5.3.1 Conclusions

During hydrogen absorption and desorption process, sample Pd (60 nm)-Mg (800 nm) with glass substrate begin to react with H<sub>2</sub> after 24h 100 °C to form MgH<sub>2</sub> and fully dehydrogenate after vacuum 1h 200 °C. Higher temperature improves the hydrogen sorption kinetics which means easy to react with H<sub>2</sub> or release H<sub>2</sub>. Fig. 5.3.3 and Fig 5.3.4 shows the Raman and XRD results which proves the phase transformation of Mg thin films. In order to improve the hydrogen storage behaviors of thin films, Mg thickness was changed. Thinner Mg thickness has lower hydrogen absorption temperature. Besides, Ti interlayer and Si substrate were used. Ti interlayer can avoid the alloying between Mg and Pd which improves the hydrogen

absorption kinetics. Si substrate changes the thermodynamics of thin films. Hydrogen absorption temperature increases. Si substrate can reduce the weight and volume of Mg thin film. These results show how the Mg-based thin films behave during hydrogen sorption process which is used for hydrogen storage investigations.

#### 5.4 Thickness effect of Mg thin film

Thickness is measured by Profilometer. The error bar can be calculated below which is around  $\pm 10$  microns in Fig 5.4.1. The thickness value of Mg-based thin film should far above 10 microns due to the accuracy requirement. The scanning of Pd-Mg based thin film is useful for calibration by Profilometer technique. The error bar should be controlled in a small scale which is around 10 microns.

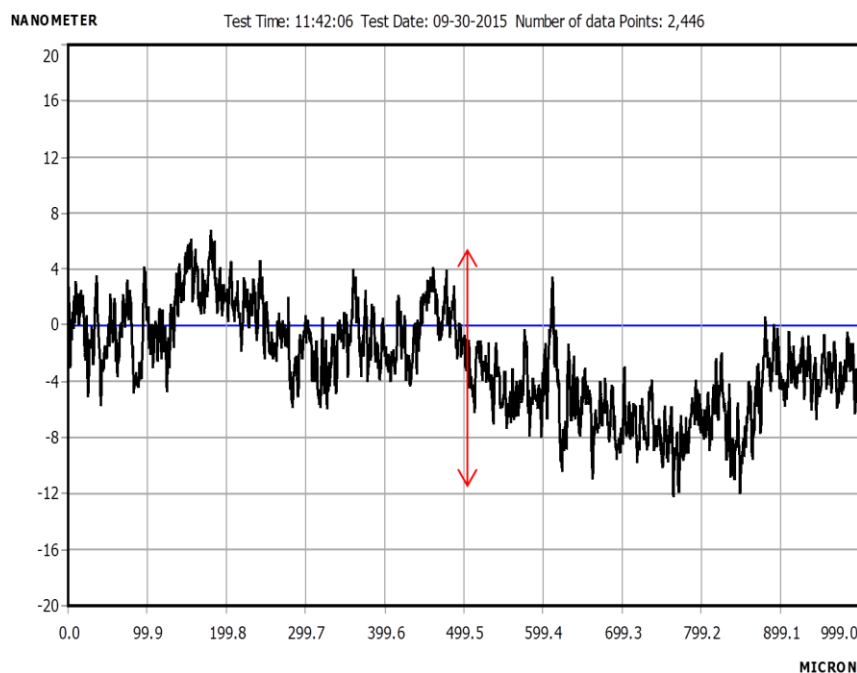


Fig 5.4.1 Profilometer measurement of sample which is placed on the disc at the beginning and then scanned about 5 cm's long. The error bar can be detected about  $\pm 10$  nm.

The thickness of sample Pd(30s)-Mg(1min), Pd(30s)-Mg(3min), Pd(30s)-Mg(5min) and Pd(30s)-Mg(20min) with glass substrate. As Mg sputtering time increases, thickness of thin

films increases. Based on the calculations, Pd sputtering speed is about 100 - 120 nm/min and the Mg sputtering speed is about 40 - 50 nm/min which is lower than Pd sputtering speed.

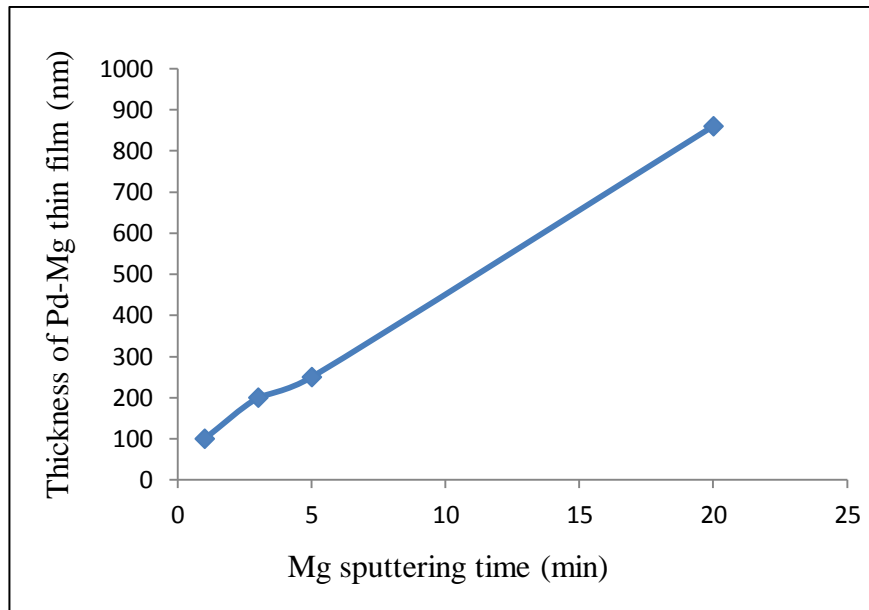


Fig 5.4.2 Thickness of Pd (30 s)-Mg (x min) thin films against different Mg sputtering time (min)

### 5.5 Interface shear stress linked with hydrogenation process

The Stoney equation is based on the thin film curvature. This method can be used in thin film system. But this equation has some assumptions which are important to recognize. The following assumptions are shown below:

1. Both the film thickness and substrate thickness should be uniform, have the same bend radius. Film thickness  $\ll$  substrate thickness  $\ll$  bending radius
2. Both the thin film and substrate are homogeneous, isotropic and linearly elastic.
3. The curvature of thin film system is equibiaxial (two equal direct curvatures). The twist curvature vanishes in all directions.

4. The film stress states are in-plane isotropic.
  5. The strains of plate systems are infinitesimal.
  6. All surviving stress and curvature components are constant on the plate system's surface.
- [71, 79, 80]

For these experiments, the Stoney equation is valid and useful. As the bending radius changes, the interface shear stress of thin films changes as well. The relationship between bending radius and interface shear stress is linear. The film in this case should be elastically connected to the substrate. At last, the Stoney equation is shown below [81]:

$$\sigma_f = \frac{E_s h_s^2 r}{6 h_f (1 - \nu_s)} \quad (21)$$

In Stoney equation,  $h_f$  represents uniform thickness of thin film and  $h_s$  indicate uniform thickness of substrate. The subscript f and s denote the thin film and substrate, respectively. E and  $\nu$  are the Young's modulus and Poisson's ratio respectively. This equation indicates the relationship between the radius of curvature of r and the interface shear stress of  $\sigma$ .

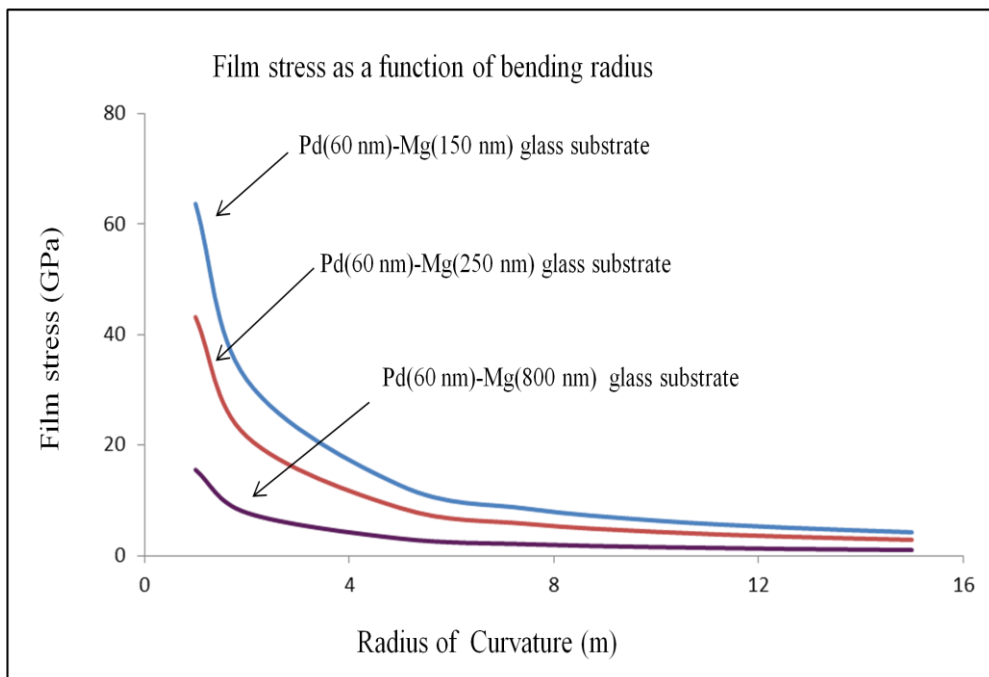


Fig 5.5.1 Film interface shear stress against radius of Curvature of samples Pd-Mg thin films glass substrate which is based on Stoney equation

As shown in Fig 5.5.2, interface shear stress decreases and curvature radius increases with increasing scan length. Increasing scan length can improve the accuracy. From 1 mm to 5 mm scan length can be measured. Thus we measure thin films stress based on 5 mm scan length with high accuracy.

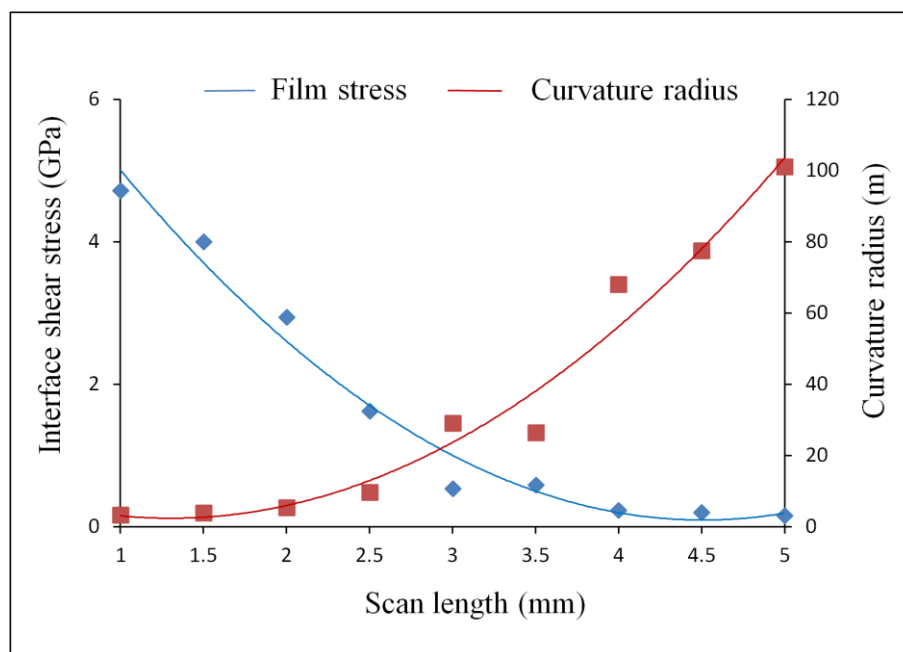


Fig 5.5.2 The interface shear stress and curvature radius against the scanning length of thin films. The scan length is from 1 mm to 5 mm.

As-sputtered samples were scanning through Profilometer. The interface shear stress can be measured as shown in Fig 5.5.3. Pd-Mg thin film with 50 nm Mg thickness has the lowest interface shear stress among these samples which is lower than 1000 MPa. Other Pd-Mg thin films' interface shear stress is around 1000 MPa. Pd(60nm) thin film without coating Mg layer has highest interface shear stress among them.

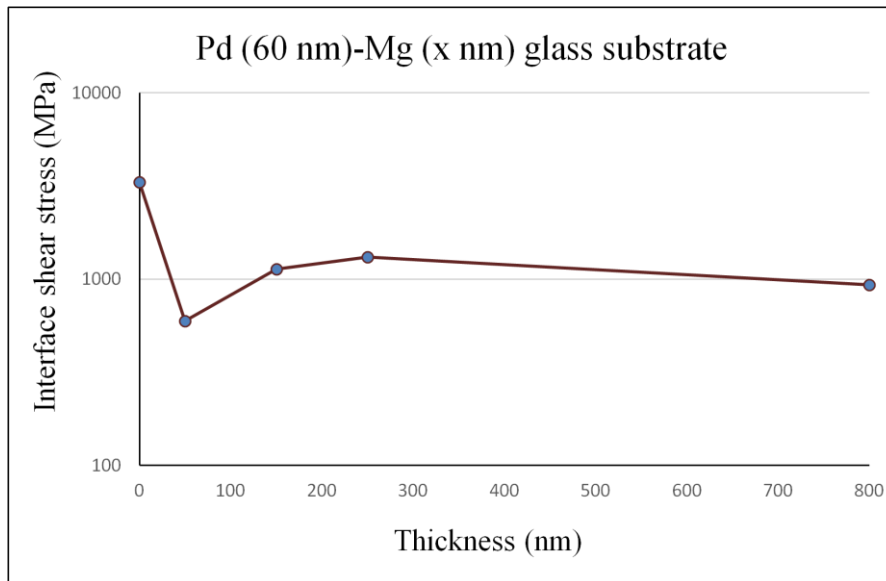


Fig 5.5.3 Interface shear stress of sample Pd-Mg thin film with different Mg thickness

In Fig.5.5.4 and Fig.5.5.5, the connection between interface shear stress and hydrogenation properties is built. In Fig. 5.5.4, under room temperature, sample (A) Pd(60 nm)-Mg(150 nm) glass substrate and (D) Pd(60 nm)-Mg(150 nm) silicon substrate interface shear stress is measured every 24 h after hydrogenation. Sample (D) interface shear stress is lower than 1 GPa within 72 h. Sample (A) interface shear stress is higher than 1 GPa (around 1.5 GPa) after 72 h. Comparing sample (A) and (D), silicon substrate has lower shear stress level. Comparing sample (A) and (B), thicker Mg film has lower interface shear stress level. Each sample is cut to five parts for hydrogenation. The error bar is made by five different regions of the samples' detection which is around 500 MPa. The data dot is the mean value of five different regions' value. The error bar shows the scale of measured samples. As hydrogenation time increases, the interface shear stress increases.

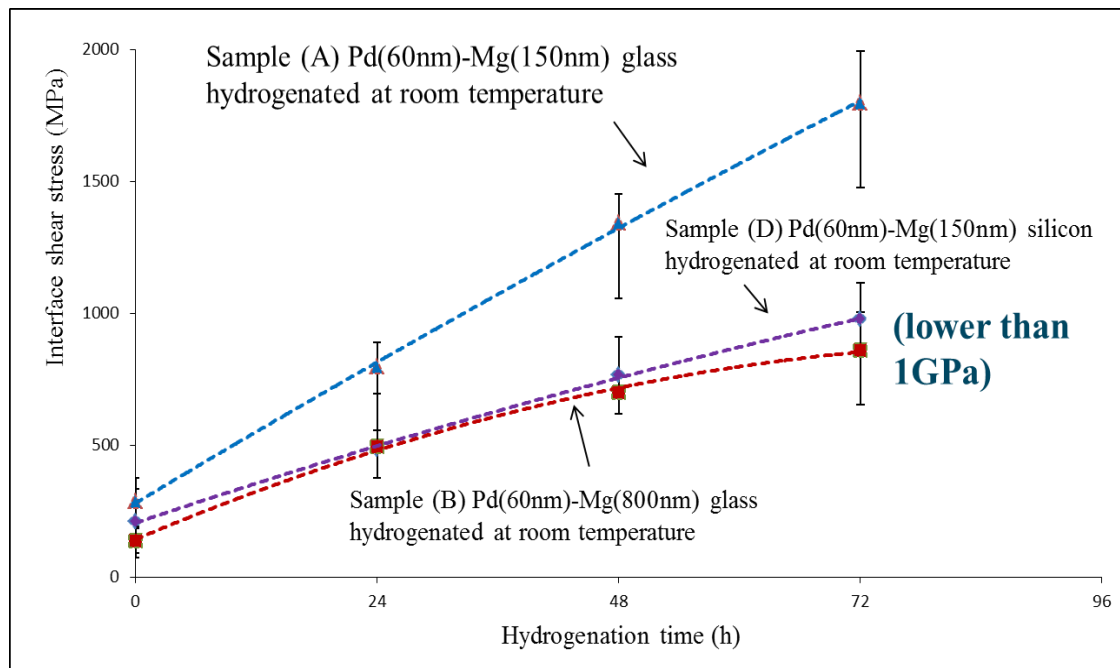


Fig 5.5.4 Hydrogenation time against the interface shear stress of sample (A), sample (B) and sample (D) at room temperature 3 bar pressure. The scanning speed is 1mm/s and the scan length is about 5 mm. The error bar is measured by the various regions of the sample (A), (B) and (D).

As shown in Fig 5.5.5, sample (B) Pd(60 nm)-Mg(800 nm) glass substrate shear stress is measured every 24 h after hydrogenation. At room temperature, the interface shear stress is lower than 1 GPa after 72 h hydrogenation. Shear stress increases with increasing hydrogenation time which matches Stoney equation well. At 100 °C, shear stress is above 1 GPa after 48 h hydrogenation. Temperature has a big effect on interface shear stress because of the thermal expansion. Interface shear stress accumulates due to the increase of temperature. The error bar indicates the scale of interface shear stress which is measured by five regions' value. In the same sample if you scan in different regions the value has slightly changed.

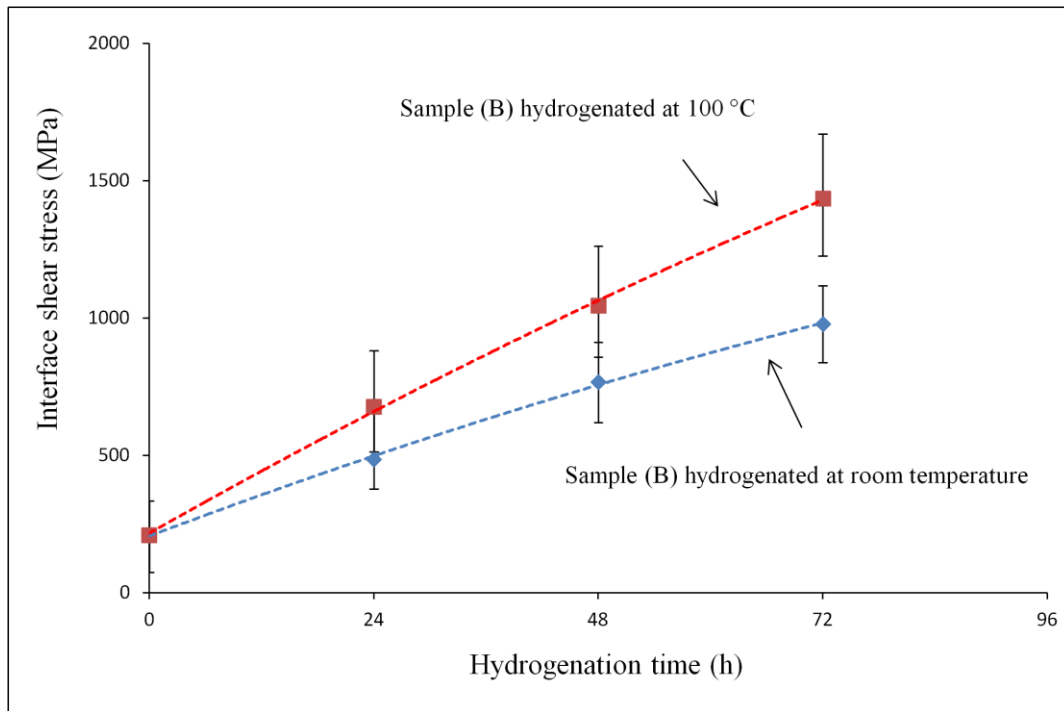


Fig 5.5.5 Hydrogenation time against the interface shear stress of sample (B) Pd(60 nm)-Mg(800 nm) glass substrate at room temperature and 100 °C under 3 bar pressure. The scanning speed is 1mm/s and the scan length is 5 mm in total. The error bar is measured by the various regions of the sample (B).

### 5.5.1 Conclusions

The interface shear stress is around 1 GPa after hydrogenation which match the value of the buckling stress estimated by XRD. With the hydrogenation time increases, interface shear stress increases linearly. When temperature change and Mg thickness change, interface shear stress varies. High temperature causes the thermal expansion and hydrogenation time accumulates high compressive stress which leads to higher interface shear stress. During the experiment, scan speed has almost no influence while scan length has influenced a lot. Larger scan length can reduce the shear stress which increases the accuracy. The scan length should be far above the bending radius. In experiment, the scan length is chosen as 5 mm. After

increasing the scan length the interface shear stress becomes lower which indicates more accurate results.

#### 5.6 Surface roughness and buckling appearance of Mg thin film

Both the surface roughness and buckling appearance are measured by Profilometer. For the buckling measurement, the cross section is chosen as 0.5 x 0.5 mm region. The scan speed is 0.05 mm/s. There are 100 times scanning on the surface in total. The buckling appearance and surface roughness can be measured by Confocal and Profilometer techniques. When the region has buckling, the surface is also rougher than other regions. Thus buckling appearance has relevant effect with film surface roughness.

As shown in Fig 5.6.1, surface roughness change slightly with different Mg layer thickness. The surface roughness value is measured by Profilometer. The surface roughness is around 0.1  $\mu\text{m}$ . Pd (60nm)-Mg (50nm) glass substrate has the lowest surface roughness among all these samples which is about 0.05  $\mu\text{m}$ . The error bar is lower than 0.1  $\mu\text{m}$ . The error bar is made by different parts of the samples. Different region has slightly changed surface roughness. The data capacity is five different regions.

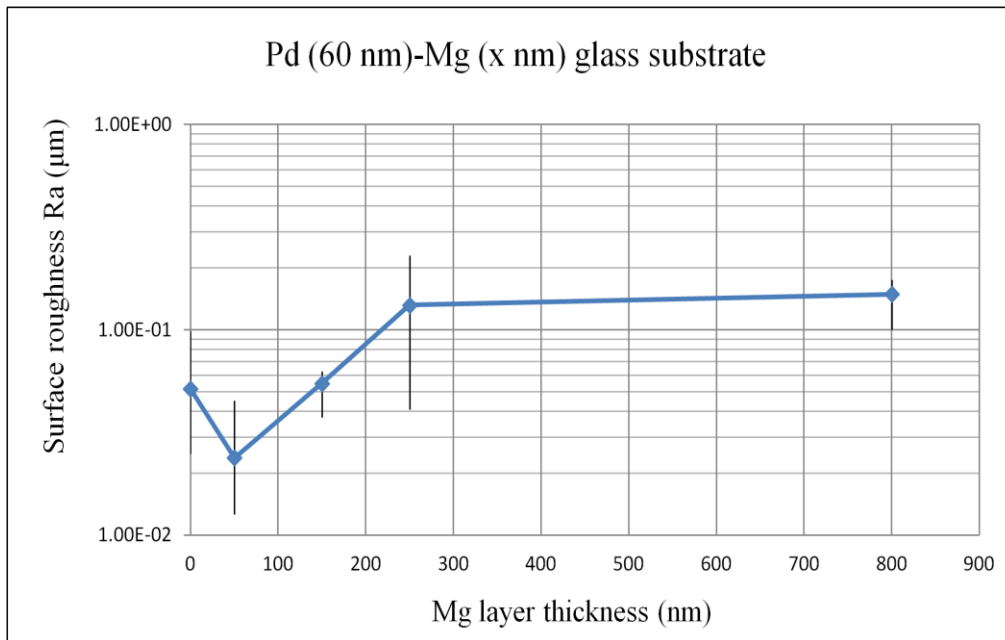


Fig 5.6.1 surface roughness of sample Pd(60 nm)-Mg(x nm) glass substrate with different Mg thickness. The error bar is made by various regions' detection.

Confocal microscopy provides the results of samples' microstructure. Confocal images are shown below in Fig 5.6.2. Pd(60 nm)-Mg(50 nm) has the smoothest surface among three samples with different Mg thickness. There are some scratches in Confocal images which may be due to oxidation of samples. Black region forms which may due to the stress build up.

(10 x magnification)

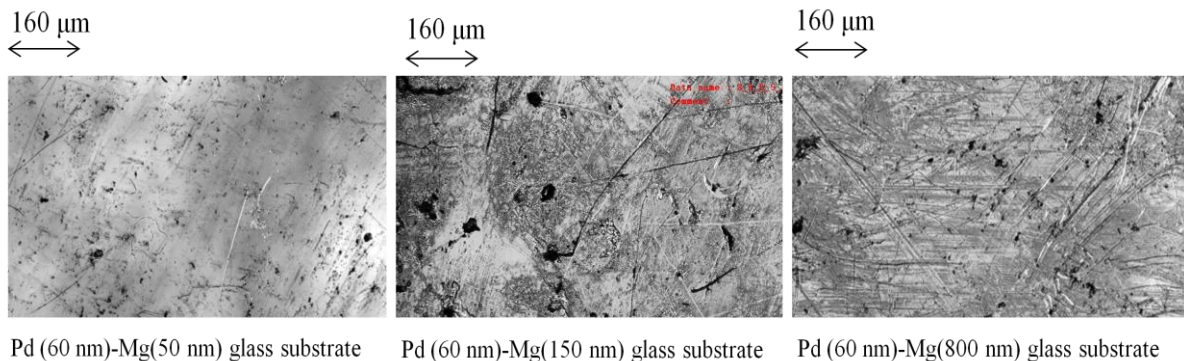


Fig 5.6.2 10 x magnification by Confocal microscopy of as-sputtered sample Pd(60 nm)-Mg(50 nm), Pd(60 nm)-Mg(150 nm) and Pd(60 nm)-Mg(800 nm) with glass substrate

As shown below, sample Pd(60 nm)-Mg(800 nm) with glass substrate after hydrogenation were measured through Confocal microscopy. At 72 h 3bar H<sub>2</sub> room temperature hydrogenation conditions, the surface becomes rougher than as-sputtered materials. The black zones seem to be buckling. Under 72 h 3bar H<sub>2</sub> 100 °C hydrogenation conditions, the buckling region is huge. The surface become rougher than the sample hydrogenated under room temperature.

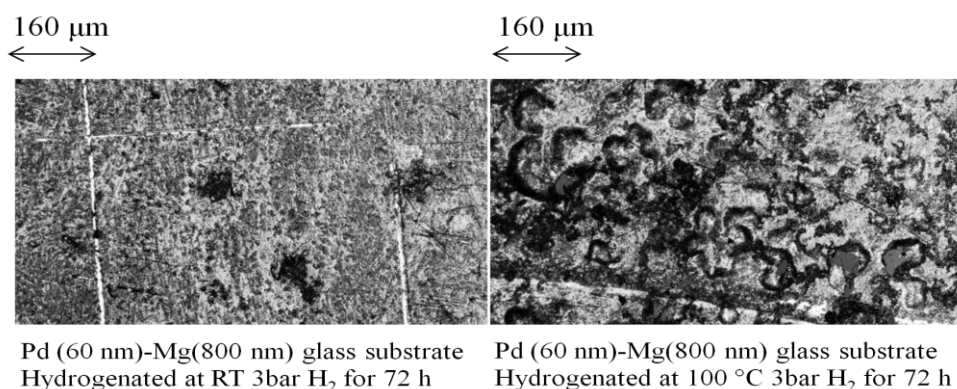


Fig 5.6.3 10 x magnification by Confocal microscopy of sample Pd(60 nm)-Mg(800 nm) glass substrate hydrogenated at room temperature 3 bar H<sub>2</sub> 72h and Pd(60 nm)-Mg(800 nm) glass substrate hydrogenated at 100 °C 3 bar H<sub>2</sub> 72h.

Confocal images of samples with different substrate are shown below. Sample sputtered on MgO substrate has smoothest surface roughness with no buckling present. It is shown that MgO remains smooth on the surface which can induce a sorption behavior dominated by plasticity due to higher adhesion force. Sample deposited on glass substrate has few buckling with smooth surface. Among three samples, sample deposited on silicon substrate has rough surface with many buckling as shown in Fig 5.6.4. It seems to have de-lamination of the film from the substrate. The black zone shows off the stretches and buckling. The adhesion energy of different substrate is quite different. Besides, buckling can influence the adhesion energy. More buckling, the thin film was easy to peel off.

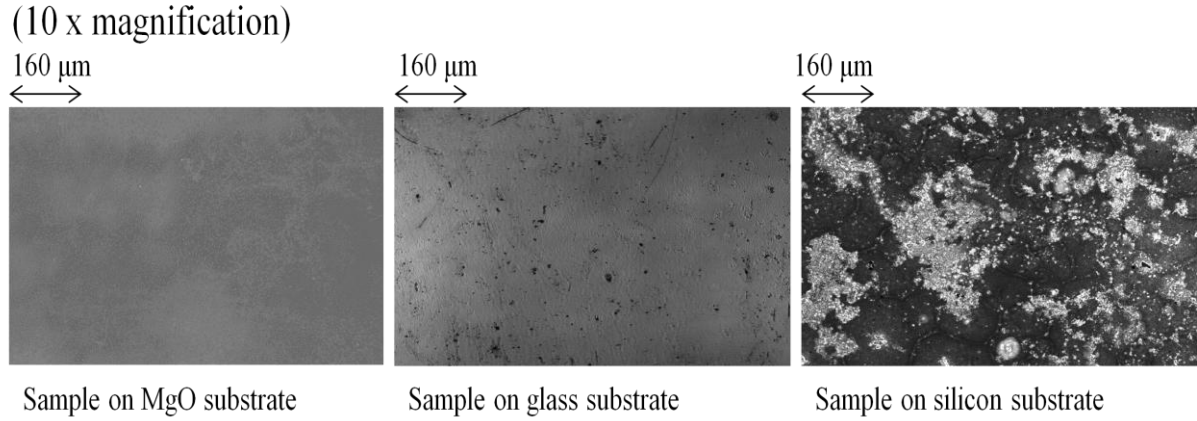


Fig 5.6.4 10 x magnification by Confocal microscopy of sample Pd-Mg with MgO substrate, sample Pd-Mg with glass substrate and sample Pd-Mg deposited on silicon substrate

The buckling appearance is observed by Profilometer technique. The surface condition is shown in Fig 5.6.5. In Fig 5.6.5, different color represents various surface roughness. Red color means the largest surface roughness which seems to be buckling. The scanning region is 0.5 mm x 0.5 mm in sample (a) and (b). Scan speed is about 0.05 mm/s. Pd(60nm)-Mg(800nm) glass substrate hydrogenated 72 h room temperature 3 bar  $\text{H}_2$  has only one buckling. While under 100  $^\circ\text{C}$ , sample (b) has about five buckling region. More scratches can be found in sample (b). The surface color represents different surface conditions. It shows that higher temperature leads to rougher surface. High temperature causes the volume expansion which can accumulate high stress.

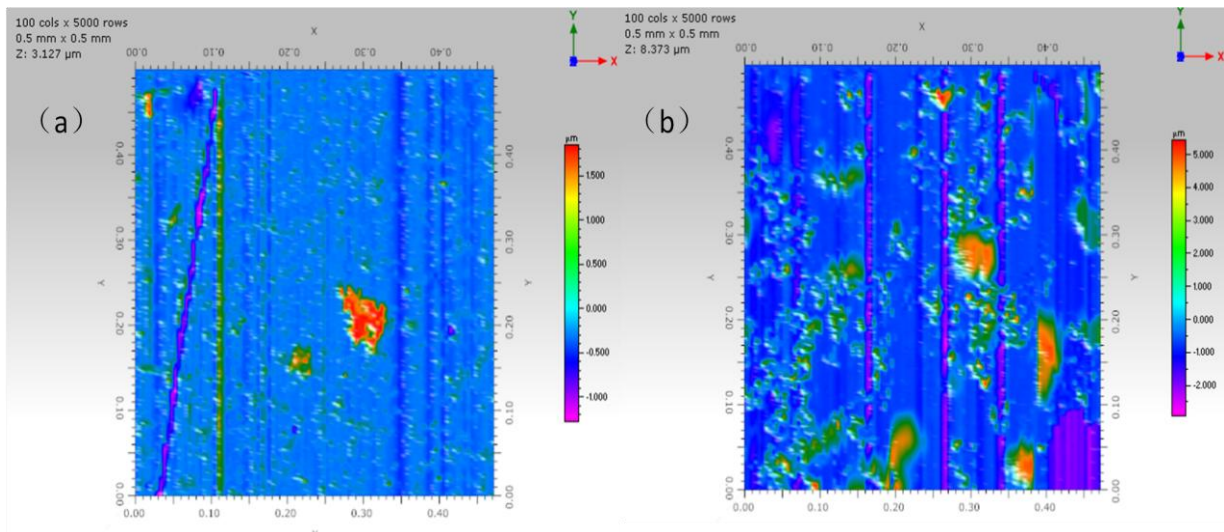


Fig 5.6.5 buckling appearance observed by Profilometer of sample (a) Pd(60nm)-Mg(800nm) glass substrate hydrogenated for 72 h at room temperature 3 bar H<sub>2</sub> (b) Pd(60nm)-Mg(800nm) glass substrate hydrogenated for 72 h at 100 °C 3 bar H<sub>2</sub>

The buckling appearance is measured through Profilometer technique. The surface condition is shown in Fig 5.6.6. In Fig 5.6.6, different color represents different surface roughness. Red color means the largest surface roughness which seems to be buckling. Blue color shows about the smooth surface. The region is 0.5 mm x 0.5 mm in sample (c) and (d). Scan speed is about 0.05 mm/s. Pd(60nm)-Mg(150nm) glass substrate hydrogenated 24 h 100 °C 3bar H<sub>2</sub> has two buckling. While at 100 °C, sample (d) has only one buckling region. More scratches can be found in sample (c). It shows that thinner film has more buckling region after heating up. Among sample (a) to sample (d), hydrogenation time and temperature are the two parameters to influence the number of buckling.

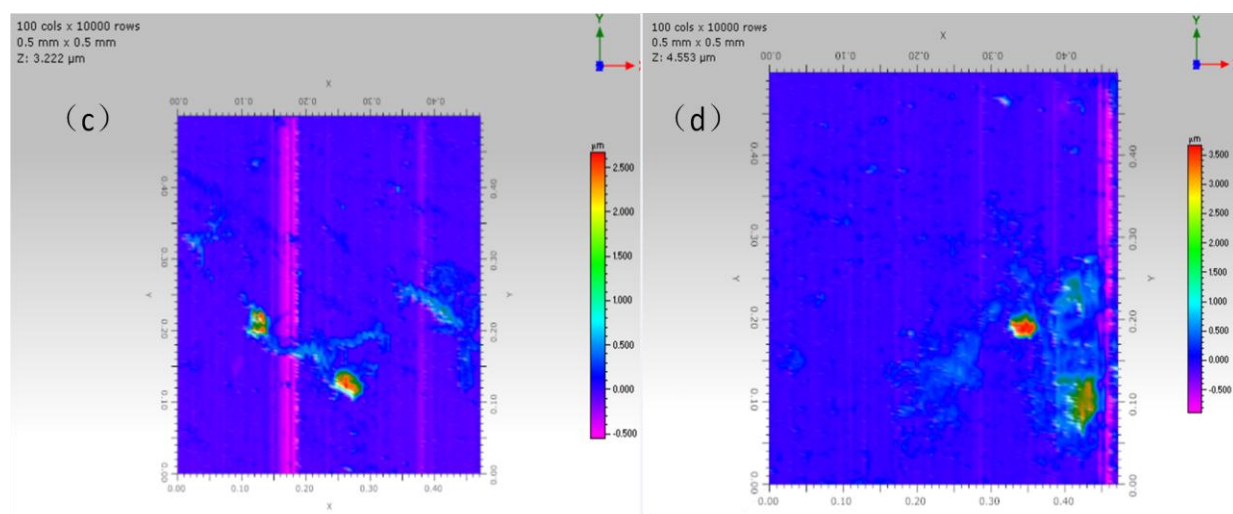


Fig 5.6.6 buckling appearance observed by Profilometer of sample (c) Pd(60nm)-Mg (150nm) glass substrate under 24 h 100 °C 3bar H<sub>2</sub> (d) Pd(60nm)-Mg (250nm) glass substrate under 24 h 100 °C 3 bar H<sub>2</sub>

Surface roughness of sample Pd(60 nm)-Mg(800 nm) glass substrate is measured as shown in Fig 5.6.7. The samples are hydrogenated 24 h, 48 h, 72 h and 96 h. At room temperature,

surface roughness increases with the increasing of hydrogenation time. The surface roughness is below 0.5  $\mu\text{m}$  after 96h hydrogenation. At 100  $^{\circ}\text{C}$ , The surface roughness is about 1 $\mu\text{m}$  after 96h hydrogenation. Higher temperature has higher surface roughness due to the thermal expansion comparing with the sample hydrogenated at lower temperature. Surface roughness and interface shear stress both increasing with the hydrogenation time as shown in Fig 5.5.5 and Fig 5.6.7. The results show that the surface roughness has positive correlation with the interface shear stress of the Mg thin films. More buckling can lead to rougher surface of thin film. The buckling forms due to the stress accumulation. Thus higher stress also leads to rougher surface of the Mg-based thin films.

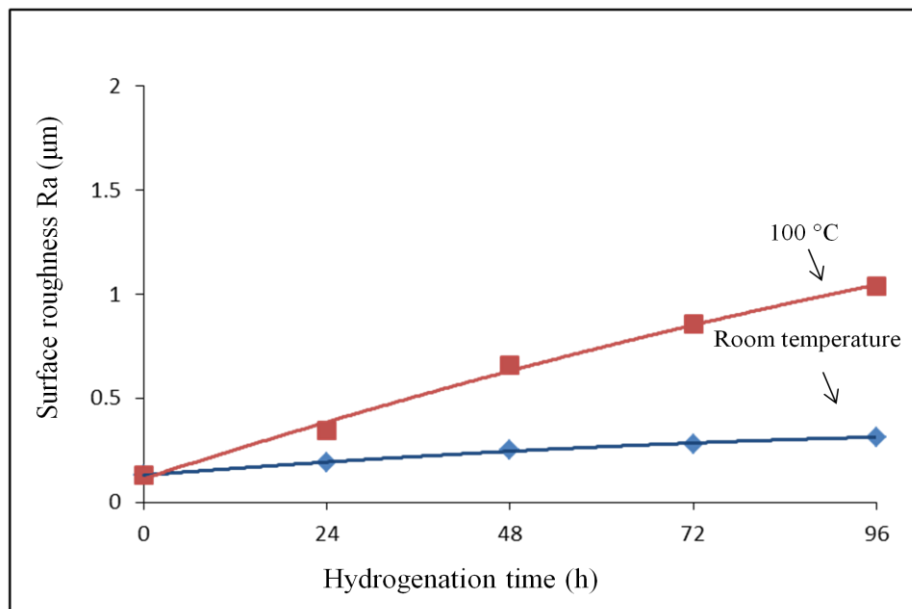


Fig 5.6.7 Surface roughness Ra value of sample Pd(60nm)-Mg(800nm) glass substrate against hydrogenation time (0 h, 24 h, 48 h, 72 h, 96 h) at room temperature and 100  $^{\circ}\text{C}$  respectively

### 5.6.1 Conclusions

From the surface roughness results, during hydrogen sorption process, stress accumulates at the surface which also easily leads to buckling appearance. The buckling number increases

with the accumulation of stress. More bulking number appears after hydrogen absorption. Hydrogenation time and temperature increase lead to more bulking which means surface becomes rougher than before. Stress accumulates and bulking appears to release stress. The surface roughness increases linearly with the hydrogenation time. Higher hydrogen absorption temperature leads higher surface roughness value. After temperature increases, surface become rough which surface coalescence forms due to the thermal expansion of temperature increase. The relationship between surface roughness and hydrogenation behavior can be built from the experiment which can be useful for hydrogen sensors applications.

## 5.7 Mg based multilayers

Mg based multilayer such as Mg/Y was investigated as below. The alloying effect between Mg and Y metals can be measured. Multilayer is different system with thin layer system. Transition metal such as Y can be chosen to improve kinetics.

Mg/Y multilayers were sputtered with the Pd cap layer which is about 60 nm. Different Mg/Y multilayers were made with various Y thickness range from 10 nm – 40 nm. The schematic drawing of the film is shown below in Fig 5.7.1. The total thickness is controlled which is about 860 nm including 800 nm Mg/Y layer and 60 nm Pd top layer. The multilayer construction is shown below.

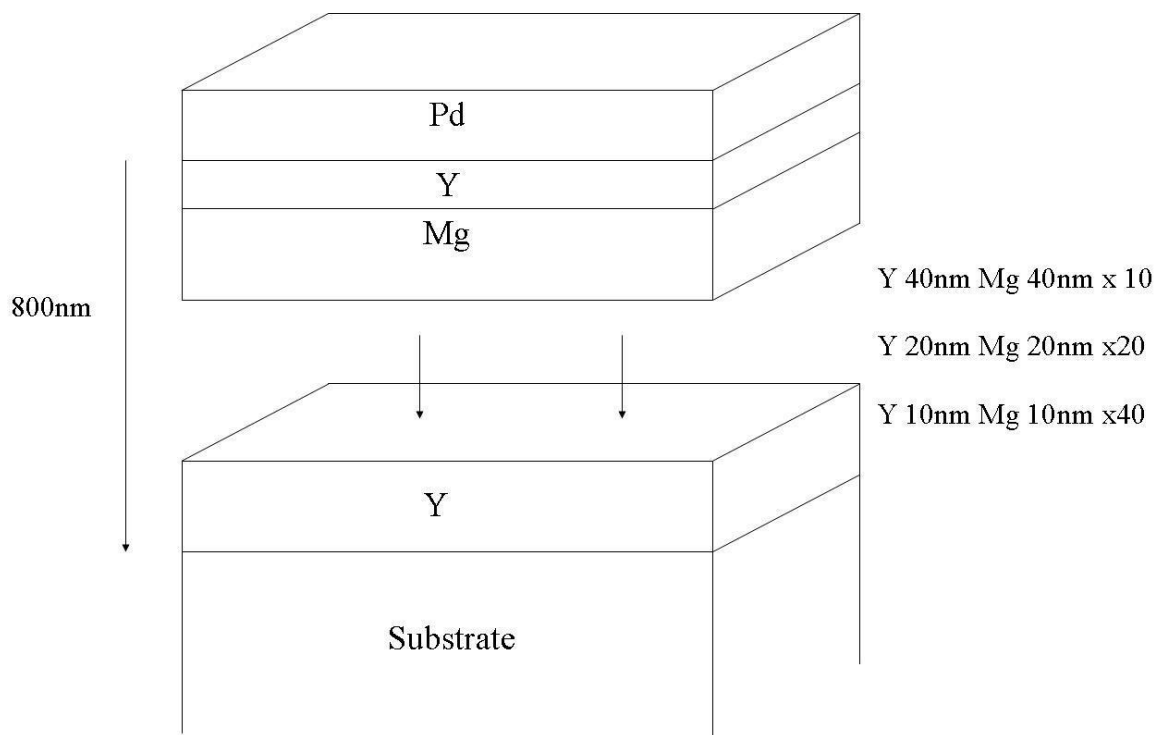


Fig 5.7.1 Schematic drawing of the Pd-Mg-Y films with Y and Mg layers of varying thicknesses and number of layers. The total thickness was about 800 nm.

The films were shown in Fig5.7.2 which was analyzed by XRD. Some interesting features are observed. At first Pd, Mg and Y peaks are observed. Then the lattice parameter of the Mg/Y multilayer is calculated which is shown in table 5.7.4. The Pd close packed (111) plane can be observed with high intensity which is due to the 60 nm thickness of Pd top layer. For Mg layer, three multilayers structures have the same total thickness of Mg, but the intensity of Mg varies. There doesn't seem to be a recognizable pattern to the intensities as the thickness decreases. Mg is shown to be FCC structure. There are many small peaks of sample Pd(60 nm)-Mg(40 nm)-Y(40 nm), which shows the structure of FCC and HCP Y. Both the Mg and Y peaks shift among these three samples. The peaks shift which indicated that the lattice parameter changes. There is no alloying phase observed in Fig 5.7.2.

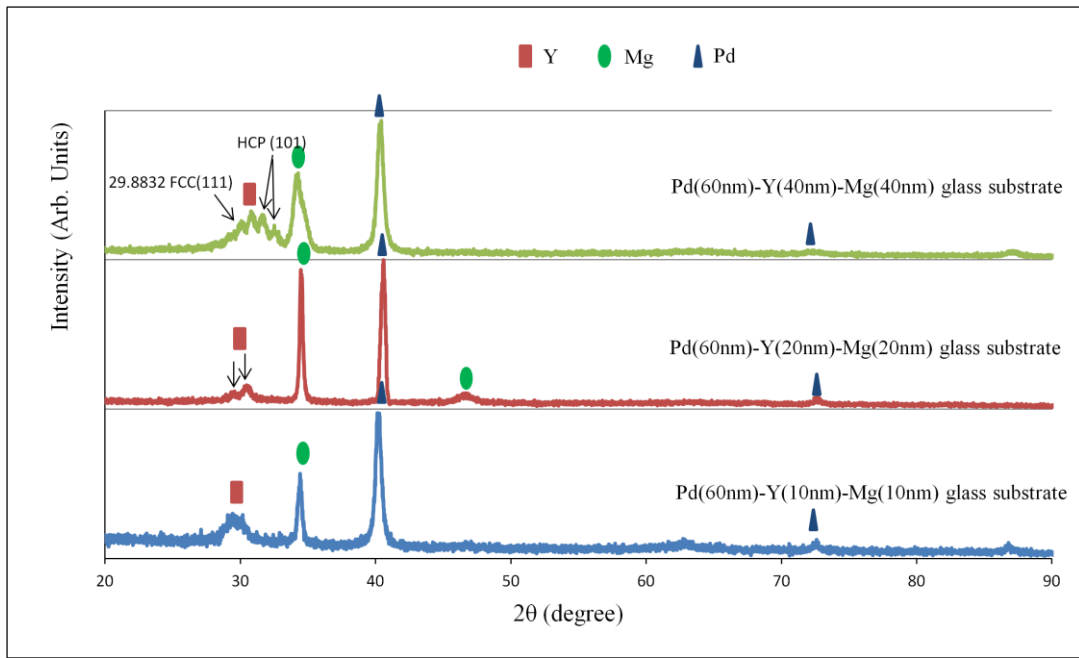


Fig. 5.7.2 The XRD detection of Mg/Y multilayers at room temperature

After hydrogenated sample Pd(60 nm)-Y(40 nm)-Mg(40 nm) glass substrate at 3 bar 250 °C for 24 h, FCC (111) Y and Pd can be observed clearly. Y lattice parameter changes from HCP to FCC due to the temperature increases. Lattice expands with the increasing of temperature. MgH<sub>2</sub> has the similar peak position with Y as shown in Fig 5.7.3. In Table 5.7.4, all the lattice parameter values are shown through Topas software. The value of lattice parameter is around 5.

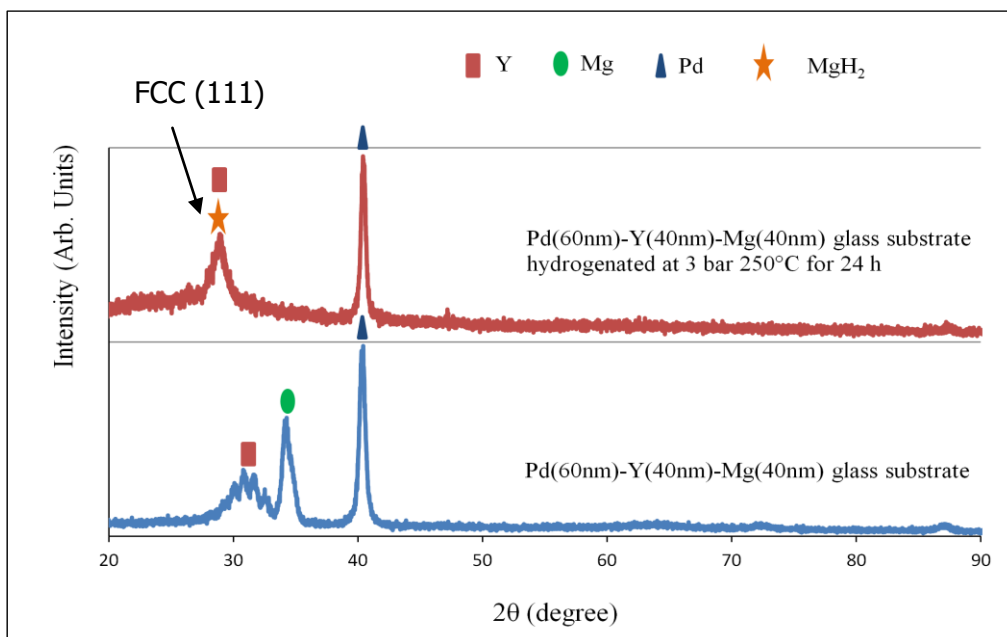


Fig 5.7.3 XRD detection of sample Pd(60nm)-Y(40nm)-Mg(40nm) glass substrate hydrogenated at 3 bar 250 °C for 24 h

Table 5.7.4 The lattice parameter of as-sputtered Mg/Y multilayers

	HCP - Y		FCC – Y	Mg – C axis
	c	a	a	c
Mg/Y (40 nm)	5.768	3.735	n/a	5.211
Mg/Y (20 nm)	5.753	3.705	5.04	5.195
Mg/Y (10 nm)	5.811	3.634	5.16	5.241

Sample Pd(60 s)-Y(40 s)-Mg(40 s) multilayer was heated from room temperature and then cooling down to room temperature under He atmosphere. Mg, Y and Pd phase was observed clearly. There is no alloying phase formation between Y and Mg. Y layer can also reduce the alloying formation between the Mg and Pd. The Mg, Y and Pd peaks position stay the same. The lattice parameter value stays constant as well. Multilayer structures provide a new method to store hydrogen.

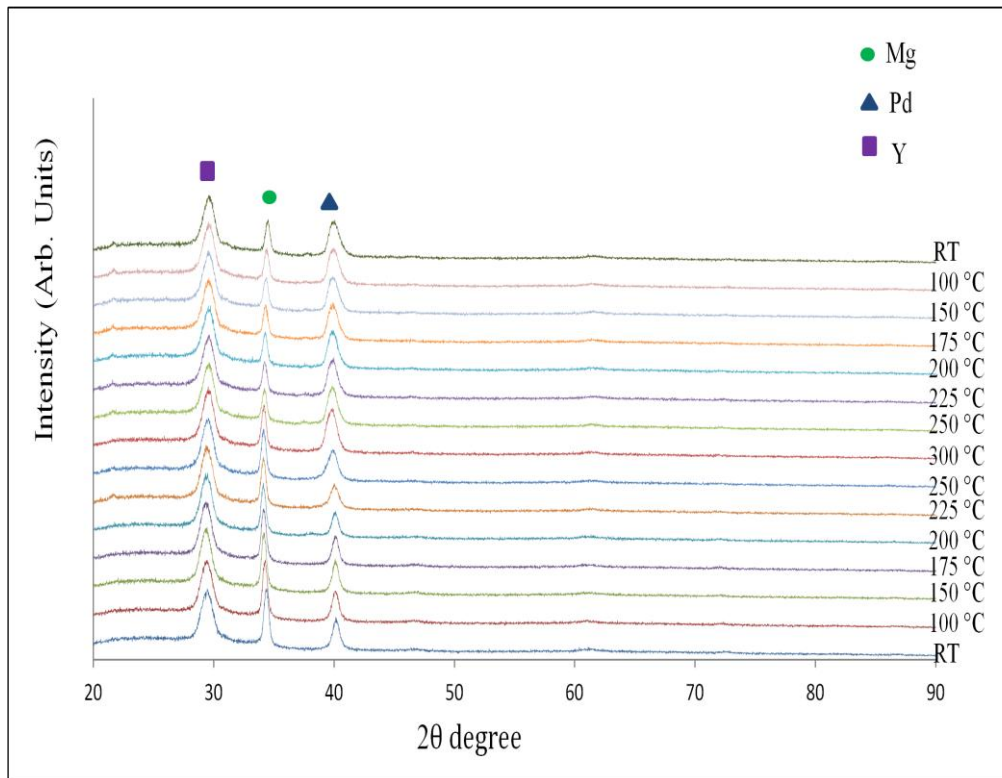


Fig 5.7.5 Sample Pd(60 s)-Y(40 s)-Mg(40 s) (5 layers) multilayer under 3bar He heating from room temperature to 300 °C and then cooling down from 300 °C to room temperature.

## 5.8 Sheet resistivity of Mg based thin films

### 5.8.1 Two probe technique

Table 5.8.1 two probe sheet resistivity data from sample (a) to sample (e)

Sample ID	R1	R2	R3	R4	R5	R(mean)
(a) 1 A 25 sccm	4.6 Ω	4.5 Ω	4.7 Ω	5.3 Ω	3.6 Ω	4.5 Ω
(b) 1 A 35 sccm	4.4 Ω	4.6 Ω	5.6 Ω	6.1 Ω	3.5 Ω	4.8 Ω
(c) 1 A 45 sccm	2.8 Ω	3.3 Ω	3.6 Ω	2.7 Ω	3.8 Ω	3.2 Ω
(d) 0.6 A 25 sccm	9.9 Ω	7.6 Ω	9.8 Ω	10.3 Ω	8.4 Ω	9.2 Ω
(e) 2 A 25 sccm	2.7 Ω	1.6 Ω	2.2 Ω	1.9 Ω	2.4 Ω	2.2 Ω

The results show that lower current has higher sheet resistivity. The mean resistivity of sample (d) is about 9.2 Ω which is highest among all the samples. Lower current may have

bad random orientation which increases the resistivity. Comparing with the bias current, base pressure has less effect on sheet resistivity.

### 5.8.2 Four probe technique

Table 5.8.2 four probe sheet resistivity data from sample (a) to sample (e)

Sample ID	R1	R2	R3	R4	R5	R(mean)
(a) 1 A 25 sccm	3.7 $\Omega$	3.8 $\Omega$	4.1 $\Omega$	4.4 $\Omega$	3.5 $\Omega$	3.9 $\Omega$
(b) 1 A 35 sccm	4.1 $\Omega$	4.3 $\Omega$	4.7 $\Omega$	5.1 $\Omega$	3.3 $\Omega$	4.3 $\Omega$
(c) 1 A 45 sccm	2.8 $\Omega$	3.0 $\Omega$	3.6 $\Omega$	2.3 $\Omega$	3.2 $\Omega$	3.0 $\Omega$
(d) 0.6 A 25 sccm	7.4 $\Omega$	7.1 $\Omega$	6.8 $\Omega$	8.1 $\Omega$	8.0 $\Omega$	7.5 $\Omega$
(e) 2 A 25 sccm	2.0 $\Omega$	1.2 $\Omega$	2.2 $\Omega$	1.4 $\Omega$	1.7 $\Omega$	1.7 $\Omega$

The results show that lower current has higher sheet resistivity. The mean resistivity of sample (d) is about 7.5  $\Omega$  which is highest among all the samples. Lower current may have bad random orientation which increases the resistivity. Comparing with the bias current, base pressure has less effect on sheet resistivity. Four probe resistivity measurements has lower value than two probe measurement due to the accuracy of contact resistivity.

### 5.9 Optical behaviors

The transmittance against wavelength of sample Pd (30 nm) glass substrate is shown in Fig 5.9.1. The transmittance has a big drop when the wavelength is around 300 nm and there is a second transmittance drop when the wavelength is around 500 nm. Above 600 nm, the transmittance increases with the increasing of wavelength. At the 400 nm wavelength, there is a sudden increase of transmittance which may be due to the Pd thickness influence.

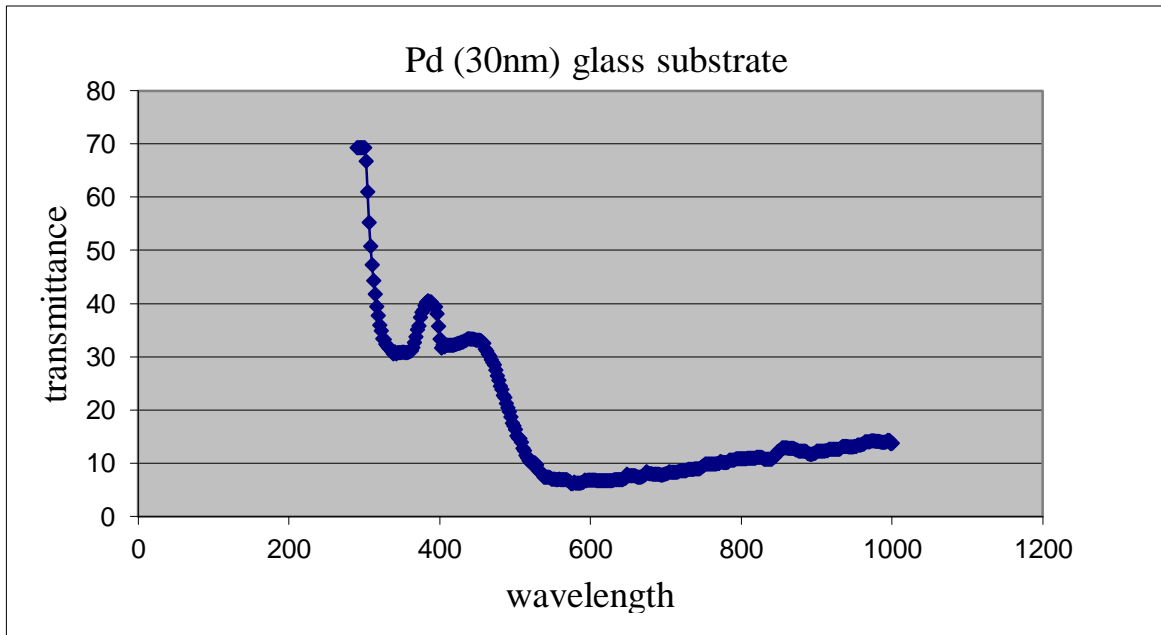


Fig 5.9.1 Optical behaviors of Pd (30 nm) glass substrate is shown. The relationship is between transmittance and wavelength.

### 5.9.1 Conclusions

In table 5.8.1, 5.8.2 and Figure 5.9.1, only basic experiment is doing. Sheet resistivity and optical transmittance are the specific physical properties of thin films which could be influenced during hydrogenation process. Due to some reasons, I did not continue to do it. But I think if we can build the relationship between these two thin films' physical properties and hydrogenation behaviors, it is meaning for hydrogen sensor investigations. Hydrogen sensors can be tools which can indicate hydrogen change.

## 6. Conclusions

### 6.1 General discussion

In this chapter, the results will be discussed. The results are including thin film microstructure, the interface shear stress, surface roughness, ex-situ and in-situ XRD measurements and so on. The Mg films were deposited on the glass substrate in different conditions using CFUBMSIP system which leads to various crystallinity, microstructure and intrinsic stress. All the results are shown in a simple and correct way. These results provide a complete picture of Mg based thin films. Based on these results, the general discussions are shown below:

Bias current and argon flow rate are the two main sputtering parameters which can be controlled by sputtering machine. Bias current provides large driving force on crystallinity through influencing the Mg lattice parameter. Higher bias current leads to higher value of lattice parameters. Besides, higher Ar flow rate leads to thicker and denser films through changing the base pressure as shown in Table 5.1.3. Deposition conditions influence intrinsic stress as well. The features in Fig 5.1.4 show the microstructure with porosities. Grain size increasing provides the reduction of stress which means grain growth reduces stress.

Mg-Pd thin films will form alloying phase  $Mg_5Pd_2$  above 250 °C under He atmosphere based on the Mg/Pd binary phase diagram. The alloying phase formation will reduce the hydrogen capacity because part of Mg alloys. On the  $H_2$  atmosphere, Pd hydrogenated first to form  $PdH_{0.6}$  at room temperature and then dehydrogenated at around 175 °C to 200 °C.  $MgH_2$  begins to form at around 125 °C. Alloying phase  $Mg_5Pd_2$  is still existence but less obvious. Hydrogenation reaction is superior comparing with alloying reaction. XRD results indicate the mechanisms of Mg thin film hydrogenation. In order to improve the Mg thin film hydrogen storage properties, Ti interlayer and Si substrate were used. Based on Fig 5.3.4 and

Fig 5.3.5, Ti interlayer is confirmed to avoid the alloying and improve kinetics because no alloying phase formation after hydrogenation and hydrogenation time is shortened. Comparing with glass substrate, Si substrate reduce the substrate weight and volume while improves the hydrogenation temperature.

Pd(60 nm)-Mg(50 nm) glass substrate has the lowest surface roughness value and interface shear stress among samples under different Mg thickness. Lower surface roughness means smoother surface. Less stress accumulates provides less sketches and buckling on the surface which will reduce the surface roughness due to the surface morphology. Buckling can release stress while the film layer will peel off with high buckling numbers.

Hydrogenation time and temperature are the two parameters to influence the interface shear stress of the thin films. High temperature and long hydrogenation time leads to more buckling which increases the interface shear stress. High temperature causes the thermal expansion and hydrogenation time increases high compressive stress which improves interface shear stress. Scan length and scan speed are two important factors which influence the calculation of the interface shear stress. Higher shear stress level leads to more buckles during hydrogen absorption which will require less driving force for the thin film peeling off. It means less energy can be absorbed to overcome the energy barrier caused by stress accumulation between Mg layer and substrate. Interface stress of thin film is related with thermodynamics issue. There will be a driving force for the atoms adsorption. [82] Thus the absorption temperature of Mg thin film is reduced by thinner Mg films.

Mg/Y multilayers are detected by XRD. Y acts as the transition metal which influence the kinetics. Various thickness of Y will influence the lattice parameter of Mg-Y thin films. There is no alloying phase formation between Y and Mg under high temperature He atmosphere. In Mg/Y multilayer, it is potential that the interfacing layers cause the

thermodynamics change. In the future, different Y thickness can be measured to indicate the influence on hydrogen sorption temperature.

## 6.2 Final conclusions

These results are discussed and well considered which map the project aims. In these results, the conclusions are corrected and accumulated which is shown below:

The grain size of Mg based thin films is measured through Scherrer equation based on XRD. Mg grain size is about 100 nm which is estimated by Jade software. When using SEM, the grain size is measured around 250 nm. Thus it is confirmed the actual grain size is nano-size. Besides, intrinsic stress reduces with the grain size increasing which indicates grain growth provides stress reduction.

In order to find the effects on Mg thin film hydrogen sorption properties, Ti interlayer, Si substrate and various Mg thicknesses were used. Ti interlayer can avoid the alloying formation between Mg and Pd which will improve the Mg thin film hydrogen capacity. The reaction kinetic is improved. Si substrate influences the thermodynamics which increases hydrogen absorption temperature around 50 °C. Mg thickness increasing leads to the hydrogen absorption temperature reduction. Thinner film has lower absorption temperature which is good. But thinner Mg film has lower theoretical maximum hydrogen capacity which should be considered. Mg/Y multilayer systems were investigated as well. The characterization of these Mg/Y samples shows that HCP / FCC yttrium occurs at different layer thicknesses, changing the lattice spacing at coherent interfaces with Mg. This shows another potential route to the hydrogen sorption process. These results are relevant with Mg thin film hydrogen storage.

The intrinsic stress is controlled and changed by various sputtering conditions (bias voltage and current). The value of intrinsic stress is similar with the interface shear stress which is around 1 GPa. After hydrogenation at room temperature, the value of interface shear stress is below 1 GPa. At 100 °C, the interface shear stress is around 1 GPa after hydrogenation 48 h. The link between Mg hydrogen absorption behaviors and interface shear stress is built. At the same time, higher interface shear stress has more buckling numbers of the surface. The surface becomes rougher than before. Higher stress needs less driving force to form buckling. If the buckling number reaches a constant value that the film will peel off from the substrate.

The surface roughness is increasing due to the temperature increase and increase of hydrogenation time. Meanwhile, high surface roughness also has more buckling number measured by Profilometer. At room temperature, the value of surface roughness is far below 1  $\mu\text{m}$ . At 100 °C, the value of surface roughness is around 1  $\mu\text{m}$  after hydrogenation 72 hours. On room temperature, the roughness increases slowly with a small change. At 100 °C, surface roughness increases fast and linear with hydrogenation time. High temperature accumulates more stress to form buckling which increases the surface roughness.

At last, the Mg thin films sheet resistivity and optical transmittance properties are investigated but not finished. The results are basic which are in the beginning of research. Interface shear stress, surface roughness, sheet resistivity and optical transmittance are all the Mg thin films' physical properties. These properties are influenced by hydrogen sorption factors such as hydrogen temperature, hydrogenation time and hydrogen capacity. The relationship between them could be built which are useful for hydrogen sensors applications.

### 6.3 Future work

Based on experimental work, there are still some jobs need to be well considered. Some work is partially finished and some is not. Future work is discussed. This would help to make a

more complete thin film picture in this chapter. The thesis demonstrates thin film hydrogen sorption properties for hydrogen storage investigations and physical properties of thin film for further hydrogen sensors investigations. In the future, more hydrogen storage properties especially hydrogen sorption capacity of Mg-based thin films will be achieved. More physical properties of Mg thin films relevant with hydrogen sensors will be discussed.

More detailed microscopy including cross section regions should be measured by TEM instead of SEM. TEM can provide higher resolution which will give a better picture than SEM. The microstructure will be magnified by TEM. TEM could be used to observe the hydride phase of a growing film in applied stress conditions. After hydrogenation, phase change should be measured by TEM in the future. Besides, as for the Pd-Ti-Mg thin film, TEM results can help us to know how to avoid alloying with Ti interlayer. For thin film, we can also make the connection between Mg column width and hydrogen behavior such as hydrogen capacity and sorption temperature.

Various and flexible substrate will be used for Mg based thin films. Different substrate will have different volume and weight which can influence the hydrogen capacity. Both hydrogenation and dehydrogenation properties such as temperature and pressure are discussed through hydrogen chamber and RGA technique. The hydrogen capacities are measured which may be better than glass substrate. Changing the substrate can help thin films to meet the target of hydrogen capacity. Both kinetics and thermodynamics properties will discuss and measure through XRD and RGA techniques. During MPhil study, RGA equipment is broken for a long time which should be carried out in the future. Without RGA, only maximum hydrogen capacity can be estimated.

In the future, sheet resistivity can be measured by both two probe technique and four probe techniques. The relationship among hydrogenation temperature, hydrogenation time and sheet resistivity will be discussed. According to the sheet resistivity change, hydrogen

sorption conditions can be estimated. Build the relationship between sheet resistivity and hydrogenation behavior. This ability of thin films could be a promising use for hydrogen sensor applications.

When regarding to multilayers, the lattice mismatch between layers can be an effective route for destabilization of hydrides. The work for Mg/Y multilayer is discussed. Both HCP and FCC phases are included. Further research using in situ methods would be more useful here, as it would show the phases of yttrium hydrides. How the transition metal will influence the samples are discussed. At the same time, with the work of multilayer, in-situ XRD under He and H<sub>2</sub> atmosphere can be detected to find the alloying phase between transition metal Y and Mg. How the transition metal such as Y influence the kinetics of Mg based thin films. Various thickness of Y may have different effects. Alloying phase between Mg and Y will be investigated. At the same time, the hydrogen sorption temperature and capacity will be achieved. Then we will know how Mg/Y multilayer thin film behaves comparing with Pd/Mg thin film.

In the hydrogenation process, temperature and hydrogenation time will influence the surface roughness and interface shear stress. Buckling will appear in the surface and buckling number will be calculated in 0.5 x 0.5 mm regions. Thus, buckling number may be used to estimate the hydrogenation process and conditions. Besides, the interface shear stress of thin films can make the relationship with the buckling number and surface roughness in the future.

Optical behaviors can be measured by optical UV laser. Transparent features are changing due to the Mg thickness and Mg microstructure. Mg thickness can be controlled by sputtering time and Mg microstructure can be controlled by sputtering parameter such as bias voltage and base pressure. The relationship between optical transmittance and hydrogen conditions such as different temperature will be estimated. The results are useful to know various thin films samples' optical behaviors which are better for hydrogen sensors investigations.

## List of Publications

### Poster Presentations

Effect of a Ti interlayer on hydrogen sorption behavior of Mg thin films

Yuan, C., Nayebossadri, S., Book, D.

H<sub>2</sub>FC SUERGEN conference in Bath 2016

Hydrogen sorption behavior of magnesium thin films

Yuan, C., Nayebossadri, S., Book, D.

H<sub>2</sub>FC SUERGEN conference in Birmingham 2015

Hydrogen sorption behavior of magnesium thin films

Yuan, C., Nayebossadri, S., Book, D.

H<sub>2</sub>FC SUERGEN conference in Birmingham 2014

### Oral Presentations

Hydrogen absorption properties of Mg-based thin films

Yuan, C., Nayebossadri, S., Book, D.

H<sub>2</sub>FC SUERGEN conference in University of St Andrews 2017

Hydrogen absorption properties of Mg-based thin films

Yuan, C., Nayebossadri, S., Book, D.

H<sub>2</sub>FC SUERGEN conference in Belfast 2016

### Paper publications

Investigations on hydrogen absorption properties of Mg-based thin films

## References

1. China-hydrogen org <http://www.china-hydrogen.org/> assessed (22/09/2017)
2. Lucas, R. E. *Lectures on Economic Growth*. (Harvard UP, 2002).
3. McLamb, E. The ecological impact of the industrial revolution. at <http://www.ecology.com/2011/09/18/ecological-impact-industrial-revolution/> accessed (22/09/2017)
4. I.P. Jain, C. Lal, A. Jain. *International Journal of Hydrogen Energy* 35 (2010) 5133-5144.
5. R. Barsky and L. Kilian *Journal of Oil and Macroeconomy Since the 1970s*. <http://www.nber.org/papers/w10855> accessed (22/09/2017)
6. IEA. Key world energy statistics 2016. <http://www.iea.org/publications/freepublications/publication/key-world-energy-statistics.html> accessed (22/09/2017)
7. BP. Statistical review of world energy 2013. <http://www.bp.com/en/global/corporate/about-bp/energy-economics/statistical-review-of-world-energy-2013.html> accessed (22/09/2017)
8. CDIAC. Carbon Dioxide Information Analysis Centre. <http://cdiac.ornl.gov> accessed (22/09/2017)
9. Department for Transport. Cars and Carbon Dioxide. <http://www.dft.gov.uk/vca/fcb/cars-and-carbon-dioxide.asp> accessed (22/09/2017)
10. US EIA. EIA annual energy outlook 2014. <http://www.eia.gov/totalenergy/> accessed (22/09/2017)
11. Nations, U. A summary of the Kyoto Protocol. [http://unfccc.int/kyoto\\_protocol/background/items/2879.php](http://unfccc.int/kyoto_protocol/background/items/2879.php) accessed (22/09/2017)

12. A. Züttel, A. Remhof, A. Borgschulte and O. Friedrichs Hydrogen: the future energy carrier *Philos. Trans R. Soc. A Math. Phys. Eng. Sci* 368 (2010) 3329-3342
13. Department for Transport. Cars and Carbon Dioxide. <http://www.dft.gov.uk/vca/fcb/cars-and-carbon-dioxide.asp> accessed (22/09/2017)
14. V.P. Utgikar and T. Thiesen *Technology in Society* 27 (2005) 315-320.
15. P.P Edwards, V.L. Kuznetsov, W.I.F. David, N.P. Brandon *Journal of Energy Policy* 36 (2008) 4356-4362.
16. A. Züttel, Materials for hydrogen storage. *Mater. Today* 6, 24–33 (2003).
17. Refueling Station Compressor Efficiency, CDP #61. [http://www.nrel.gov/hydrogen/docs/cdp/cdp\\_61.ppt](http://www.nrel.gov/hydrogen/docs/cdp/cdp_61.ppt) accessed (22/09/2017)
18. H. Imamura, K. Masanari, M. Kusuhara, H. Katsumoto, T. Sumi and Y. Sakata. *Journal of Alloys Compound* 386 (2005) 211.
19. V.P. Utgikar and T. Thiesen *Journal of Technology in Society* 27 (2005) 315-320.
20. H. Wang, H.J. Lin, W.T. Cai, L.Z. Ouyang and M. Zhu *Journal of Alloys and Compounds* 658 (2016) 280-300.
21. J. Seon-Ah, S. Jac-Hyeok, A. Jae-Pyoung, C. Young Whan and Y. Kyung-Woo *Journal of Acta Materials* 55 (2007) 5073-5079.
22. K. M. Thomas, *Journal of Catal. Today* 120, 389–398 (2007)
23. H. Imamura, Y. Hashimoto, T. Aoki, T. Ushijima and Y. Sakata *Journal of Materials Transactions* 55(3) (2014) 572-576.
24. A. Baldi and B. Dam *Journal of Materials Chemistry* DOI: 10. 1039/c0jm03249b
25. S. A. Jin, J. H. Shim, J. P. Ahn, Y. W. Cho and K. W. Yi *Journal of Acta Materialia*, 55 (15) (2007) 5073-5079.
26. W. Oelerich, T. Klassen, and R. Bormann. *Journal of Alloys and Compounds* 315 (1) (2001) 237-242.

27. T. Noritake et al. *Journal of Appl. Phys. Lett.* 81 (2002) 2008.
28. K F. Aguey-Zinsou and J R. Ares-Fernández *Journal of Energy & Environmental Science*, 3(5) (2010) 526-543.
29. H. Wang, H.J. Lin, W.T. Cai, L.Z. Ouyang and M. Zhu *Journal of Alloys and Compounds* 658 (2016) 280-300.
30. S. Abdessameud, M. Mezbahul-Islam and M. Medraj *Journal of Sci. World* 2014 (2014) 190320.
31. J.P.A. Makongo, Y. Prots, U. Burkhardt, R. Niewa, C. Kudla and G. Kreiner *Journal of Philosophical Magazine* 86 (2006) 427-433.
32. A. Zaluska, L. Zaluski and J.O. Strom-Olsen *Journal of Alloys Compd.* 288 (1999) 217-225.
33. H. Imamura, Y. Hashimoto, T. Aoki, T. Ushijima and Y. Sakata. *Journal of Materials Transactions* 55(3) (2014) 572-576.
34. M. Barawi, C. Granero, P. Diaz-Chao, C.V. Manzano, M. Martin-Gonzalez, D. Jimenez-Rey, I.J. Ferrer, J.R. Ares, J.F. Fernandez and C. Sanchez *International Journal of Hydrogen Energy* 39 (2014) 9865-9870.
35. A. Baldi and B. Dam *Journal of Materials Chemistry* 21 (2011) 4021.
36. J. R. Ares, F. Leardini, P. Díaz-Chao, J. Bodega, D. W. Koon, I. J. Ferrer and C. Sánchez *Journal of Alloys and Compounds*, 495(2) (2010) 650-654.
37. K. Higuchi, K. Yamamoto, H. Kajioka, K. Toiyama, M. Honda, S. Orimo and H. Fujii. *Journal of Alloys and Compounds*, 330 (2002) 526-530.
38. Q. Jianglan, L. Yang, X. Gongbiao, Z. Jie and L. Xingguo *Journal of Dalton Trans* 43 (2014) 5908.
39. S. Huaiyu, M. Weigang, K. Masamochi, T. Yasuyuki, X. Gongbiao, F. Shigenori, F. Sayoko, B. Sean and L. Xingguo *International Journal of hydrogen energy* 39 (2014) 9893-9898.

40. A. Needleman and S. Suresh *J Mech Phys Solids* 44 (5) (1996).
41. C.M.P. Fry, D.M. Grant and G.S. Walker *International Journal of hydrogen energy* 39 (2014) 1173-1184.
42. J.R. Ares, F. Leardini, P. Diaz-Chao, I.J. Ferrer, J.F. Fernandez and C. Sanchez *International Journal of Hydrogen Energy* 39 (2014) 2587-2596.
43. R.E. Cuthrell, F.P. Gerstle Jr and D.M. Mattox *Journal of Rev Sci Instrum* 60(6) (1989) 1018.
44. A. Baldi, M. Gonzalez-Silveira and V. Palmisano *Journal of Phys Rev* 1-4 (2009) 226102.
45. C.J. Chung et al. *Phys. Rev. Lett.* 108, 1-4 (2012).
46. A. Molinari, F. D'Amico, M. Calizzi, Y. Zheng, C. Boelsma, L. Mooij, Y. Lei, H. Hahn, B. Dam and L. Pasquini *International Journal of hydrogen energy* 41 (2016) 9841-9851.
47. T. J. Richardson, J. L. Slack, R. D. Armitage, R. Kostecki, B. Farangis and M. D. Rubin. *Journal of Appl. Phys. Lett* 3047 (2001).
48. S. Bao, K. Tajima, Y. Yamada, M. Okada and K. Yoshimura *Journal of Sol. Energy Mater. Sol. Cells* 224 (2008).
49. S. Abdessameud, M. Mezbahul-Islam and M. Medraj Thermodynamic Modeling of Hydrogen Storage Capacity in Mg-Na Alloys. *Sci. World J.* **2014**, 190320 (2014).
50. J. Hwaebong, Y. Junhan, C. Sungmee and L. Wooyoung *Journal of Alloys and Compounds* 601 (2014) 63-66.
51. Richardson et al. *J. Alloys Compd.* 356, (2003) 204.
52. J.P.A. Makongo, Y. Prots, U. Burkhardt, R. Niewa, C. Kudla and G. Kreiner *Journal of Philosophical Magazine* 86 3-5 (2006) 427-433.
53. S. Singh, S.W.H. Eijt, M.W. Zandbergen, W.J. Legerstee and V.L. Svetchnikov *Journal of Alloys and Compounds* 441 (2007) 344-351.
54. Y. Hong-Hui and J.W Hutchinson *International Journal of Fracture* 113 (2002) 39-55.

55. H. Le-Quoc, A. Lacoste, S. Miraglia, S. Bechu, A. Bes and L. Laversenne *International Journal of Hydrogen Energy* (2014) 1-8.
56. Y. Pivak et al. *Journal of Sci. Mater.* 60 (2009) 348-351.
57. Y. Pivak, H. Schreuders, M. Slaman, R. Griessen and B. Dam *International Journal of Hydrogen Energy* 36 (2011) 4056-4067.
58. Y. Pivak, V. Palmisano, H. Schreuders and B. Dam *Journal of Mater. Chem.* 1 (2013) 10972.
59. A. Baldi and B. Dam *Journal of Materials Chemistry* DOI: 10.1039/c0jm03249b
60. V. Palmisano, M. Filippi, A. Baldi, M. Slaman, H. Schreuders and B. Dam *International Journal of Hydrogen Energy* 35 (2010) 12574-12578.
61. K. Yoshimura, Y. Yamada and M. Okada *Journal of Surface Science* 566-568 (2004) 751-754.
62. M.K. Dietrich, A. Laufer, G. Haas, A. Polity and B.K. Meyer *Journal of Sensors and Actuators A* 206 (2014) 127-131.
63. X. Gongbiao, Y. Junzhi, F. He, L. Wei, Z. Jie and L. Xingguo *Journal of RSC Advances* 3 (2013) 4167.
64. C.M.P. Fry, D.M. Grant and G.S. Walker *International Journal of hydrogen energy* 38 (2013) 982-990.
65. A. Baldi et al. *Journal of Phys. Rev. B* 81 (2009) 1-10.
66. L.Z. Ouyang, S.Y. Ye, H.W. Dong and M. Zhu *Journal of Appl. Phys. Lett.* 90 (2007) 21917.
67. L.P. Mooij et al. *Journal of Adv. Energy Mater.* 1 (2011) 754-758.
68. H. Jung, S. Cho and W. Lee *Journal of Alloys and Compounds* 635 (2015) 203-206.
69. M. Ohring *The Materials Science of Thin Films* (1992).
70. C.V. Thompson *Journal of Acta Metall.* 36 (1988) 2929-2934.

71. M. Slaman, B. Dam, M. Pasturel, D.M. Borsa, H. Schreuders, J.H. Rector, R. Griessen *Journal of Sensors and Actuators*, 123 (2007) 538-545.
72. J.R. Ares, F. Leardini, P. Diaz-Chao, I.J. Ferrer, J.F. Fernandez and C. Sanchez *Journal of hydrogen energy* 39 (2014) 2587-2596
73. K. Yamamoto, K. Higuchi, H. Kajioka, H. Sumida, S. Orimo, H. Fujii *Journal of Alloys and Compounds*, 330-332 (2002) 352-356.
74. P.J. Kelly and R.D. Arnell *Journal of Vacuum*, 56(3) (2000) 159-172.
75. Scanning Electron Microscopy  
<https://www2.warwick.ac.uk/fac/sci/physics/current/postgraduate/regs/mpags/ex5/techniques/structural/sem3/> assessed (22/09/2017)
76. P. Chater (University of Birmingham, 2010).
77. P. Gates Gas Chromatography Mass Spectrometry  
<http://www.bris.ac.uk/nerclsmsf/techniques/gcms.html> assessed (22/09/2017)
78. K. Higuchi, H. Kajioka, K. Toiyama, H. Fujii, S. Orimo, Y. Kikuchi, J. Alloys Comp. 293-295 (1999) 484-489.
79. M. A. Brown, A. J. Rosakis, X. Feng, Y. Huang and E. Ustundag *International Journal of Solids and Structures* 44 (2007) 1755-1767.
80. X. Feng and Y. Huang *Journal of Acta Mech. Sinica* 21 (2005) 362-370.
81. G.G. Stoney *Journal of Proc. R. Soc. London. Ser. A* 82 (1909) 172.
82. H. Lbach. *Surface science reports*, 29(5) (1997) 195-263.

